Advances in Optics and Photonics

Mode-division and spatial-division optical fiber sensors

Christophe Caucheteur,[1,*] **Joel Villatoro,**[2,3]
Fu Liu,[4,5] **Médéric Loyez,**[1,6] **Tuan Guo,**[4] **and**
Jacques Albert[5]

[1] *Electromagnetism and Telecommunication Department, University of Mons, 31 Boulevard Dolez, 7000 Mons, Belgium*
[2] *Department of Communications Engineering, University of the Basque Country UPV/EHU, Plaza Torres Quevedo 1, E-48013 Bilbao, Spain*
[3] *IKERBASQUE, Basque Foundation for Science, E-48011 Bilbao, Spain*
[4] *Institute of Photonics Technology, Jinan University, 855 Xingye East Av, Guangzhou 511443, Guangzhou, China*
[5] *Department of Electronics, Carleton University, 1125 Colonel By Drive, Ottawa, ON K1S 5B6, Canada*
[6] *Proteomics and Microbiology Department, University of Mons, 6 Avenue du Champ de Mars, 7000 Mons, Belgium*
*Corresponding author: christophe.caucheteur@umons.ac.be

The aim of this paper is to provide a comprehensive review of mode-division and spatial-division optical fiber sensors, mainly encompassing interferometers and advanced fiber gratings. Compared with their single-mode counterparts, which have a very mature field with many highly successful commercial applications, multimodal configurations have developed more recently with advances in fiber device fabrication and novel mode control devices. Multimodal fiber sensors considerably widen the range of possible sensing modalities and provide opportunities for increased accuracy and performance in conventional fiber sensing applications. Recent progress in these areas is attested by sharp increases in the number of publications and a rise in technology readiness level. In this paper, we first review the fundamental operating principles of such multimodal optical fiber sensors. We then report on the theoretical formalism and simulation procedures that allow for the prediction of the spectral changes and sensing response of these sensors. Finally, we discuss some recent cutting-edge applications, mainly in the physical and (bio)chemical fields. This paper provides both a step-by-step guide relevant for non-specialists entering in the field and a comprehensive review of advanced techniques for more skilled practitioners. © 2022 Optica Publishing Group

Mode-division and spatial-division optical fiber sensors

Christophe Caucheteur, Joel Villatoro, Fu Liu, Médéric Loyez, Tuan Guo, and Jacques Albert

1. INTRODUCTION

1.1. Motivation and Significance

Optical fiber sensors are almost as old as the first optical fibers developed for telecommunications. It can be considered that the idea to use optical fibers as sensors occurred as a side benefit of efforts to prevent them from being perturbed by temperature changes and micro- or macro-bending in telecommunication networks. Nowadays, many optical fiber sensor configurations have matured into commercial products that are very competitive with other sensing technologies, in terms of both performance and cost [1,2]. The most prominent examples to date remain fiber Bragg grating (FBG) sensors and arrays, as well as distributed sensors based on various implementations of Brillouin, Raman, and Rayleigh scattering in single-mode fibers (SMFs). Although most commercial systems rely on measurements of the transmitted or reflected fundamental mode of single-mode optical fibers, more recent developments have focused on multimodal architectures that considerably widen the sensing modalities. Temperature, strain, displacement, pressure, and bending have been the physical parameters of interest of the first developed sensors. Then, a continuous effort has been made towards performance enhancements and additional sensing modalities, especially in the chemical and biological fields. Although access to the additional cladding-guided modes that conventional SMFs can support has been very fruitful along these lines, there are also many more new sensing schemes that take advantage of the multiple available propagating modes of specialty fibers: fibers with multilayered refractive index profiles, fibers with non-circular cross sections, microstructured fibers, and many kinds of multicore fibers (MCFs). The most important differentiators enabled by these advances arise from the possibility of multiparameter sensing with a single device, the reduction of cross-sensitivities or the improved accuracy of a single measured parameter by combining the responses of many fiber modes to its evolution. The sensor configurations that allow those modalities include resonant devices (refractive index gratings) and mode interferometers. Both mode-division-multiplexed (MDM) and spatial-division-multiplexed (SDM) optical fiber sensor configurations have been studied and demonstrated for physical sensing applications (temperature, strain/lateral force/pressure, curvature, torsion, vibration, microfluidics, acoustics, electric, and magnetic fields) as well as for chemical, biochemical, electrochemical, and medical sensing applications. The overall progress in these fields is attested by the steady annual growth of the number of active international research groups, publications (currently several hundred per year) and patents. Compared with commercially available optical fiber sensing solutions where advances consist mostly of engineering optimization, most research on MDM and SDM sensors has been more fundamental and concentrating on widening the sensing modalities and the applications, as evidenced by publications in top-level journals of the multidisciplinary fields covered by these technologies. However, these fundamental research paths are now being translated into more applied ones and an important rise in technology readiness levels has been achieved over the past few years. Given the ample evidence of commercial viability for

more mature optical fiber sensing configurations, the future for emerging technologies such as MDM and SDM sensors is highly promising.

1.2. Scope and Organization of the Review

The objective of the current review is to highlight the recent trends in MDM and SDM sensors, mainly focusing on new applications that have been enabled (compared with single-mode-based systems), and on the increased use of specific coatings and plasmonic amplification of sensing modalities. In addition, there are a number of common underlying mathematical and physical principles to all these systems that are described experimentally and through simulations.

This review does not deal with distributed fiber sensors, as they are based on totally different sensing mechanisms than point sensors and mostly designed for other applications [3,4]. With regards to point sensors, the emphasis will be on devices where more than one guided mode is involved, as this is where most of the new applications have emerged and where most of the potential lies for further advances. As a result, devices that have been commonly used (and commercialized) for decades (Bragg grating strain and temperature sensors for instance) are not discussed beyond their fundamental operating principles as they apply to more advanced systems. Furthermore, there have been numerous recent thematic fiber-optic sensor review articles covering specific technologies or applications, consisting mostly of commented literature surveys and comparative lists of performance and characteristics [5–9]. The current review aims at providing a unified vision and understanding of single-point optical fiber sensors encompassing several fiber modes in one core, in multiple cores or both in the core(s) and the cladding. This family of optical fiber sensors has been the subject of intense research and development over the past few years and has witnessed considerable progress both in terms of practicality and target applications. In the following, we use the terminology "multimodal" sensors to lighten the text in describing common features of mode division and spatial division sensors.

The main discriminant factor in the sensor systems to be considered is the participation of at least two modes with different effective refractive indices and mode field distributions. Propagation of these modes into any waveguiding structure where they at least partially overlap will lead to wavelength-dependent transfer functions or to total transmitted power fluctuations when connected to optical instrumentation by input and output SMFs. The main operating principle of any sensor system design is to control the amount of excitation and recoupling of different modes at the input/output junctions as well as the lengths and positions of the light paths of the various modes through the system (Fig. 1).

The possible systems are divided into two main categories: resonant or interferometric (and sometimes both). Interferometric systems require the excitation of more than one co-propagating waveguide mode over a finite distance over which the modes propagate at different phase velocities. Any change in the refractive index structure over which the modes propagate will change their relative phase velocities and, hence, their field amplitude superposition and, thus, the power coupled into the output(s) of the device. Resonant systems involve a periodic modulation of the refractive index of some part of the fiber device (a grating), resulting in coherent coupling of power between modes. This coupling only occurs at specific wavelengths that depend on the mode effective indices and the grating period, as measured by the positions and amplitudes of resonances in their transmission and/or reflection spectra. Any small perturbation of the effective indices changes the resonant wavelength(s) whereas amplitude changes are typically obtained from changes in the waveguiding structure that have a measurable

Figure 1
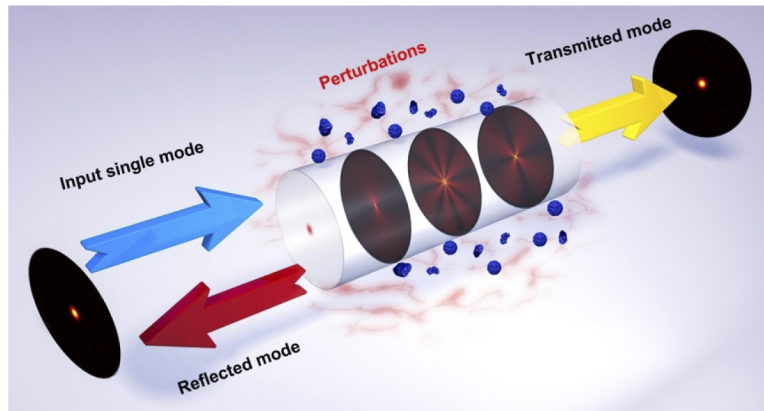
Operating principle of a generic multimodal optical fiber sensor based on a finite-length sensing section under arbitrary perturbations, along with single-mode input and output fibers.

effect on the mode shapes and, thus, on the grating coupling coefficients (adding a lossy coating or macrobending, for instance).

The remainder of the paper is organized as follows. Section 2 provides a general overview of the current knowledge on the necessary fundamental fiber-optic principles involved in fiber sensor design. First, we summarize how fiber modes and their properties can guide and affect designs in many kinds of fibers, including MCFs designed for spatial-division multiplexing. Then, the principles and implementations of all-fiber interferometric systems are introduced, including tapers, single-mode/multimode/single-mode (SMS) structures, supermode interferometers, and fibers with weakly coupled multiple cores. Lossy mode resonances (LMRs) in fibers coated with layers thick enough to support waveguiding are also considered. Finally, fiber grating principles, configurations, and their subsequent sensing modalities are presented. Sections 3 and 4 describe a selection of representative recent advances in physical, electromagnetic, chemical/biochemical, and medical applications of fiber-optic point sensors. There are four tables that present condensed information from a non-exhaustive but very representative list of relevant references. This is followed by a discussion about the current challenges that are preventing the faster and wider deployment of new fiber-optic sensor technologies as well as by suggested opportunities for new research that have appeared as a result of the most recent advances.

2. FUNDAMENTALS OF MULTIMODAL FIBER SENSORS

2.1. Fiber Modes in Multimode and Multicore Systems

What has become quite interesting and rich in new sensing opportunities in recent years is the appearance of new types of SMFs and multimode fibers (MMFs) developed for a variety of applications. These applications include short- and long-haul communications, active fiber devices for use in fiber lasers, supercontinuum sources, and other nonlinear optical systems and biomedical devices. In particular, it was realized that fibers with cores able to support "a few" modes had sufficient mode stability to sustain independent channels of information over long distances without intermodal mixing (thereby leading to "mode division multiplexing") [5–24]. In the same category, MCFs that carry information in independently guiding cores within an optical fiber also have many interesting new sensing applications [25–55].

Prior to going further in the presentation of such structures, it is certainly relevant to recall what an optical fiber mode is. The mathematical formalism is available in numerous textbooks [56–59] and is not reproduced here. We just provide some important information for the correct understanding of the essence of multimodal optical fiber sensors. Propagation of light in optical fibers is derived from Maxwell equations by solving the Helmholtz equation, usually in a (r,z,φ) cylindrical system of coordinates. The polarization states of modes are crucial in determining their sensitivities to perturbations. Numerous kinds of optical fibers can be described (or for graded-index fibers approximated) by a series of concentric layers of transparent dielectric materials. When the refractive index contrast of the whole structure is small (including the surrounding material), it is common to use the scalar wave equation to obtain the so-called linearly polarized (LP) modes. However, when the refractive index contrast becomes larger, or when sensing modalities depend critically on mode field polarization, the LP approximation results are inaccurate and the full vector analysis remains the sole option.

Therefore, for the sake of completeness, we consider this more exhaustive representation in the following. For fibers with cylindrical symmetry, within each layer the field components are linear combinations of ordinary and modified Bessel functions. A solution is found by matching the tangential field components of adjacent layers. Four types of vector fiber modes exist.

 - TE_{0n} describes the transverse electric family of modes for which the component of the electric field along the optical fiber axis is zero. The electric field of these modes is strictly azimuthal (no r or z components) and, therefore, parallel to the boundaries of the fiber layers.

 - TM_{0n} describes the transverse magnetic family of modes for which the component of the magnetic field along the optical fiber axis is zero. The electric field of these modes is forming closed loops in r–z planes and is, therefore, radially polarized across the layer boundaries.

 - EH_{mn} and HE_{mn} are hybrid modes for which the components of the electric and magnetic fields along the optical fiber axis are both non-zero. The subscripts m and n are both integers: m corresponds to the multiplier of the angle in the cosine/sine functions that determines the azimuthal dependence of the modes whereas n is the order of appearance of a mode in descending order of effective index. All these modes have mixed polarization (r, z, and φ components are all non-zero), but for modes with high radial orders (greater than about 10), EH modes are predominantly TM polarized (i.e., E fields with r and z components), whereas HE modes are TE polarized (actually φ polarized). This means that EH/TM cladding modes are polarized perpendicularly to the fiber surface whereas HE/TE modes are polarized along the plane of the fiber surface. Finally, the cylindrical symmetry imposes that any mode can be rotated by any angle ψ without losing its identity. For instance, Fig. 2 shows two modes with a seemingly identical (but rotated) profile (as seen from the intensity pattern). A closer examination of the mode electric fields shows that they are indeed different, i.e., an HE mode on the left and an EH mode on the right. Upon rotation by $\psi = \pi/2$, the HE mode intensity pattern becomes identical to that of the EH mode, but the fields are completely different whereas the effective indices are slightly different. As a result, the sensing properties of devices based on such two modes will be distinct in most cases.

For about 20 years now, one of the richest (if somewhat predictable) fields of research in fiber sensors has been all-fiber interferometers constructed by splicing short sections

Figure 2
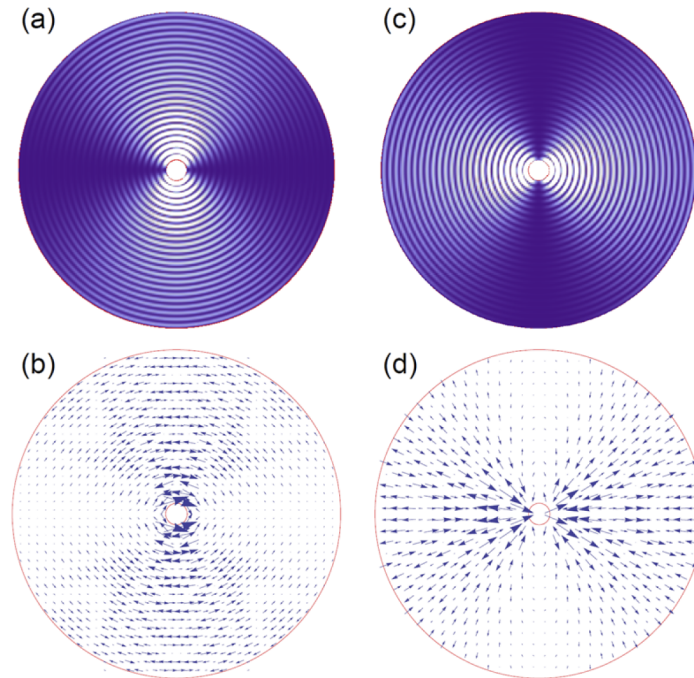
(a), (c) Mode intensity and (b), (d) vector field plots in the cladding region of a single-mode fiber in air, for the $HE_{1,25}$ ($N = 1.40858$) and $EH_{1,25}$ ($N = 1.40844$) modes with $\psi = 0$.

of different types of fibers between SMF input and output leads, optimized for specific sensing applications. In a more general sense, it is shown in the following sections how to select and use multimodal fiber types with specific field distributions and effective index dispersions to provide enhanced sensing accuracy in certain applications.

There are many well-established methods to calculate mode fields and their effective and group indices in fibers with arbitrary refractive index profiles, but the sensor precision requirements (and recent achievements) indicate that the accuracy of mode solvers is of prime importance. In particular, modern spectral interrogation systems for fiber gratings can provide wavelength resolutions of a few picometers and resonant wavelength position accuracies of the order of 0.1 pm. Therefore, to simulate and model such sensors and sensing schemes at wavelengths between ~1000 and ~1600 nm, mode effective indices must be precise to at least 6 significant digits. In addition, this requires using the most accurate fiber parameter values available, i.e., the refractive indices and their dispersion, and the cross-section geometry (dimensions). Of course, the problem is further complicated with arbitrary coatings on the fiber surface, such as the nanoscale metal layers used for plasmonic sensors and by the fact that fiber processing (such as laser irradiation to form gratings in the core of optical fibers) often leads to hard to quantify changes in the fiber indices and dispersion [60].

Many commercially available optical fiber mode solvers come with solving options based on the complexity of the fiber cross section. There are analytic and semi-analytic methods that are in principle "exactly accurate" for cylindrically symmetric structures with arbitrary numbers of layers [57–62]. They are derived directly from Maxwell's equations and use modern numerical tools for matrix computations and root searching that have more than enough precision. There are also 1D finite-difference (FD) mode solvers where the azimuthal dependence of the solutions of the wave equation is removed by separation of variables using the periodicity of the mode

solutions with azimuthal angle [63–65]. Solving the same problem with these two methods is a good test of their validity because they are based on quite different algorithms and, in fact, may help in choosing the grid resolution for the FD approach. For fibers lacking in cylindrical symmetry, such as fibers with a deformed cladding (D-shaped, rectangular, or with a deep wide slot to expose the core), and apart from very few special configurations, "brute force" methods based on 2D FDs or finite-element (FE) techniques are required [58,63,66]. Although still configured to force the field solutions to satisfy Maxwell's equations at all the material boundaries, the quality of the mode fields and effective indices obtained with these algorithms for arbitrarily complex fiber cross sections are difficult to verify with high quantitative precision.

There are also specific mode solving approaches for the special case of photonic crystal fibers (fibers with microstructures that have radial and azimuthal symmetries allowing the use of bandgap calculation techniques [67]). In all of these cases, FD and FE methods provide the most flexible mesh gridding for arbitrarily complex refractive index distributions [58,63]. However, achieving parts per million effective index accuracies then requires very extensive calculation times because of the sizes of the calculation grids.

Finally, there are many sensing approaches that rely on depositing functional or waveguiding coatings on the surface of the fiber. Waveguiding coatings that are thick enough and/or have a sufficiently large refractive index to guide light within their boundaries, produce what is usually referred to as LMRs because they allow for the resonant transfer of energy from an underlying guided mode to the coating guided mode [68,69]. These coatings must be treated as additional layers in the refractive index profile of the fiber and the guided modes of the whole system must be recalculated. As LMRs are typically highly dispersive, because they are guided near cut-off by very thin layers with small index difference from the fiber and/or surroundings, the effect on grating-based resonances can be quite large (cf. Section 2.5). In the case of non-waveguiding functional coatings, the layers used are typically very thin and their presence modifies the properties of the modes guided by the interface where the coating is located (see [70] for a recent example). The effect of the coatings and of their modifications depends on the overlap of the evanescent field of these modes with the coating layer. For these types of coatings, modes can also be recalculated or perturbation techniques based on the modes of the uncoated fiber can be used. Simulation of sensing events involve changing the permittivity or thickness of the coating and finding their effect on the mode effective indices and field distributions. However, for many coatings the exact optical properties are not precisely known (see, for instance, [71,72] and references therein). They can depend rather critically on the deposition techniques used and even on parameters chosen for a given deposition technique. Ultrathin coatings (of the order of $\lambda/100$) further complicate the issue, as they are rarely perfectly uniform and may have roughness values similar to their thickness. This results in a regime where they can be difficult to distinguish from nanoparticles, with consequences on the exact value of their average complex permittivity [73].

Special consideration must be made for cylindrically symmetric multimode systems, including the important case of the core and cladding of the standard SMF, as they are used in many fiber sensor systems. As shown in Fig. 2, the high-order cladding-guided modes (i.e., with effective indices lower than about 1.4 for silica glass fibers) separate into four well-defined quasi-degenerate (similar effective index) groups defined by their azimuthal order parity (odd or even) and their dominant electric field orientation in the fiber cross section. The existence and composition of these mode families can be verified by simulations, but they also show up very

Figure 3
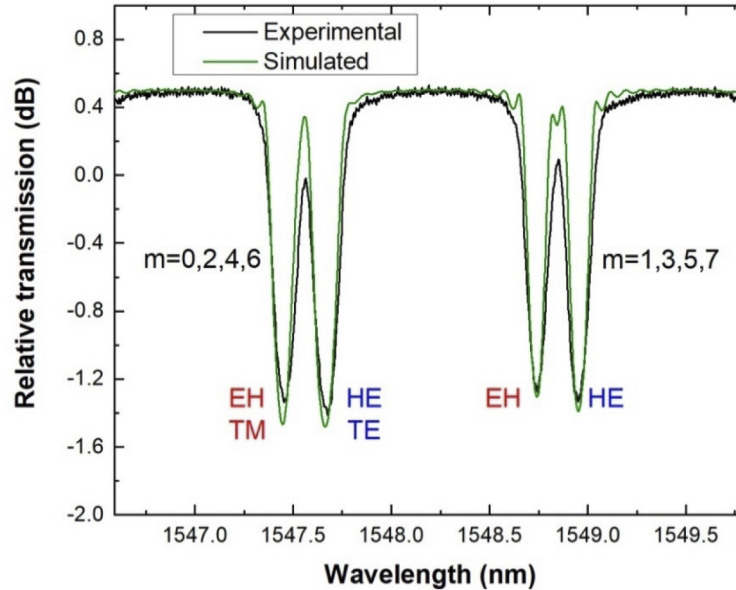
Part of a 1-cm long 11.7° tilted fiber Bragg grating transmitted power spectrum written in single-mode optical fiber (CORNING SMF28) with a period of 556 nm showing two neighboring cladding mode resonances. The mode content of the resonances is indicated by the labels and azimuthal order *m*.

clearly, for higher-order modes at least, in the measured spectra of fiber gratings such as off-center FBGs [74–76], excessively tilted fiber gratings (Ex-TFGs) [77], and tilted fiber Bragg gratings (TFBGs) [78]. Figure 3 shows a TFBG spectrum extract which indicates the corresponding mode polarization and azimuthal parity of four measured and simulated resonances (the EH/TM modes are always on the short-wavelength side of a resonance pair and resonance pairs alternate between odd and even azimuthal order groups) [79]. Understanding and controlling these mode profile distributions and polarizations is an essential feature of advanced multimodal sensor design.

In the same way as with few mode fibers, the optical networking community developed "spatial division multiplexing" using fibers with several cores to increase the information carrying capacity of single fibers. When the cores are optically isolated from each other and from the cladding surface, each core mode of such fibers can be calculated using the same techniques used for single-core fibers. However, the effect of sensing-induced perturbations on the whole fiber may in certain circumstances affect the cores differentially. The best example of this is in fiber shape sensors based on MCFs, because bending the fiber introduces a non-uniform stress distribution over the fiber cross section and, thus, perturbs the modes of each core by different amounts. Interrogation of MCF segments requires special splicing techniques and devices such as fan-in, fan-out or "photonic lanterns" to get light in and out of the multiple cores separately. On the other hand, when the individual cores are sufficiently close for their mode fields to interact, there are two approaches for solving light propagation [27,41,44,46,52]: finding the "supermodes" of the whole structure and treat them exactly the same way as those of few mode fibers, or using a coupled-mode formalism based on the "approximate" modes of each core taken separately. The second option is only feasible when the coupling is weak (cf. Section 2.3.3.3).

2.2. Sensing Properties of Fiber Modes

The following discussion focused on sensing "small" changes which do not alter significantly the guiding properties of the fibers.

In all sensing modalities targeting the measurements of small changes, the most important mode property is its effective refractive index, because it affects power level changes in mode interference devices or wavelength shifts in resonant devices. The mode field distributions on the other hand affect the amplitudes of the spectral changes. For instance, the first-order correction expression for the change in the effective index N of a guided mode due to a localized change in refractive index (from $\bar{n}$ to n) is given by [59]

$$N^2 = \bar{N}^2 + \frac{1}{\iint \bar{E}^2 dA} \iint (n^2 - \bar{n}^2)\bar{E}^2 dA, \tag{1}$$

where $\bar{N}$ and $\bar{E}$ are the effective index and transverse electric field distribution of the unperturbed mode. The integral in the numerator is obviously calculated only over the region of the fiber cross section where refractive index changes occur (usually the fiber surface for chemical sensors, but the entire fiber for small strains, for instance). This formula is very convenient for estimating the sensitivity of sensor designs without exhaustive mode and propagation simulations and, in particular, to compare the sensitivities of different modes in multimode sensors.

A more accurate but still first-order (linear) estimation of the change in a mode effective index due to variations in fiber parameters is provided by Eq. (2). The rate of change for the effective index of a mode N due to a perturbation "x" is given by

$$\frac{dN}{dx} = \sum_k \frac{\partial N}{\partial n_k} \frac{\partial n_k}{\partial x} + \sum_j \frac{\partial N}{\partial a_j} \frac{\partial a_j}{\partial x}, \tag{2}$$

where variables n_k represent the refractive indices of all the materials in the guiding cross section (including coatings and surrounding materials in addition to the core and cladding of the optical fiber) and a_j the dimensions of all the waveguiding segments found in the optical fiber sensor cross section. The first factor in these two sums represents the change in effective index of a mode relative to a change in refractive index of the materials and to a change in dimensions, respectively. These quantities can be found by mode solver calculations with small variations in fiber parameters. The second factor requires knowledge (and calculations) of the effect of given perturbations (temperature, strain, chemical change, etc.) on refractive indices and fiber dimensions. For grating-based sensors, a third contribution will come from the effect of the perturbation on the period of the grating (Section 2.6).

It is now obvious that when dealing with multimode structures, a given perturbation will affect modes differently because their modal dispersions differ and their fields occupy different spatial regions of the fiber cross section. Multimodal sensors are ideal to take advantage of these differences to improve their accuracy by comparing measurements affecting more than one mode.

Finally, for calculations involving fiber perturbations that cannot be considered "small," there remains the option of re-simulating for the modes of the new waveguiding structure, but this is generally quite computationally expensive and rarely done.

2.3. Interferometric Systems

2.3a. Mode–Mode Interference

It is known that the propagation constant of each mode supported by an optical fiber or by any other optical waveguide has a unique value, typically denoted β and equal to

$(2\pi/\lambda)$ times the mode effective index N (with λ the light wavelength). This represents a possible solution of Maxwell equations for a waveguide with its particular geometry, dimensions, and refractive index profile. Theoretically, the number of modes that a waveguide can support is limited. It depends on the wavelength, the dimensions, and the refractive indices of the fiber materials. Hence, an optical fiber can be designed to support a single mode only, two modes, few modes, or hundreds of modes.

Each mode excited in a waveguide propagates at a different phase velocity. The phase of the ith mode (ϕ_i) after propagating in an optical fiber or waveguide of length L is $\phi_i = \beta_i L$. An initial phase (γ_i) of the mode at the optical fiber input can be added to ϕ_i but in many practical applications, γ_i can be neglected as it is common to all the modes. If two or more modes propagate in an optical fiber, a beating can be produced between them. In this case, there is a relative phase shift between the modes.

The above properties of modes are what lead to mode interference in an optical fiber, which was an issue (modal dispersion) in the early years of optical telecommunications when MMFs were used. However, mode interference can be useful for sensing and metrology. In these cases, modal interferometers are implemented to extract information from mode interference where the parameter to be sensed or measured is encoded.

Depending on the launching conditions and the geometrical design, two or more modes can interfere. It is, thus, possible to devise two-mode or multimode interferometers. For sensing applications, these interferometers may be alternative to the classical two-arm or multipath interferometers implemented with optical fibers, planar waveguides, or with bulk optics. Sensor design then consists of choosing which modes will provide the best selectivity and sensitivity for the application selected and the corresponding launch conditions to access the selected modes.

There is a great variety of optical fibers and configurations that can be used to devise compact modal interferometers. Several prominent examples are discussed in the following sections.

2.3b. Basic Principle, Implementations, and Sensing Modalities

The idea to use mode–mode interference for detecting sound was proposed in the late 1970s by Bucaro and Carome [80]. The concept was simple: light at a wavelength below the cut-off wavelength of a step-index SMF was used. Under these conditions, the SMF becomes multimode, thereby, allowing multimode interference.

Modal interferometers implemented with optical fibers with elliptical cores and birefringent fibers were demonstrated in the 1980s [81]. In these cases, the two interfering modes were the fast and slow modes of mutually orthogonal polarizations. In these interferometers, polarizers or mechanisms to preserve the polarization state of the guided light were necessary.

Some issues of the aforementioned modal interferometers included the need for bulk optics components, such as microscope objectives and polarizers, as well as mechanical positioners to launch light in the fiber core. Such setups are nowadays impractical for sensing applications. However, the concepts and ideas introduced in these pioneering works motivated more research on modal interferometers and their applications by many research groups reporting a great variety of sensing, filtering, and other applications.

Sensing with a classical two-arm interferometer consists of perturbing the sensing arm with the parameter to detect while the reference arm is unaltered or isolated from said parameter. However, in a modal interferometer, all the interfering modes

may be perturbed with the parameter being sensed, as all the modes propagate in the same waveguide exposed to the parameter. The latter may alter the phase of each mode that participates in the interference. If we consider the ith and jth modes, the phase difference between them can be denoted as $\Delta\phi = (\beta_j - \beta_i)L$. Thus, changes in β will result in changes of $\Delta\phi$. Changes of L, which are independent of the types of modes that participate in the interference, can also cause changes of $\Delta\phi$. Therefore, sensing with modal interferometers consists in correlating the changes of $\Delta\phi$ with the parameter(s) to sense.

In practice, most modal interferometers are interrogated with a broadband optical source and a suitable spectrometer. Thus, the transmitted or reflected spectrum is analyzed. Changes of $\Delta\phi$ caused by a measurand result in shifts of the transmission or reflection spectrum. In other cases, changes in light intensity at a specific wavelength are monitored and correlated with the parameter being sensed. Shifts of an interference pattern or intensity changes are easy to measure with a spectrometer or photodetector. However, this approach can only be used to measure changes in a property to be sensed, not an absolute static value. In addition, it cannot be used to determine changes that occur faster than the refresh rate of the spectrometer unless the wavelength change in question is less than one inter-fringe distance. In the following sections, some specific examples are discussed in more detail.

2.3c. Modal Interferometers Designs

Tapered fibers. A tapered optical fiber has a diameter that decreases gradually or abruptly to a certain value before increasing again to reach the initial fiber diameter. The narrowest segment of a tapered fiber is called the waist.

An optical fiber can be tapered by heating and pulling. A tapering station must entail a heat source (flame, mini-oven, CO_2 laser, etc.) to soften the glass and translation stages to pull the optical fiber in a controlled manner. Some fusion splicers have special programs to taper optical fibers and capillaries. Commercially available machines can taper optical fibers with literally any diameter and assemblies of optical fibers inside a capillary tube, in a controlled and reproducible manner. Therefore, the technology to fabricate tapered fibers can be considered as mature.

When a single-mode optical fiber is adiabatically tapered, the fundamental mode is broadened gradually and there is no possibility to excite other modes, resulting in the impossibility to devise a mode interferometer. However, if an optical fiber is tapered with a non-adiabatic process, two or more modes can be guided by the cladding in the taper waist. Ideally, if the shape and dimensions of the taper are designed properly, only two modes are excited in the waist. For example, Fig. 4 schematically shows a tapered SMF that has two abrupt transitions separated by a long uniform waist; this structure

Figure 4
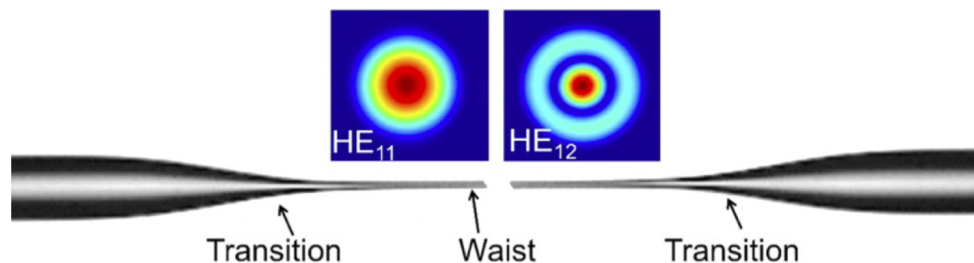
Micrograph of a tapered optical fiber and intensity patterns of the modes that participate in the interference.

Figure 5
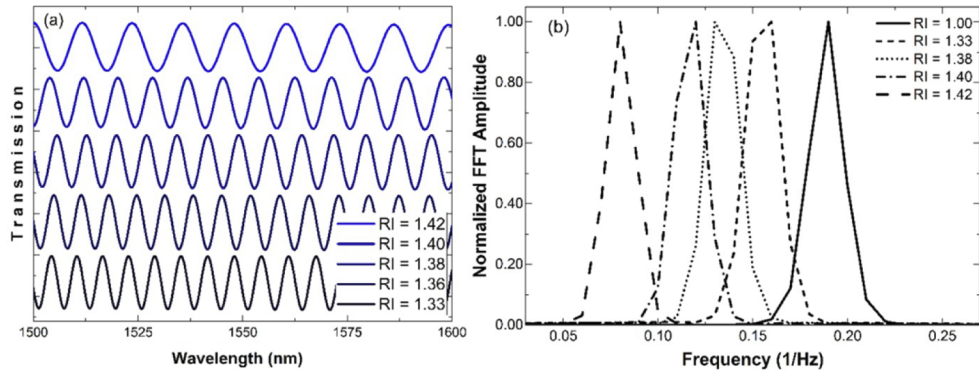
(a) Calculated interference patterns of a tapered optical fiber immersed in different refractive index (RI) solutions. (b) FFT amplitude as a function of frequency calculated from the spectra shown in (a). The tapered fiber described in Fig. 4 was considered for simulations.

was proposed and demonstrated by Salceda-Delgado *et al.* [82]. The two abrupt taper transitions allow the coupling and recombination of HE_{11} and HE_{12} modes.

The transmission spectrum of the tapered fiber depicted in Fig. 4 can be expressed as

$$T(\lambda) = I_1(\lambda) + I_2(\lambda) + 2\{I_1(\lambda)I_2(\lambda)\}^{1/2}\cos[\Delta\phi(\lambda)]\}, \tag{3}$$

where $I_1(\lambda)$ and $I_2(\lambda)$ denote the power carried by the two interfering modes. The period of the interference pattern in the transmission spectrum can be expressed as

$$P = \lambda^2/(\Delta NL), \tag{4}$$

where λ can be taken as the peak or central wavelength of the excitation light source and $\Delta N(\lambda) = N_1 - N_2$, with N_1 and N_2 the wavelength-dependent effective indices of the two interfering modes mentioned previously. It is clear that changes in ΔN will result in modifications of the period of the interference pattern. The latter can be easily calculated by means of a fast Fourier transform (FFT). This concept was proposed for refractive index sensing [82]. The advantage is that the refractive index is decoded from the period of the modal interferometer instead of the shift of the interference fringes (that are affected by both index and temperature). This feature makes the refractive index sensor temperature independent (as long as the temperature dependence of the two modes is similar and the thermal expansion along *L* negligible). To enhance the refractive index sensitivity, the dimensions of the taper can be adjusted to expose more of the mode evanescent fields to the surroundings [83].

Figure 5(a) shows the spectra of a tapered fiber immersed in media with different refractive indices. The taper had the following parameters: the two transitions were identical and had a length of 1 mm, the diameter of the waist was 10 μm, and the length of the uniform waist was 30 mm [84]. It can be seen that the period of the interference pattern increases with the refractive index. This is due to the strong dependence of the two modes excited in the taper on the external refractive index. The amplitude of the FFT as a function of frequency is shown in Fig. 5(b) for some indices; each refractive index has a unique peak in the Fourier domain.

The taper described previously was coated with a temperature-sensitive polymer to develop highly sensitive temperature sensors. In this case, temperature changes the refractive index of the polymer, which, in turn, alters the propagation constants of the HE_{11} and HE_{12} modes. The polymer that coats the tapered fiber works also as a

cladding and a packaging material. A temperature sensitivity of 3101.8 pm/°C was demonstrated in Ref, [84], which is considerably higher than the sensitivity of other fiber-optic temperature sensors (~10 pm/°C for an FBG for instance).

The interfering modes in a non-adiabatic tapered fiber can be perturbed with sensitive coatings deposited on the waist. Thus, modal interferometers based on tapered fibers are good candidates for bio- and chemical sensing. The detection of pesticides [85], humidity [86], glucose [87], and pH [88], among other parameters [89,90], has been demonstrated with modal interferometers based on non-adiabatic tapered SMFs. In these cases, the read-out is based on the shift of the interference pattern.

Some issues concerning modal interferometers based on non-adiabatic tapered fibers include fragility and high sensitivity to bending. The waist diameter of the tapers must be around 10 µm or less to allow the excitation and recombination of two modes. The drastic change in the diameter of the SMF makes it fragile and difficult to handle. Small curvatures or bending can drastically modify the transmission spectrum of a tapered SMF. Thus, the interferometer must be properly protected and kept straight during measurements.

SMS structures. The idea of splicing a segment of step-index optical MMF between two segments of identical step-index SMFs was proposed in the late 1980s [91]. Such structure was called a multifiber union, but nowadays it is most commonly denoted as an SMS fiber structure. The fabrication of an SMS structure can be performed with a conventional fusion splicer. The optical fibers are first cleaved and then fusion-spliced. The resulting SMS structure is shown schematically in Fig. 6. The structure is robust as the dimensions of the optical fibers are preserved and because the fusion-splicing process does not compromise the integrity of an optical fiber.

In an SMS structure, the cores of the SMF and the MMF are concentric because the axes of the SMF and the MMF remain perfectly aligned after the splicing process. The axial and circular symmetries condition the types of modes that can be excited in the multimode segment of the SMS structure. The index profile of the MMF and its dimensions also determine the features of the interferometer and, hence, the performance as a sensor. In addition to the configurations proposed in Fig. 6, an almost infinite sensor design space can be explored by

Figure 6
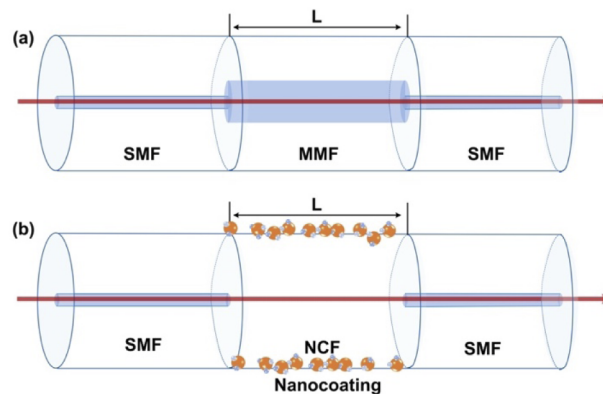
Schematic representation of two SMS structures fabricated with (a) MMF or (b) "no-core" fiber. Here *L* is the length of the multimode segment. The structure shown in (b) becomes sensitive to the surrounding medium because the evanescent field of the guided modes extends outside the fiber surface. Therefore, such structures can be coated with layers or nanomaterials.

Figure 7
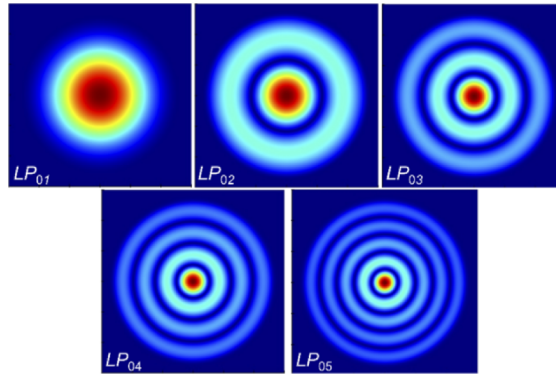
Calculated electric field distributions of the first five circular modes excited in the multimode section of an SMS structure where the MMF had a core diameter of 105 μm. A wavelength of 1550 nm was used for the calculation.

splicing a variety of fibers together, optimized for different applications. The simple fabrication and the low cost of the optical fibers needed to assemble an SMS structure make it attractive, which explains its huge popularity in the sensing community.

Figure 7 shows the electric field distribution of some circular modes excited by the fundamental mode of the SMF in an MMF with core and cladding diameters of 105 and 125 μm, respectively. Calculations were carried out with the MODE (Lumerical) waveguide simulator assuming a wavelength of 1550 nm, an SMF with numerical aperture of 0.14, and a MMF with numerical aperture of 0.22. In this case, since the incoming mode has an azimuthal order equal to 1 (HE_{11}), and because the MMF has the same cylindrical symmetry, only HE_{1n} modes (formally identical to LP_{0n} mode) are excited, and if the input core mode of the SMF is polarized, this polarization is maintained throughout the structure (unless a bending or a coating breaks the cylindrical symmetry).

The working mechanism of an SMS structure is multimode interference and self-imaging [92–95]. In such a structure, the MMF is excited by the fundamental mode of the SMF which has a Gaussian-like profile. Thus, a symmetric spot of light is injected in the MMF so that some circularly symmetric modes are excited. Most of the energy is coupled to lowest-order modes. Therefore, the beating between such lowest-order modes is calculated to predict the properties of an SMS structure [92–95]. In addition to mode profiles, their propagation in the same structure and at the same wavelength was also calculated (also with LUMERICAL). In the simulations shown in Fig. 8, the SMF and the MMF were assumed to be perfectly aligned.

A periodic rearrangement of the optical power distribution across the MMF diameter can be observed along the length of the MMF. The superposition or beating of all the circular modes excited in the MMF is what gives rise to interference and self-imaging effects. In this simulation, the MMF section length was chosen so that the output SMF was located at one of the self-imaging points, where the interference of the modes replicates the shape and position of the input mode so that it couples efficiently into the output SMF.

In sensing applications, the transmission spectrum of the SMF structure is measured or analyzed to extract information [92–95]. As an example, Fig. 9(a) shows the transmission spectrum of an SMS structure for which the MMF has a core of 50 μm, a numerical aperture of 0.22, and a length between 10.23 and 10.43 mm. The length of 10.33 mm was found to be a multiple of the self-image when the wavelength was

Figure 8
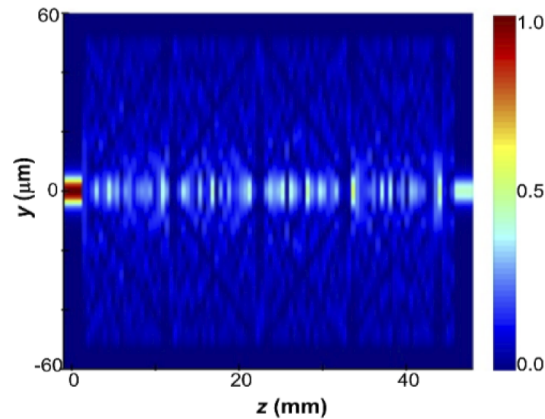
Evolution of the optical power distribution at 1550 nm along an SMS structure where the MMF has a 105 µm diameter core.

1550 nm. Note that a deviation of 100 µm in the length of the segment of MMF, i.e., less than 1%, changes drastically the wavelength position of the highest peak.

The effect of small changes in the size of the MMF core on the transmission of an SMS structure was also investigated. The core diameter of MMF may fluctuate around ±2% due to fabrication errors. Thus, the transmission spectrum of an SMS structure was calculated for an MMF core between 49 and 51 µm. The results of the calculations are shown in Fig. 9(b). A change in the MMF core of just 1 µm shifts the spectrum by nearly 60 nm.

Results shown in Figs. 9(a) and 9(b) confirm that small fluctuations in the dimensions of the SMS structure strongly affect its transmitted spectrum. Such fluctuations are difficult to avoid in practice. Therefore, it is difficult to have full control on the transmission spectrum of an SMS structure. However, the exact wavelength of the maximum of the spectrum is not important in some sensing applications as only its shift as a function of the target parameter is evaluated.

The multimode element of an SMS structure can also be a segment of a silica glass rod or capillary tube. Such a rod is commonly known as no-core fiber (NCF). The rod is the core of the multimode segment whereas the external environment is the cladding

Figure 9
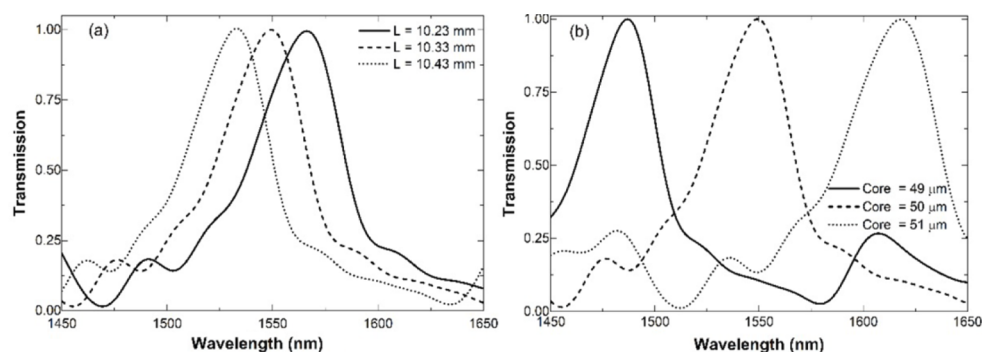
Normalized transmission spectra of an SMS structure where the MMF has a core of 50 µm. (a) Calculated spectra for different values of the length of the MMF segment. (b) Calculated spectra for an $L = 10.33$ mm but different values of the core of the MMF.

[93,96,97]. Thus, the evanescent waves of the interfering modes can interact with the external environment or with nanomaterials or nanocoatings deposited on the NCF. Such materials or coatings can be designed to be sensitive to a particular chemical or biological parameter. Their exposure to a chemical or biological parameter gives rise to changes in the phase difference between the interfering modes.

The SMS structure has been widely exploited for sensing applications [98–100]. To this end, the wavelength position of the highest peak (dip) of the transmission (reflection) spectrum of the SMS structure can be correlated with the target parameter. This means that with such a structure, absolute measurements can be taken. The wavelength position of the highest peak can change if the SMS structure is exposed to different parameters. Temperature, for example, alters the propagation constant of the modes excited in the MMF. Consequently, the peak shifts to shorter or longer wavelengths for a temperature decrease or increase. So far, different temperature sensors have been demonstrated with SMS structures [101–107].

Vibration [108], curvature/bending [109,110], and strain [111,112] can also be sensed with an SMS structure. The first three parameters can modify the propagation constants of the interfering modes by different amounts due to the elasto-optic effect. In addition to an index change, axial strain applied to an SMS structure induces a minute change in the length of the multimode segment, which also gives rise to relative phase changes between the modes. As a consequence, the transmission spectrum of the SMS structure is altered.

Sensing the aforementioned physical parameters with an SMS structure requires possible temperature fluctuations to be compensated for. A reference temperature sensor is therefore needed in practical applications. Several research groups have proposed different alternatives to measure simultaneously temperature and other physical parameter with an SMS structure [98–100].

SMS structures are also affected by issues related to cross-sensitivity, nonlinear behavior, modest reproducibility, and expensive interrogation. The shift of the transmission or reflection spectrum is not necessarily linear depending on the measuring range. The interrogation of SMS structures entails spectrometers that operate in the well-established telecommunications wavelengths that are expensive. Thus, the interrogation of a single sensor based on a SMS structure can be costly. Hence, the sensor can be unattractive in many practical applications, particularly in those where non-optical sensors are available and can carry out the same sensing task at a lower cost. The fabrication of SMS structures has also some issues. Presently, there is no means to produce such structures in batches. They are therefore fabricated one by one which means that there may be small variations on the number of modes that participate in the interference and their amplitudes so that repeatability remains an issue.

The aforementioned drawbacks represent opportunities to investigate new fabrication and interrogation approaches or the use of new optical fibers to assemble an SMS structure. In either case, the simplicity of the structure must be preserved to keep its advantages and robustness. Thus, so far, different variants of SMS structures and approaches to improve their sensitivity have been demonstrated by several research groups. These include tapered or etched MMF, combinations of MMFs, a combination of a MMF with a NCF, cascaded SMS structures, etc. In all these cases, the input and output SMFs are identical [98–100].

MCF interferometers. MCFs are waveguides that have several individual cores sharing a common cladding. An MCF can be designed with specific core arrangement and materials to minimize or avoid optical interactions between cores. In this case, the

fiber is called uncoupled or weakly coupled MCF and each core can be considered as an independent waveguide. Uncoupled MCFs were conceived to overcome the capacity limit of the current optical communication system [113]. An MCF can also be designed to allow optical interaction among the cores, for example, by reducing the separation between them. In this case, the fiber is called a coupled-core MCF. The latter supports several supermodes but with certain launch conditions it is possible to excite two supermodes only. In the following section, supermode interferometers based on a coupled-core MCF are discussed in more detail.

MCFs with isolated cores are promising for the development of a myriad of sensors; some are unique or have functionalities that sensors based on single-core fibers cannot achieve. Shape sensors based on weakly coupled MCFs are a good example [114,115]. Such sensors have attracted considerable interest due to their multiple potential applications in the industry and medical sectors. In fact, MCF shape sensors have reached a high level of readiness and are commercially available.

Interferometers can be implemented with uncoupled-core MCFs in three different manners. In one of them, each core of the MCF is an optical path of the interferometer, thus, each individual core of the MCF is interrogated. To do so, expensive fan-in and fan-out devices are necessary. The advantage of multi-path MCF interferometers is that their length can be several meters or kilometers, which makes them good candidates for quasi-distributed sensing [116,117].

The other alternative to make an interferometer with uncoupled-core MCFs is to taper a section of such MCF after being spliced to an input/output SMF [118–123]. The core of the SMF and the central core of the MCF must be aligned. The tapering of the MCF allows the cores of the MCF to get closer and interact. Hence, periodic coupling between the central core and the surrounding cores takes place [118,121,123]. The coupling between the cores depends on the diameter of the cores and their separation as well as on the external medium. Such tapers can, thus, be used for refractive index sensing [121,123]. Gas or chemical sensing is also feasible if the tapered MCF is coated with layers whose refractive index changes when exposed to a gas or chemical substance.

The last possibility to implement an interferometer with uncoupled-core MCF consists of exciting all the cores of the MCF by means of intermediate fibers or a lateral offset [43,124,125]. For example, microscopic segments of MMF spliced between input/output SMF and MCF or by splicing SMF and the MCF with lateral offsets. In this manner, fan-in/out is not necessary but with these launching conditions the insertion losses are high.

Interferometers implemented with tapered or misaligned weakly coupled MCFs may not be a good alternative to devise single-parameter sensors because their fabrication entails multiple steps and the robustness of the MCF is compromised. There is no control on the modes that are excited in a tapered or misaligned MCF either. Hence, the performance of an interferometer may not be predicted or tailored. Therefore, said interferometers cannot be an alternative to those based on conventional single-core fibers.

In addition to these implementations, the concept of a photonic lantern obtained from adiabatically merging several single-mode cores into one multimode core has progressed. It has been largely reviewed in [126] and is not covered further here.

Supermode interferometers. Supermodes are used to describe the modes and optical properties of a MCF for which the cores interact optically with each other. A fused fiber coupler can be considered as the simplest case of a coupled-core MCF. In a

certain region of such a coupler, two single-mode cores can be close to each other and share the same cladding. In fact, the analysis of fused-fiber couplers was done in terms of supermode beating [127–129]. MCFs with strongly coupled cores embedded in a common cladding were demonstrated experimentally in 2014 for high-temperature sensing [130].

In general, the number of supermodes that a coupled-core MCF can support depends on the number of cores that compose the fiber and the number of modes in each individual core. This means that a strongly coupled MCF can be treated as a special form of MMF. However, under certain light launching conditions, it is possible to excite and recombine only two supermodes in the MCF.

The fabrication of a supermode interferometer is similar to that of an SMS structure: a segment of coupled-core MCF is fusion spliced to an input and output SMF. However, there are substantial differences between a supermode interferometer and an SMS structure implemented with an MMF. The most important one is that it is possible to control which of the supermodes participate in the interference. This advantage is important in sensing applications as described in the following.

A supermode interferometer has one of the structures sketched in Fig. 10. Such structures are most often conceived to operate in reflection to facilitate end-point sensing, but the same principles apply in transmission. To fabricate these interferometers, the MCF must have identical coupled cores; one of them is located in the geometrical center of the fiber and the other cores are around the central core. The numerical aperture of all the cores of the MCF is approximately equal to that of the SMF. In this manner, the insertion loss of the SMF–MCF–SMF structure is minimal, no matter the length of the MCF segment.

In the structures shown in Figs. 10(b) and 10(c), the unique core of the SMF and the central core of the MCF are assumed to be axially aligned and in direct physical contact. The SMF is assumed to operate in the single mode regime. Under these conditions, only the two supermodes that have non-zero intensity in the central core are excited in the MCF. The propagation constants of such supermodes can be denoted as β_1 and β_2. They depend on the wavelength (λ) of the incident light, the size of the cores, their separation, and the material of the cores.

Figure 10
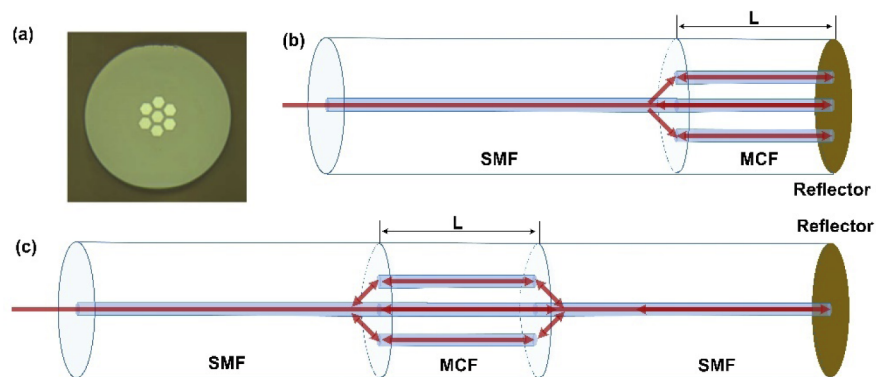
(a) Cross section of a coupled-core MCF. Reprinted with permission from [130]. Copyright 2014 Optical Society of America. (b) and (c) Two possible configurations of supermode interferometers. Here *L* denotes the length of the MCF segment.

The light source, materials, and core arrangement of the MCF can be chosen to tailor the properties of a supermode interferometer. The transmission spectrum of this interferometer can be described with Eq. (3). The reflection spectrum is described with a similar equation, but with $2L$ instead of L. In either case, the interference pattern can be characterized by its visibility (V), which is defined as $V = 2\sqrt{I_1 I_2}/(I_1 + I_2)$. Therefore, after normalization, the reflection of the structure shown in Fig. 10(a) and 10(b) can be expressed as

$$Ra(\lambda, L) = I_{ns}(\lambda)[1 + V\cos(4\pi\Delta NL/\lambda)]/(1 + V)] \tag{5a}$$

$$Rb(\lambda, L) = I_{ns}(\lambda)[1 + V\cos(2\pi\Delta NL/\lambda)]/(1 + V)]^2. \tag{5b}$$

In Eqs. (5), $I_{ns}(\lambda)$ is the normalized power spectrum of the excitation light source. In many cases, the excitation light source is a superluminescent diode (SLED), which has a quasi-Gaussian spectral distribution. The square factor is due to the fact that the transfer function of the MCF interferometer is applied to the light power spectrum twice in the configuration shown in Fig. 10(b).

To predict the interference pattern of a supermode MCF interferometer, it is necessary to calculate the wavelength dependence of ΔN. Thus, Fig. 11 shows the two supermodes that are excited in the MCF when it has seven identical cores.

These two supermodes have a maximum intensity in the central core of the MCF. Figure 11 also shows that the dependence of ΔN on wavelength is linear. Such wavelength dependence can be expressed as

$$\Delta N(\lambda) = a\lambda + b, \tag{6}$$

where a and b are the linear fit coefficients.

The predicted and measured reflection spectra of a supermode interferometer built with the MCF reported in Fig. 10(a) is shown in Fig. 12(a). Figure 12(b) displays the experimental evolution for the structure shown in Fig. 10(b). The spectrum was measured by launching light from an SLED to the MCF by means of a fiber coupler. The

Figure 11
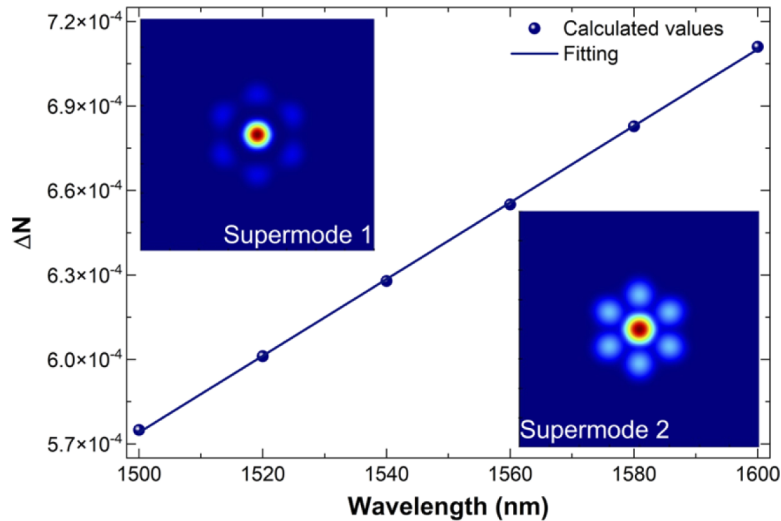
Plot of ΔN as a function of wavelength calculated for the seven-core MCF shown in Fig. 10(a). The solid line is a linear fit. The intensity profiles of the two supermodes are shown in the insets. Adapted from [131].

Figure 12
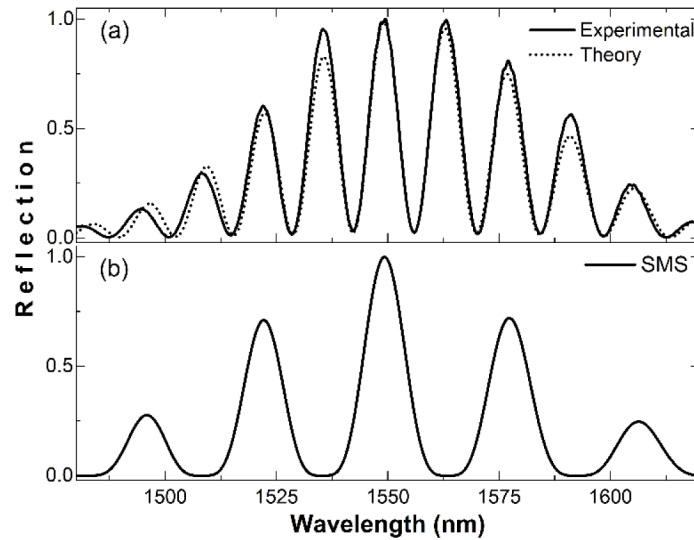
Calculated (dotted line) and measured (continuous line) reflection spectra of a supermode interferometer with (a) the SMF–MCF structure of Fig. 10(a) and (b) the SMF–MCF–SMF of Fig. 10(b) (equivalent to an SMS structure). In all cases, $L = 60$ mm.

reflected light from the cleaved MCF end was analyzed with an optical spectrum analyzer. The values used in the theoretical calculations were: $V = 0.95$, $a = 1.35 \times 10^{-6}$, and $b = -1.456 \times 10^{-3}$. An overall good agreement between the predicted and measured spectra can be appreciated in Fig. 12(a), which confirms that the design of the interferometer can be easily mastered.

Supermode interferometers have been demonstrated for sensing a variety of physical parameters, including high temperature [130,132], bending [26,44,133], vibration [48,134], refractive index [135], and distance [25].

Cascaded modal interferometers. The sensitivity of modal interferometers to more than one parameter may be an issue in practical applications. The influence of temperature, humidity, vibrations, or pressure changes that might be present during the measurement of a target parameter must be compensated for or minimized. Therefore, two modal interferometers in cascade may be necessary. Cascaded interferometers can be arranged in series or in parallel. In either case, one interferometer can be used as a reference and the other as a sensor. However, the transmitted or reflected spectrum of interferometers in parallel or in series is the sum or multiplication, respectively, of their individual spectra. This leads to a complex pattern that may be difficult to decode [136,137]. A practical way to do this, demonstrated in a certain number of cases, is to take advantage of the Vernier effect between the fringe patterns of the two interferometers [138]. A practical example of such strategy involving a triple microfiber coupler interferometer was recently demonstrated to significantly improve the refractive index and temperature sensitivities [139].

Two SMS structures in series, for example, have not been demonstrated yet, probably due to the difficulty in controlling the features of their individual output spectra and their high insertion losses. Tapered fibers in series impose additional challenges in their manufacturing, handling, and packaging.

Figure 13
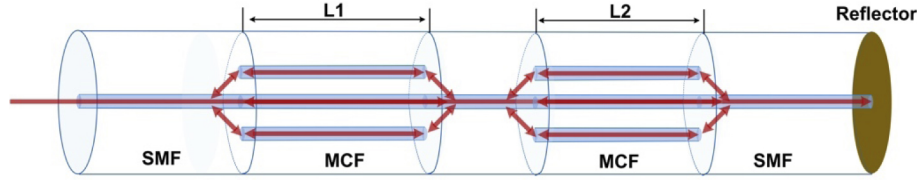
Schematic representation of phase-shifted modal interferometers.

Thus, to use two modal interferometers in cascade for sensing a single parameter it is important to ensure control on the modes that participate in the interference as well as on the fabrication steps of the interferometers.

Phase-shifted modal interferometers. The concept of phase-shifted modal interferometers was introduced in 2020 [134,140,141]. The idea consists of placing two supermode interferometers in series, but the interferometers must have a proper difference in their lengths. Figure 13 shows a schematic representation of two phase-shifted interferometers. The main requirement is that one interferometer has a length L_1 and the other a length L_2 that is linked to L_1 as $L_2 = L_1 + L_0$ or $L_2 = L_1 - L_0$. Thus, the phase difference between the two supermode interferometers will be $\delta\phi = 2\pi\Delta N L_0/\lambda$, which is restricted to be bigger than zero and smaller than π. This means that the values of L_0 are restricted to be

$$0 < L_0 < \lambda/(2\Delta N). \qquad (7)$$

Proper lengths of the two supermode interferometers can be selected as follows. First, the lengths of MCF that give transmission or reflection maxima are found. From Eq. (4) we can notice that this happens when the length of the MCF segment satisfies the following condition:

$$L_m = m(\lambda/\Delta N), \qquad (8)$$

where m is an integer number. Thus, the lengths of MCF are as follows:

$$L_1 = m(\lambda/\Delta N) + L_0 \qquad (9a)$$

$$L_2 = m(\lambda/DN) - L_0. \qquad (9b)$$

For example, if a single maximum is desirable at a particular λ, ΔN must be calculated at such a λ for the particular design of MCF that is used to fabricate the interferometers. To make the devices as short as possible, the value of m must be small. It is interesting to note that in the above equations, L_1, L_2, and L_0 depend on ΔN. For this reason, it is important to have full control on the modes that participate in the interference.

Figure 14 displays the reflection spectra of individual supermode interferometers (dotted lines) when a single device of length L_2 or L_1 was in the configuration shown in Fig. 10. The spectrum when both devices were in series is shown with the shaded area. Such spectrum results from the multiplication of the individual spectra that compose the series [140].

Let us now assume that one supermode interferometer is perturbed by a parameter we want to sense and the other is not. The pattern of the perturbed device will shift and the other will be unaltered. Consequently, the height of the peak of the spectrum of the two devices in series will change. Therefore, by monitoring intensity changes it will be possible to sense the parameter that perturbs one interferometer.

Figure 15 shows the measured intensity changes observed when one supermode interferometer was bent and the other was kept straight. The devices were fabricated with

Figure 14
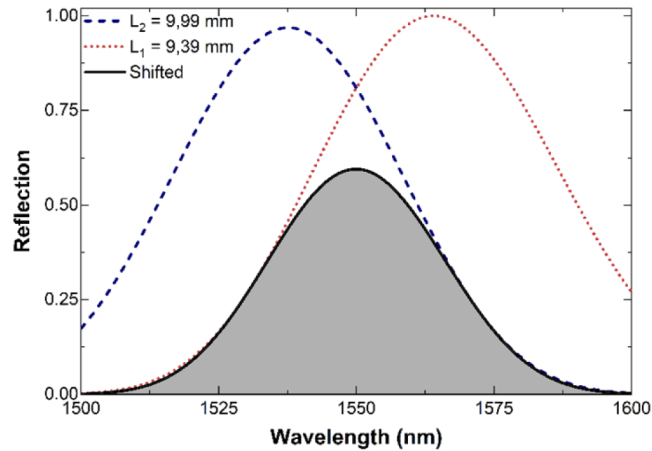
Simulated reflection spectra of individual and phase-shifted supermode interferometers. The lengths of the MCF segments are indicated.

the seven-core fiber shown in Fig. 10(a) and the configuration is as shown in Fig. 10, with $L_1 = 12.7$ mm and $L_2 = 11.7$ mm. Note that a small bending angle results in quantifiable intensity changes. The advantage in this case is that there is no need to find the point of quadrature and a low-cost SLED can be used instead of a tunable laser. Moreover, intensity changes can be monitored at high speed with a suitable photodetector. Phase-shifted supermode interferometers are suitable for sensing vibrations, acoustic waves, or any event that may bend one interferometer [41,141].

There are several issues that must be investigated before phase-shifted interferometers find practical applications. The effect of temperature has not yet been investigated in detail. Temperature will shift both interference patterns in the same proportion as the devices are made of the same MCF and have similar lengths. Therefore, temperature may not cause intensity changes. The sensitivity of phase-shifted supermode interferometers to other parameters or to the use of other types of optical fibers has not yet been demonstrated. Several research opportunities remain open in this area.

Figure 15
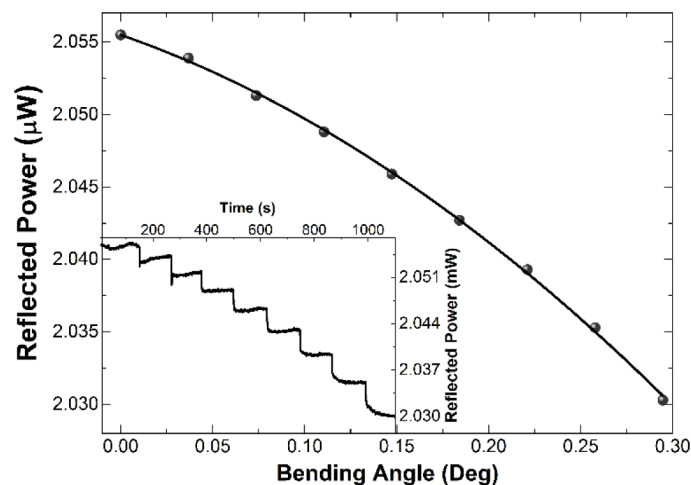
Changes in the reflection power observed in phase-shifted supermode interferometers when one of them was bent by a small angle. The inset shows the evolution of the reflected power as a function of time.

2.4. Surface Plasmon Resonances

Thin film-coated optical fibers have been widely studied and developed over the past two decades. Among the various possibilities in terms of coatings, metal-coated configurations remain to date the most common because of the possible excitation of high sensitivity surface plasmon resonances (SPRs) on metal surfaces, especially in the biochemical domain [8]. Basically, such devices become highly selective of refractive index changes near the metal surface. The SPR phenomenon appears when a noble metal film of appropriate thickness (typically between 30 and 70 nm) is deposited on the fiber outer surface at a modified location (e.g., an unclad section, a strongly bent section, or a section with a fiber grating) where an evanescent wave from the fiber is coupled into the metal layer. The conditions required to excite SPR are: (1) phase matching between the evanescent field of the fiber and the surface plasmon polariton mode of the metal-surrounding medium interface; and (2) having at least part of the evanescent field of the fiber polarized radially, which is the only possible polarization of the surface plasmon. This phenomenon manifests itself as an unambiguous resonance in the transmission spectrum of the fiber. In the first implementations of SPR on fibers and many times since, a subset of the guided modes of highly multimode and cladding-removed fibers are sufficiently phase- and polarization-matched to a surface plasmon polariton to give rise to a relatively broad loss resonance of a few tens of percent in transmission. As this is not, properly speaking, a multimode sensing principle, it is not discussed further.

What is discussed is the use of fiber gratings to probe the SPR via well-controlled modes selectively excited by the gratings. Owing to the spectral breadth of the SPR, there can be many modes of a relatively thick underlying fiber with effective indices at least partially phase-matched to the SPR. The effective indices of these modes have much increased sensitivity to surface refractive index changes, reflected in wavelength changes of the corresponding grating resonances, and the resonances also exhibit large-amplitude changes because of the delocalization of the mode fields away from the fiber core and towards the outer metal surface [78]. As a result, many exciting new sensing methods have been developed to take advantage of the differential sensitivities of these plasmon-hybridized modes, as described in Section 3.6.

2.5. LMRs

LMRs, previously called guided-mode resonances, arise when optical fibers are coated with thin films having refractive indices larger than that of the fiber and surroundings, and also do not absorb excessively. Even in the absence of gratings, and similarly to SPR, LMRs occur when light guided by the underlying fiber couples synchronously to a mode of the thin coating: the result is an apparent loss of light at certain wavelengths of the transmission spectrum [68]. In contrast to SPR, however, both TE and TM modes can be excited in the thin coating so that slightly different resonances are observed using polarized input light, with a wavelength spacing that depends on the guiding properties of the coating. Furthermore, increasing the thickness of the coating can lead to higher-order modes appearing, with corresponding additional resonances in transmission [68]. LMRs were observed both for semiconductor and dielectric claddings [142,143]. Appropriate materials for LMR generation are indium tin oxide, titanium dioxide, indium oxide, aluminum-doped zinc oxide, zinc oxide, and polymers, with several applications reviewed recently by Chiavaioli and Janner [144].

Finally, even at thicknesses too small for the coating to support guided modes, it has been shown that it can modify the dispersion curves of the underlying fiber modes in a way that produces anomalous wavelength shifts of grating resonances in such fibers [145,146]. Apart from providing a great way to measure nanoscale thickness coatings

Figure 16
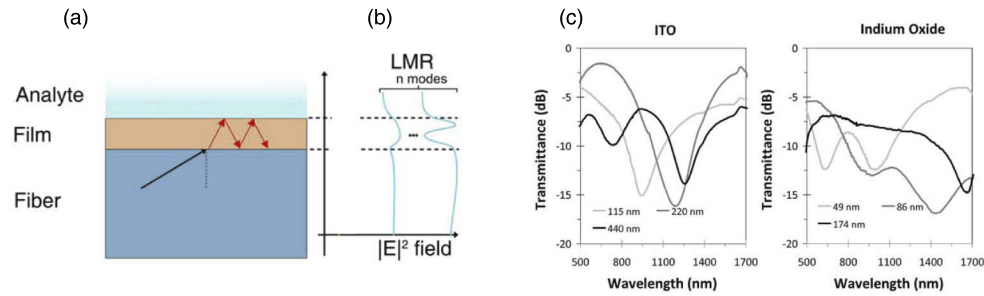
(a) Light guided by a fiber impinging on a coating with a refractive index higher than that of the fiber and of the surrounding, thereby preventing total internal reflection at the fiber surface and allowing coupling to guided modes of the coating if it is thick enough to support guided modes at the wavelengths used. Reprinted with permission from [144]. Copyright 2021 Optical Society of America. (b) Mode field sketches showing LMR resonances. (c) Exemplary LMR observed experimentally in cladding-removed multimode fibers with indium tin oxide and indium oxide. Reprinted from Villar *et al.*, J. Opt. **12**, 095503 (2010) [146]. © IOP Publishing. Reproduced with permission. All rights reserved.

in situ, the sensing properties of these dispersion modified fibers have yet to be studied (Fig. 16).

2.6. Fiber Gratings
2.6a. Periodic Refractive Index Modulation
A periodic perturbation of the fiber along its axis defines a grating that can be used to transfer power from one propagating mode to another, or from a forward mode to a backward one in a SMF. This exchange of power is also described by a coupled-mode formalism which states that efficient power coupling can only occur if the following phase matching condition is met [145–147]:

$$N_1 \pm N_2 = \lambda/\Lambda, \qquad (10)$$

where N_i are the effective indices of the modes exchanging power at wavelength λ, and Λ is the dominant period of the longitudinal perturbation (usually the first term of the Fourier expansion of any periodic perturbation along the fiber axis). This form of the equation describes how a forward propagating mode with effective index N_1 couples to another mode N_2 propagating in the direction specified by the $\pm$ sign [forward (−) or backward (+) relative to the incident mode direction]. Because they can couple between different modes, gratings can be used for both multicore systems and single-core, multimode systems, and, as just noted, they can couple bi-directionally.

Fiber gratings can be divided in two broad categories. As fiber modes have effective index values generally bound between 1.0 and 1.45 (for glass fibers), Eq. (6) shows that when the period of the perturbation is larger than the wavelength ($\lambda/\Lambda < 1$), the modes being coupled must be propagating in the same direction (co-directional coupling); these are referred to as "long-period gratings" (LPGs) [148,149]. The opposite ($\lambda/\Lambda > 1$) requires that N_1 and N_2 have the same sign, leading to contra-directional coupling. These short-period gratings are known as FBGs [150,151].

Many of the most widely used point fiber sensor technologies are all based on FBGs and commercially viable sensing solutions are marketed by several tens of companies worldwide. The vast majority of FBG sensors are produced by ultraviolet (UV) irradiation in high-quality but very inexpensive telecommunication-grade single-mode

Figure 17
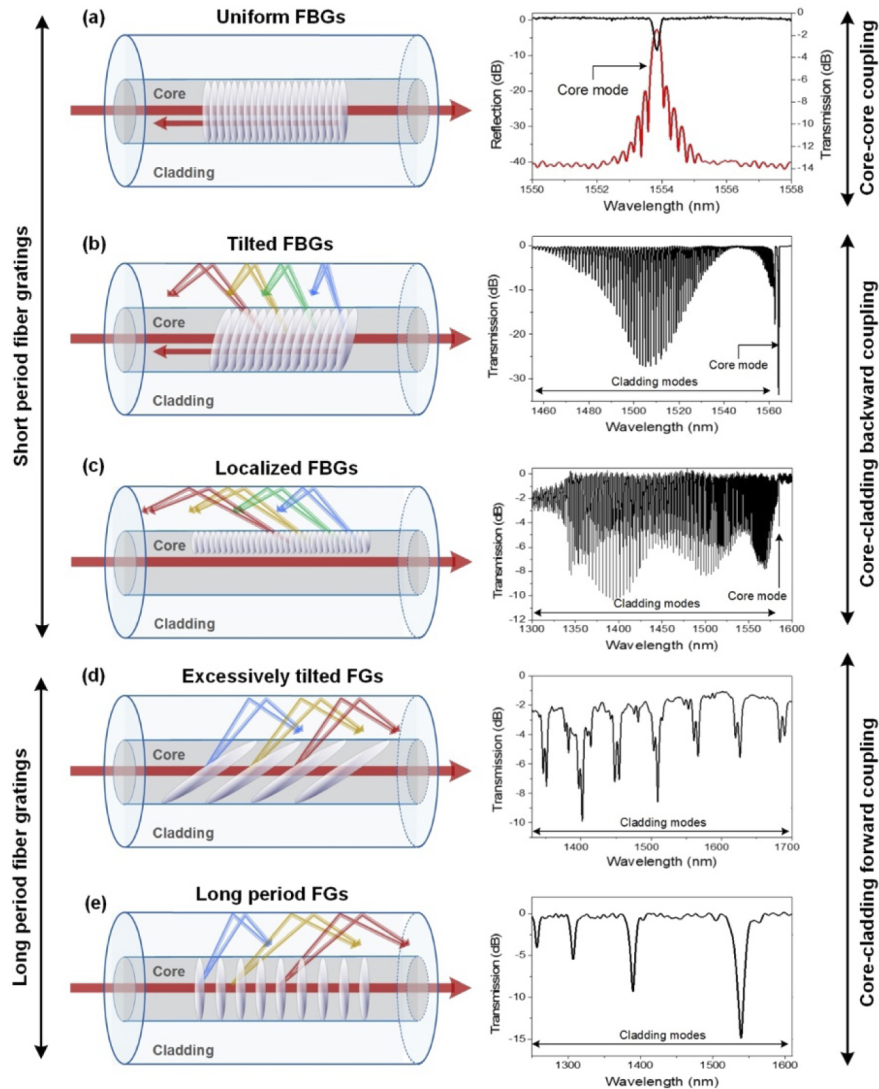
Four kinds of fiber gratings classified according to their grating period and mode coupling (left, operating principle mechanisms; right, corresponding transmitted amplitude spectrum). For uniform FBGs, the reflected amplitude spectrum is also depicted in red. Reprinted from [157] under a Creative Commons 4.0 License.

optical fiber [152] and they have shown to provide reliable measurements of temperature, strain, and pressure. Gratings in polymer optical fibers (POFs) have also emerged since the late 1990s, first in (PMMA) [153] and then in other materials under the commercial names CYTOP [154], TOPAS [155], and ZEONEX [156].

Recent advances deal mostly with gratings designed to couple between more modes and in specialty fibers, most often produced with femtosecond pulsed laser sources because these can write refractive index gratings in a much wider variety of glasses and other materials such as polymers. In the context of the present review, FBGs and variants can be used for contra-directional coupling between the modes of a multimode structure or as "conventional" core-mode back-reflectors in the different cores of a MCF.

In the following sections, we present the four types of gratings in terms of mode coupling that are illustrated in Fig. 17.

2.6b. Short-Period Gratings (FBGs)

A permanent, uniform FBG is usually produced in the core of an SMF by exposure to an interference pattern of intense UV light through the exploitation of a photosensitive mechanism [148]. Pulsed excimer lasers at 248 or 193 nm and frequency-doubled continuous-wave argon lasers at 244 nm are commonly used. Although "photosensitive" fibers (with higher germanium doping) are available from specialty fiber suppliers, normal SMF is often used, provided it is rendered more photosensitive by first diffusing hydrogen gas into it [158,159].

As sketched in Fig. 17, a standard core mode back-reflector FBG is defined by three main parameters: L, the physical length along which the modulation is created (usually between 1 mm and a few centimeters); Λ, the period of the refractive index modulation; and δn, the amplitude of the refractive modulation (usually between 10^{-5} and 10^{-3}). Light is reflected over a small bandwidth around a central wavelength called the Bragg wavelength, which is determined by the following relationship:

$$m\lambda_B = 2N_{core}\Lambda, \tag{11}$$

where m is the grating order ($m = 1, \ldots, M$) and N_{core} is the effective index of core mode at the Bragg wavelength λ_B. For an effective coupling at 1550 nm, the period of the first-order grating ($m = 1$) is of the order of 530 nm because $N_{core} \sim 1.447$ for a standard fiber at that wavelength. The amplitude of the resonance increases with L and δn while the full width at half maximum (FWHM) is proportional to δn but inversely proportional to L. A 1-cm-long FBG will have a FWHM of ~200 pm and therefore a resonance quality factor ($\lambda/\Delta\lambda$) of the order of 10^4.

The grating transfer function for the input mode field wave is a complex quantity. The real part yields the amplitude response whereas the imaginary part contains the phase information. The amplitude reflection spectrum corresponds to the Fourier transform of the refractive index modulation profile. Hence, for a first-order grating at 1550 nm, there are higher orders at smaller wavelengths ($m = 2$ around 775 nm, $m = 3$ around 517 nm, etc.). FBG sensing is largely based on the amplitude response of uniform gratings, but some more-sophisticated sensing modalities make use of the phase spectrum, especially with gratings that include period discontinuities, multiple periodicities, and amplitude profiling (apodization, for instance).

Two main methods coexist for FBG inscription with respective assets and limitations: the transverse holographic technique and the phase mask technique [159,160]. The former uses an interferometer that splits the incident laser beam into two divergent beams that are then recombined by lenses and mirrors to interfere at the fiber location where the inscription takes place. The grating period can be easily tuned by modifying the incident angle of the two laser beams, but a good laser spatial coherence and setup stability are required for a proper operation of the technique. For the phase mask technique, a periodic groove pattern is photolithographically etched into a UV transparent (fused silica) substrate. The groove depth is designed to diffract an incoming UV laser beam into the +1 and –1 diffracted orders (and as little as possible light in the zero-order, straight-through direction). As a result, an interference pattern with a power modulation period that is exactly half that of the phase mask is produced near its surface, where the fiber is positioned. The phase mask method is necessary for use with excimer laser sources because of their low spatial coherence which precludes the use of the transverse holographic technique. It is also appreciated for not requiring stringent alignment and the high reproducibility of FBG parameters it produces. This is especially important in the notoriously cost-sensitive sensors field. The only drawback of the phase mask method is the need to purchase or fabricate a new phase mask in order to change the wavelength of the FBG. The NORIA system from Northlab

Photonics uses an excimer laser, all the optics, fiber-handling spools, and a revolving platform with 16 slots for phase masks: it is sold as a semi-automated FBG production platform. Other FBG fabrication tools are integrated and further industrialized: draw tower gratings (DTGs) can even be produced in a reel-to-reel system during the fiber drawing [161]. They are the ultimate solution to produce a cable containing tens to hundreds of cascaded wavelength-division-multiplexed or time-division-multiplexed FBGs. They can also be used to mass-produce individual gratings at relatively low cost.

Aside from these classical writing methods, the advent of femtosecond pulsed lasers has allowed alternative gratings production using phase masks and through the development of the point-by-point, line-by-line, and plane-by-plane techniques [162–165]. There, the laser beam is focused through a microscope objective (in index-matching oil or in air) towards the fiber location where the inscription (a controlled glass damage process) can take place. As the laser is pulsed, the stepwise translation of the fiber according to the pulse rate allows to pattern the glass modification and thereby create a controlled refractive index modulation. Gratings can also be located away from the core or partly offset from the fiber axis in a three-dimensional fashion because traditional photosensitivity mechanisms are no longer required to produce permanent, subwavelength-scale refractive index modifications in just about all kinds of transparent materials. This technique is certainly the most flexible to date and allows to produce many more structures in optical fibers than standard fiber grating technologies.

A uniform FBG is intrinsically sensitive to temperature changes and axial strains, as both parameters modify the effective refractive index and the grating period [166]. This results in a wavelength shift of the FBG reflected amplitude spectrum, without modification of shape, when uniform perturbations are applied along the grating length. The sensitivities vary with the Bragg wavelength, the fiber composition, and the grating type. For an SMF-28 at 1550 nm, the temperature sensitivity is close to 10 pm/°C whereas the axial strain sensitivity is of the order of 1 pm/$\mu\varepsilon$. Because of its composition and the normal photosensitive process, a standard FBG will be erased at temperatures in the range of 250–400 °C. These standard FBGs are referred to as Type I gratings. The temperature stability issue can be avoided by using different photosensitive processes. Most notably, Type IA gratings are produced by "regeneration" of a FBG upon thermal treatment at high temperatures for typically several hours [167]. Another commonly used technology for high-temperature resistant gratings is the Type II, or so-called "damage" grating resulting from a single pulse of very intense UV light [168]. The pulsed femtosecond laser process described earlier can be considered as more advanced, more controlled form of damage gratings and they also support higher operating temperatures without degradation, up to 1100°C in some cases. All these approaches (and many other less-common techniques) are also applicable to the fabrication of the other types of resonant structures described in this section.

FBGs are weakly sensitive to isostatic pressure and their sensitivity at 1550 nm is close to ~4 pm/MPa. Pressure sensing is then usually obtained with specialty fibers (especially microstructured and polymer fibers) or with swelling hydrogels surrounding the gratings. The addition of a sensitive layer around an FBG widens the sensing modalities and opens the door to chemical sensing. The role of this layer is to transduce the chemical species to be detected (in liquid or in gas) into a parameter that can be measured by the grating, i.e., a temperature change or a strain [169,170]. Uniform FBGs are not inherently sensitive to bending as the refractive index modulation is made on the neutral strain axis of the fiber. However, when attached to a structure to monitor and provided that they are not placed on the neutral axis of the said structure,

they can measure the bending of the latter through extension and compression, as obtained with electrical strain gauges.

Uniform FBGs are not intrinsically sensitive to changes of the surrounding refractive index (SRI) because light remains confined in the core and does not enter into contact with the outer medium. The sensitivity arises for thinned FBGs where the cladding is removed totally or in large part to expose the core evanescent wave to the surroundings, following an etching process (usually with hydrofluoric acid) or a mechanical polishing. Unless the fiber is thinned almost down to the core, the sensitivity is still very weak in water solutions because the mismatch between the effective refractive index of the core mode (~1.447) and that of water (~1.319) is large and, therefore, the evanescent field of the mode does not much penetrate the surrounding. Other configurations such as long-period fiber gratings (LPFGs) and TFBGs are much more suited to this aim, as they access higher-order modes with effective indices closer to that of the sensing medium [78,171,172].

FBGs can also be used for transverse strain sensing, but the readout technique relies in this case on the birefringence effect [173]. The application of a transverse force increases the linear birefringence, resulting in an increase of the wavelength splitting between the two reflected amplitude spectra: the amount of lateral force can be determined from the measurement of the increase in wavelength separation between both spectra. This technique is not typically used for glass fibers because of their large Young's modulus and relatively small photo-elastic coefficients, but a metrology based on the polarization-dependent loss (PDL) spectrum measurement is a good alternative in this case as it is more effective in revealing small polarization-induced wavelength shifts [174].

2.6c. LPGs

As described in Section 2.6.1, subwavelength grating periods lead to contra-directional coupling, but gratings with periods of several times the wavelength and more couple modes that travel in the same direction in the fiber. In addition, because of the longer period (typically between 100 and 500 μm), an LPFG can be fabricated much more easily than an FBG, even using periodic heating with fiber fusion tools. LPFGs were popularized after an initial report by Vengsarkar *et al.* in 1996 about periodic structures able to couple the guided fundamental core mode of a SMF into forward-propagating cladding modes [149]. This type of grating is a fiber analog of the previously known grating-assisted directional couplers and mode converters [130]. Since cladding modes decay rapidly as they propagate along the fiber axis because of scattering losses at the cladding–surrounding medium interface and that they are strongly perturbed by bending, they can only be used over short distances, which is not a problem in sensing. Similar to FBGs, the coupling in LPGs is wavelength-selective and cladding mode resonances appear in the transmitted amplitude spectrum of an LPFG at the following central wavelengths:

$$\lambda_{clad,i} = (N_{core} - N_{clad,i})\Lambda, \tag{12}$$

where $N_{clad,i}$ is the effective index of the *i*th cladding mode. The transmitted amplitude spectrum of an LPFG is composed of several well-separated broadband (FWHM ~10–50 nm) resonances, as depicted in Fig. 17. The wavelength positions of these bands depend on the grating period and the order of the resonances increases from left to right, in agreement with Eq. (12).

Although the sensitivities of LPG resonances are based on the same principle as those of FBGs, there are two important differences: the cladding mode resonances are sensitive to bending and to the SRI, and they are significantly more sensitive in

Figure 18
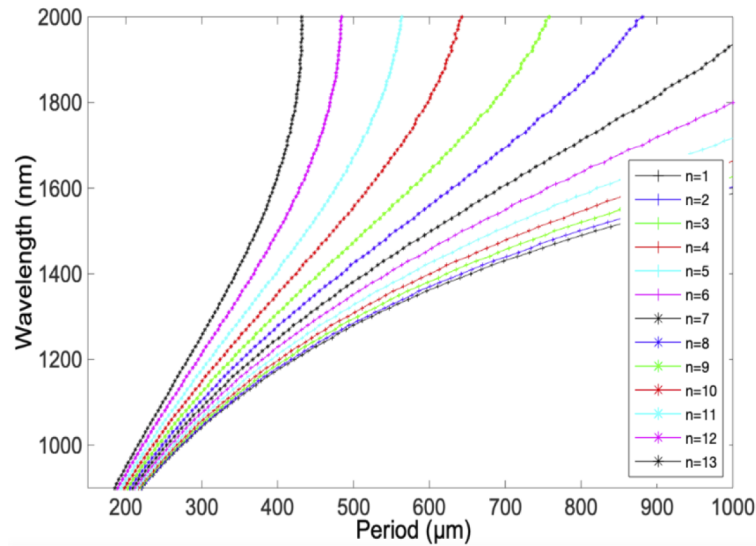
Phase matching curves for an LPFG in a SMF-28.

general because the wavelength shifts depend on the difference of the mode dispersions (instead of their sums in FBGs).

In fact, the sensitivity of these gratings greatly depends on the grating period value. Dispersion curves drawn in Fig. 18 indicate the presence of a so-called turnaround point (TAP) for higher-order cladding modes where the slope of the curve changes sign from positive to negative [175]. LPFGs featuring resonances at these TAPs become highly sensitive to perturbations, including SRI change, as the slope $d\lambda_{res}/d\Lambda$ of the dispersion curve reaches infinite values. For lower-order modes, the TAPs occur at longer wavelengths, beyond the optical telecommunication window.

LPFGs can be manufactured following different ways. Making use of an amplitude mask (usually made of metal) containing periodic apertures corresponding to half of the grating period as well as point-by-point UV or CO_2 laser irradiation are popular techniques for making LPGs. LPFGs can also be produced mechanically by pressing fibers between grooved plates or by using longitudinally distributed electric arc discharges (from a fusion splicer, for instance). In the context of this review, and apart from the fact that there are at least two modes involved (the core mode and a given cladding mode), LPFGs are rarely (if ever) used in multimodal sensors because their resonances are too widely separated and their relative dispersions so sensitive that it becomes impossible to design efficient sensors based on multiple resonances.

2.6d. Ex-TFGs

Other configurations share with LPFGs the principle of using the cladding modes of a SMF for sensing. The most similar are the so-called Ex-TFGs that were first proposed in 2006 at Aston University in the UK and used extensively since [176,177]. Typical Ex-TFGs have periodically slanted refractive index planes inclined more than 66.9° with respect to the normal optical fiber axis. Even when the grating period (perpendicular to the grating planes) is short, the large angle lengthens the axial period by $1/\cos\theta$, bringing it to the co-directional coupling regime. The usual resulting period is typically around tens of micrometers and, therefore, supports the excitation of higher-order cladding modes. Because of their slanted nature, Ex-TFGs introduce an intrinsic birefringence in the core, so that orthogonal polarizations corresponding to TE and TM modes are well resolved spectrally. The phase matching conditions for

Figure 19
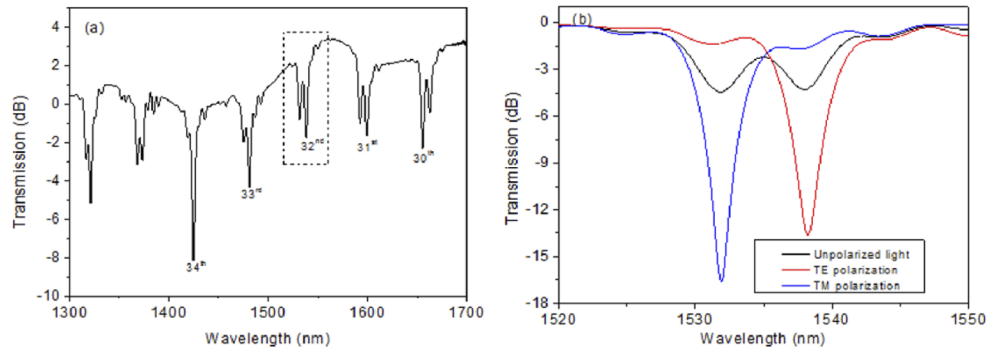
Transmitted amplitude spectrum of an 81° TFG: (a) dual-peak resonances observed with unpolarized light launched in the core; (b) enlarged view of one dual reso-nance and its identification with one EH(TM) and HE(TE) mode pair. Reprinted with permission from [77]. Copyright 2016 Optical Society of America.

Ex-TFGs can be expressed as follows:

$$\lambda_{clad,i} = (N_{core} - N_{clad,i})\Lambda_z, \tag{13}$$

where Λ_z denotes the grating period along the fiber axis.

The phase mask technique, popular for uniform FBGs inscription, and the point-by-point technique, usually preferred for LPFGs inscription, are not suited to produce Ex-TFGs. The amplitude mask method is the most used in practice: an amplitude mask is tilted by the required angle in front of the fiber and the grating structure is produced by the direct laser beam. There is a one-to-one correspondence between the tilt angle and period of the mask and those of the inscribed grating [77].

A typical spectrum of an Ex-TFG measured with unpolarized light is shown in Fig. 19. A series of resonances can be seen in the wavelength range 1300–1700 nm, with bandwidths and wavelength separations similar to those of LPGs, except for the fact that each resonance appears to be split in two.

Additional measurements with LP core guided input light in Fig. 20(b) further show that the splitting corresponds to the separate excitation of the EH/TM group and HE/TE group by input light polarized in the plane and out-of-the-plane of the tilt, respectively [77,178]. The observed splitting is due to the break in cylindrical symmetry of the fiber associated with the formation of the tilted grating. Ex-TFBGs exhibit a higher refractive index sensitivity and a lower temperature sensitivity compared with LPFGs, resulting from the excitation of higher-order cladding modes (i.e., with somewhat shorter axial periods).

2.6e. Tilted Short-Period Gratings (TFBGs)
TFBGs belong to the short-period gratings family and, as Ex-TFGs, they are character-ized by a refractive index modulation angled with respect to the perpendicular to the optical fiber axis. The main difference from Ex-TFGs is that the tilt angles are relatively smaller (less than 40° and typically much less, between 4° and 15°), and as a result their axial period is short and the gratings belong to the contra-directional coupling regime [78]. TFBGs can be manufactured following the same tools and techniques as uniform FBGs and their production benefits from over 20 years of engineering advances in mass production and quality-control processes. When the phase mask technique is involved, two main options can be pursued to produce TFBGs: (1) the phase mask is tilted in the vertical plane perpendicular to the laser beam while the fiber

Figure 20
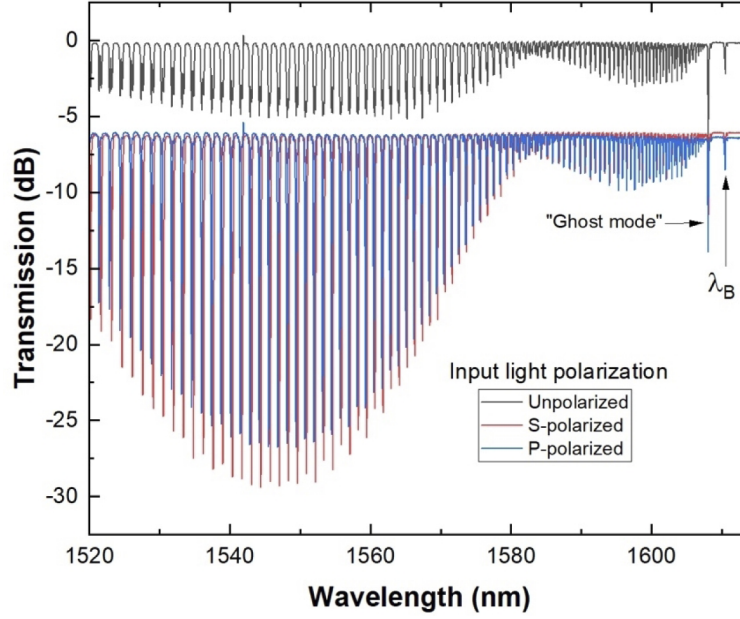
Transmission spectra of a 1-cm-long 10° TFBG measured in air, with different input light polarization states (spectra offset vertically for clarity).

is kept horizontal or (2) both the fiber and the phase mask are tilted in the direction of the laser beam. A refractive index modulation tilted with respect to the perpendicular to the optical fiber axis drastically enhances the coupling to cladding modes. Hence, when the HE_{11} mode of a SMF meets the blazed refractive index modulation of a TFBG, two kinds of optical coupling take place: the self-backward coupling of the core mode at the Bragg wavelength and multiple backward couplings between the core mode and cladding modes, as light propagation in the cladding is intrinsically multimode.

The core mode coupling appears at the Bragg wavelength while cladding mode couplings appear at well-defined shorter resonant wavelengths. They are respectively given by the following relationships:

$$\lambda_B = 2N_{core}\Lambda_z \tag{14}$$

$$\lambda_{clad,i} = (N_{core} + N_{clad,i})\Lambda_z, \tag{15}$$

where Λ_z still represents the projection of the grating period along the fiber axis (which is related to the period of the interference pattern of the laser beam differently depending on the tilt configuration).

Figure 20 depicts a typical transmission spectrum of a 10° TFBG, measured with a tunable laser-based swept-wavelength measurement system using unpolarized light and also light polarized along the S and P directions relative to the tilt of the grating planes. Cladding mode resonances can only be seen in transmission mode, as the optical power carried by these modes gets stripped away by the lossy jacket and various optical components (connectors and couplers) used to collect the reflected light. It can be seen that the Bragg wavelength is located at the right-hand side of the spectrum while several tens of narrowband cladding mode resonances range below. The value of N_{core} depends on the operating wavelength because of waveguide and material dispersion. It can be considered to be equal to 1.447 at 1550 nm for an SMF-28 optical fiber. The cladding mode resonance order increases from right to left, according to Eq. (15),

and the corresponding mode effective index decreases. At a ~70 nm distance on the short wavelength side of the Bragg resonance, the effective index of the corresponding cladding mode matches the refractive index of water at that wavelength (near 1.319) [179]. The first cladding mode resonance to the left of the Bragg resonance is the so-called ghost mode as it shares many properties of the Bragg resonance but is actually composed by the overlap of several low-order nearly degenerate cladding mode resonances [78]. The multimodal nature of a TFBG mainly depends on the tilt angle value: the higher the angle value, the higher the extension of the range of measurable cladding mode resonances towards shorter wavelengths. It was recently demonstrated that for tilt angles of the order of 20° or more, cladding mode resonances extend almost uniformly over a few hundreds of nanometers [180]. The high-order cladding mode resonances located more than 220 nm from the Bragg resonance have effective indices lower than 1 and they show the corresponding signature from resonances no longer guided by total internal reflection at the cladding–surrounding interface (i.e., a sudden increase in amplitude and background loss, and some widening). Such gratings are therefore very well suited for refractometry in gas phase because cladding modes near cut-off with strong evanescent field penetration in gas can be excited [180].

Figure 20 also shows that higher-order mode resonances also split according to the polarizations of the underlying mode groups, as in Ex-TFGs, and for the same reasons, with the important difference that they are much more densely occurring in the spectrum, and that they have much narrower bandwidths, typical of FBGs. For a detailed view of the mode splitting, see Fig. 3. The large diminution in the resonance amplitudes in the unpolarized measurement (of the same grating) stems from the fact that in this case, only half the light is in the correct polarization for each of the resonances that couples to either S or P modes (for high-order resonances that are spectrally separated): this brings the maximum attenuation in each resonance to no more than 50% (i.e., –3 dB in transmission), or a little higher due to partial overlap of neighboring resonances.

2.6f. Localized FBGs

An alternative to TFBGs that shares many of their characteristics has been reported using highly localized grating inscription techniques relying on point-by-point femtosecond pulsed laser irradiation [74,75,181,182]. Instead of grating planes extending across the fiber core, smaller dimension periodic structures along the fiber axis can be localized anywhere in the fiber cross section, and in this particular case away from the fiber core. As in TFBGs, this breaks the cylindrical symmetry of the core and, thus, couples a forward-propagating core mode to a very large number of backward-propagating cladding modes. Unlike TFBGs, however, where the amplitudes of the cladding mode resonances strongly depend on the tilt angle, peaking at a specific distance from the Bragg resonance, localized FBGs generate an apparently infinite number of cladding mode resonances extending for hundreds of nanometers from the Bragg wavelength with approximately equal amplitudes. Figure 21 shows the measured transmission spectrum of such grating with air as the surrounding medium.

2.6g. Sensing in Multimodal Systems with Fiber Gratings

Theoretical considerations. Both LPG and FBG devices have been used extensively in sensing applications because the wavelengths at which resonances occur can be measured easily and accurately using widely available and relatively inexpensive instrumentation. Furthermore, resonance wavelength and amplitude shifts occur whenever the fiber mode fields and effective indices are perturbed, by changes in or around the fiber. Finally, gratings allow core guided light to be coupled to selected cladding

Figure 21
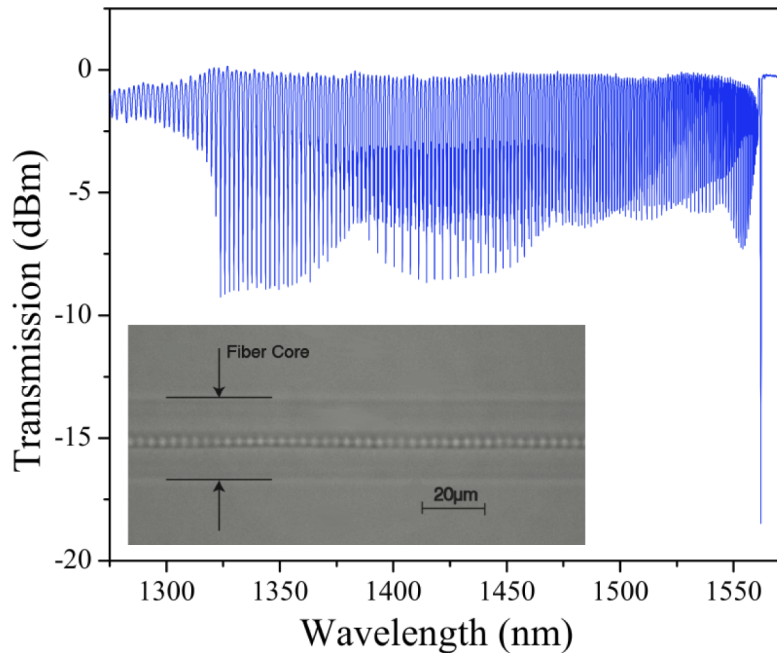
Transmitted power spectrum of a localized FBG. Inset: micrograph of the refractive index modulation strongly localized in the core.

modes or groups in order to probe the fiber and its surroundings with specific light distributions and polarization states.

Within grating-based sensors, there is an interesting trade-off between co-directional (LPGs and Ex-TFGs) and contra-directional gratings (FBGs, TFBGs, and localized FBGs). The modal resonance widths of typical contra-directional gratings lie between 0.1 and 1 nm (for gratings of a few millimeters in length) and, thus, have large quality (Q) factors (resonance wavelength/resonance width) between 10^3 and 10^4, which facilitates the accurate determination of small wavelength shifts. However, their relative wavelength shift sensitivity to a perturbation "x" (($\Delta\lambda(x)/\lambda$) is proportional to $\Delta N(x)/(N_1 + N_2)$, i.e., of the order of $\Delta N(x)/N$. Co-directional grating resonances on the other hand have widths between 10 and a few 100 nm, i.e., much lower Q factors (10–100). However, their relative wavelength shift sensitivity is proportional to $\Delta N(x)/(N_1 - N_2)$, which is potentially orders of magnitude larger than that of FBGs (for coupling between modes with similar effective indices, i.e., Λ very large relative to λ). What matters in the end is the limit of detection, which is equal to the ratio of the smallest wavelength shift that can be detected reliably to the wavelength shift sensitivity. Although co-directional gratings largely win on sensitivity, their Q factors and limits of detection are not superior to those of FBGs and other short period gratings.

So, what makes a grating become a sensor? Predominantly two effects:

(1) a change in the effective index of one (or both) of the modes being coupled, or of the grating period, will change the wavelength at which a resonance occurs.
(2) a change in the complex permittivity or dimensions anywhere within the waveguiding structure will change the mode profiles and therefore the coupling coefficient between modes, including mode loss, resulting in a change in the resonance amplitude.

What is relevant in the context of this review is the fact that in a multimode system, different modes (or modes of different cores) may have different sensitivities to each kind of perturbation and the simultaneous measurement of several resonances can be used for: (a) multiparameter sensing, (b) dealing with cross-sensitivities (temperature, for instance), (c) improving the limits of detection by using multiple resonances to measure a given parameter and, thus, averaging out the measurement noise from each of the resonances. We have also established that in multimode systems, it is possible to enhance the coupling between different groups of modes through the use of gratings that break the cylindrical symmetry of the fiber. The main consequence of this is an opportunity to optimize the grating response for specific measurands. The break in symmetry also enhances the polarization dependence of the grating responses and opens up new sensing modalities, in bending and lateral force sensing for instance, as well as in plasmonics for fibers with metal coatings.

Mode sensitivity simulations. The development of point fiber optic sensors has traditionally relied on experimental determinations of sensitivities. In practice, it is much easier to test out and calibrate the response of sensors than to predict them theoretically. This being said, a good theoretical model of a sensing modality can serve two purposes: optimizing the sensor design by predictive calculations instead of trial and error; and, more importantly, extracting more-accurate information from measured data.

In the following, we use simulations of the multiresonant transmission spectrum of a TFBG to demonstrate model-based sensor interrogation techniques. The first step in the process is to model the TFBG transmission spectrum in a known state, i.e., a state where all the parameters of the fiber waveguiding structure are as well known as possible. The fiber chosen for the device is a CORNING SMF-28 without its jacket and in air at 23°C and atmospheric pressure. The waveguiding structure at wavelengths near 1550 nm is then defined by the refractive index and dispersion of pure silica for the cladding, and a core index difference of 0.35% [183], and the refractive index of air (1.00027 for the whole C-band), along with core and cladding radii of 4.1 and 62.5 μm, respectively. A TFBG with a tilt angle of 10°, length of 1 cm, and period near 557 nm was written in this fiber using standard UV photosensitivity (KrF laser irradiation at 248 nm through a phase mask, with hydrogen loading to enhance the photosensitivity). As reported by Zhou *et al.* [60], a calibration process must be used to correct the fiber and grating parameters to accurately model the transmission spectrum because the inscription process changes the optical properties of the fiber (the formation of an absorption band in the near-UV following the laser irradiation changes the refractive index dispersion of the core [184]) and of the grating (a slight tension is used both in the grating inscription process and in the grating holding tool used during measurements). The calibration process can determine the fiber core index to at least 10^{-5} accuracy and the dispersion to 5%. A large number of TFBG calibrations have shown that for the FBG fabrication conditions listed above, the average core index of the irradiated SMF-28 at 1610 nm increases to values in the vicinity of 1.4497, i.e. an increase of ~5 $\times 10^{-3}$ from the value of the pristine fiber core. What is more important in the context of using many resonances distributed over a 100 nm spectral window, the core index dispersion increases from 1.2×10^{-5} to values in the vicinity of 1.8×10^{-5} nm^{-1} (a very significant increase of 50%). Without such adjustment, simulated grating resonances deviate from measured ones by hundreds of picometers (this calibration process can be made automatically by iterative use of a mode solver and TFBG simulation tool). Figure 22(a) shows the best fit obtained between the simulated and measured data, whereas Fig. 22(b) shows the individual resonance wavelength errors between the simulation

Figure 22
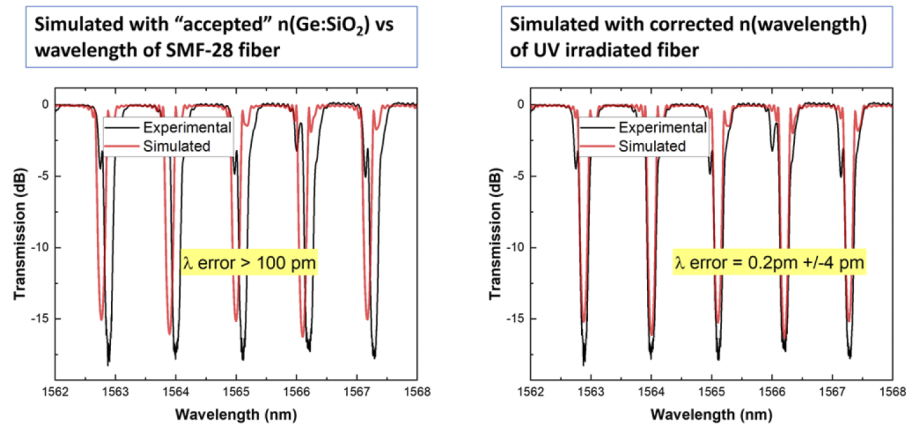
(a) Simulated and measured TFBG spectrum with simulation parameters from the accepted model for the Ge doping level of the SMF-28 fiber core. The Bragg wavelengths coincide, and the average core index has been adjusted by the increase due to the grating inscription. (b) New simulation with core index dispersion adjusted to line up the resonances to those of the measured spectrum.

and measurement. The average error has been reduced to less than 1 pm with a standard deviation of 4 pm.

Taking as a starting point the parameters of the calibrated TFBG in air, it is now possible to calculate predicted wavelength shifts of all the resonances under a given perturbation, such as changing the temperature, strain, surrounding medium, or adding a layer of material. Figure 23(a) shows a typical case of simulated wavelength shifts of the resonances of a calibrated TFBG caused by SRI increases from a starting point in a surrounding medium made of pure water. It is clear that the sensitivity increases with cladding mode order, as expected from the increase in evanescent field penetration. In contrast, Fig. 23(b) shows corresponding simulations for strain applied to a TFBG, where the sensitivity decreases with increasing cladding mode order. These examples show that differential measurements between several modes can be used to improve the measurement accuracy and help identify the sources of unknown perturbations.

Figure 23
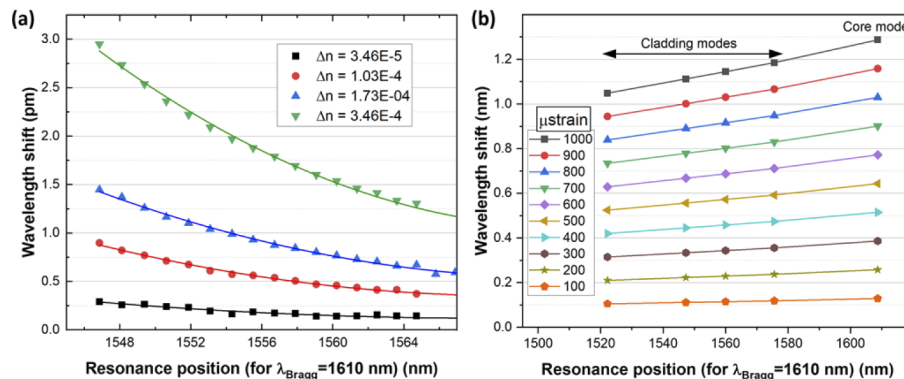
Simulated wavelength shifts of the resonances of a 10° TFBG with a Bragg wavelength at 1610 nm (a) exposed to increasing surrounding refractive index from a starting point in pure water and (b) axially pulled from 0 to 1000 μstrain.

Figure 24
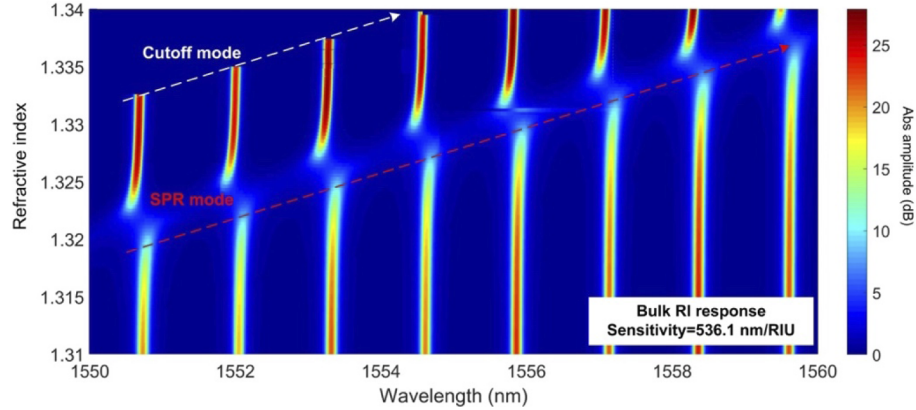
Simulated spectrum evolution of a TFBG with a Bragg wavelength at 1562 nm, surrounded by media with increasing refractive index.

A similar approach can be taken for plasmonic-assisted sensors, by adding a layer of metal to a calibrated grating in the simulations and calculating wavelength shifts for the given sensing modality [70,183–187]. Figure 24 shows how the simulated spectrum of a gold-coated TFBG in liquid varies with the refractive index of the liquid.

Given that full-scale simulations of fiber gratings are very computationally intensive (a full-spectrum calculation at 10-pm resolution takes several hours on a personal computer), other tools are available to calculate grating wavelength shifts from simpler starting points. Because of the long history of FBG sensors and their extensive use in real applications, the sensitivities of mode effective indices to strain and temperature have been studied and characterized extensively. In the case of gratings, the "rules of thumb," 10 pm/°C and 1 pm/μstrain, have been found to be useful and convenient approximations [166]. However, these depend on the wavelength of the Bragg resonance and slightly more accurate estimates can be found using "gauge factors" in the form of $\Delta\lambda/\lambda$ (where λ is the wavelength of a resonance). In those terms, the temperature and strain gauge factors for SMFs have been found to be 6.25×10^{-6}/°C and 0.8×10^{-6}/μstrain, respectively, for wavelengths in the near-infrared [188]. Still, more exhaustive characterizations or empirical calibrations are often carried out in applications where the highest possible accuracies are required, and the cost of such additional work justified.

Sensitivity calculations. The wavelength shift sensitivity of a guided mode resonance at wavelength l due to a grating of period Λ and under a perturbation "x" can be summarized in the following expression for the corresponding gauge factor K_x:

$$K_x = \frac{1}{\lambda}\frac{d\lambda}{dx} = \frac{\frac{\partial}{\partial x}(N_1 + N_2) + (N_1 + N_2)\frac{1}{\Lambda}\frac{d\Lambda}{dx}}{(N_{g1} + N_{g2})}, \tag{17}$$

where N_{gi} is the group index of the guided modes being coupled (see Supplement 1 for details).

Measurement and peak finding methodologies. The determination of the exact position of grating resonances is an important factor in increasing the accuracy of resonant fiber sensors, and gratings, in particular. Even for FBGs and their contra-directional variants that benefit from a high Q factor, there are some challenges. For "simple" uniform gratings, and assuming that the sensing modality does not lead to a chirp of the grating period or refractive index along the grating, it is possible to obtain sub-picometer wavelength position accuracy even using spectrometer with spectral resolutions of the

Figure 25
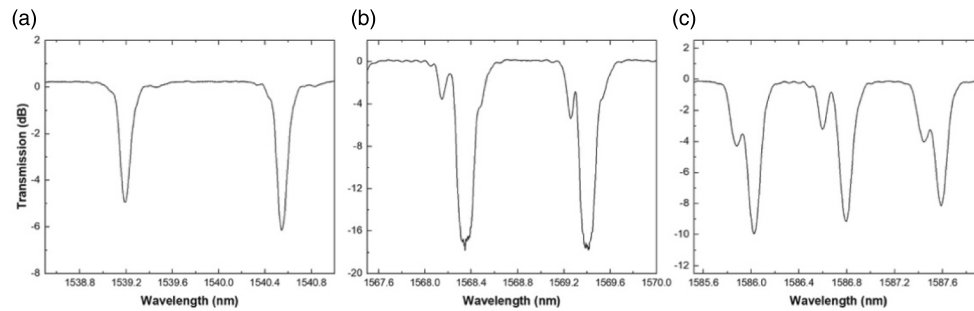
Enlarged view of several individual resonances of a TFBG, showing shape changes, shoulders, double peaks, and so on.

order of 100 pm [189]. This is obviously significantly more difficult for gratings with wider linewidth resonances (LPGs, Ex-TFBGs) or when measurements are carried out with lower spectral resolution. In order to achieve such precision, peak fitting algorithms have been developed for the most common FBGs [190–196], based on model function fits, centroid calculation or Hilbert transform approaches. Of course, these techniques remain available for FBGs in multicore systems, as long as the cores are single mode. For multimode systems, and especially those where nearly degenerate modes combined into each grating resonance, the resonance shapes can be slightly asymmetric and variable across the spectrum. For instance, Fig. 25 shows some of the individual resonances of a 1-cm long, 10° tilt TFBG across its transmission spectrum: in this case, it is obvious from this that conventional peak fitting algorithms must be adjusted according to the distance from the Bragg wavelength to account for the shape changes.

These issues are sometimes avoided by the use of pre-calibrated wavelength sweeping detection systems [197], or spectral "envelope" detection methods where individual resonance amplitude and wavelength fluctuations are averaged out [198–202]. When the measured transfer function of a sensor device in its initial (or rest) state can be simulated with a certain measurable accuracy, any change in the device state due to a "sensing event" can be traced back quantitatively to the cause of the change by varying those changes in the model until it fits the new measured state of the device. As an example, an accurate model of a specific resonance of a gold/palladium-coated TFBG was used in Ref. [185] to determine how the permittivity of the palladium changed upon exposure to hydrogen gas. All that is required is to change the permittivity in the model until the simulated resonance corresponds to that of the measurement.

Multiparameter sensing from multiple resonances. Despite the peak fitting challenges, multimode systems offer important advantages in multiparameter sensing. The availability of multiple independent measurable variables in a fiber response means that more than one parameter can be measured, or that one parameter be measured with greater accuracy by averaging the response calculated from each measured variable. Mathematically, the impact of M kinds of perturbations on a system with N measurable variables (where $M < N$) can be expressed as follows (using three parameters, temperature T, SRI, and strain (ε), and five resonances (λi) for instance. The parameters of the matrix (i.e., K_{ij}) are the individual gauge factors of each mode resonance and they can either be determined empirically or from reliable simulations and theoretical

considerations:

$$
b = \begin{bmatrix} \Delta\lambda_1/\lambda_1 \\ \Delta\lambda_2/\lambda_2 \\ \Delta\lambda_3/\lambda_3 \\ \Delta\lambda_4/\lambda_4 \\ \Delta\lambda_5/\lambda_5 \\ \Delta\lambda_6/\lambda_6 \end{bmatrix} = \begin{bmatrix} K_{11} & K_{12} & K_{13} \\ K_{21} & K_{22} & K_{23} \\ K_{31} & K_{32} & K_{33} \\ K_{41} & K_{42} & K_{43} \\ K_{51} & K_{52} & K_{53} \\ K_{61} & K_{62} & K_{63} \end{bmatrix} \begin{bmatrix} \Delta T \\ \Delta\text{SRI} \\ \Delta\varepsilon \end{bmatrix} = Kx. \tag{18}
$$

This is an "overdetermined" linear system of equations (more measurements than parameters to find), so once the gauge matrix K is known, the inverse problem of finding the best values of ΔT, ΔSRI and $\Delta\varepsilon$ (in the least squares sense) from the $\Delta\lambda_i$ can be solved (using the function "mldivide" in MATLAB© for instance, identified by the operator "\" below):

$$
\begin{bmatrix} \Delta T \\ \Delta\text{SRI} \\ \Delta\varepsilon \end{bmatrix} = K\backslash \begin{bmatrix} \Delta\lambda_1/\lambda_1 \\ \Delta\lambda_2/\lambda_2 \\ \Delta\lambda_3/\lambda_3 \\ \Delta\lambda_4/\lambda_4 \\ \Delta\lambda_5/\lambda_5 \\ \Delta\lambda_6/\lambda_6 \end{bmatrix}. \tag{19}
$$

The right-hand side of the operation shown in Eq. (19) is functionally similar to multiplying the column vector of measured wavelength shifts by the pseudo-inverse (also called the "Moore–Penrose generalized inverse") of K ("pinv" in MATLAB). The two approaches provide a different "best" solution to the problem within the roundoff error of the calculation. In principle, the precision of the result should increase with the number of measurements (i.e., wavelength shifts), a result which has not been proven yet in fiber sensors. In the minimum case, i.e., equal numbers of measurement, the solution of the inverse problem only exists if the determinant of matrix K is non-zero, because the solution is then given by

$$
\begin{bmatrix} \Delta T \\ \Delta\text{SRI} \\ \Delta\varepsilon \end{bmatrix} = K^{-1} \begin{bmatrix} \Delta\lambda_1 \\ \Delta\lambda_2 \\ \Delta\lambda_3 \end{bmatrix} = \frac{\text{adj}(K)}{\det(K)} \begin{bmatrix} \Delta\lambda_1 \\ \Delta\lambda_2 \\ \Delta\lambda_3 \end{bmatrix}. \tag{20}
$$

Given this form, any error in the measurement of $\Delta\lambda$ will lead to increasingly large errors in the parameters to be measured for smaller values of the determinant of M. Several examples of this can be found in the literature, but rarely with more than two parameters [6,24,35,47,203–206].

In addition to measuring several parameters at the same time, the availability of multiple measurements for a given sensing event provides the possibility of removing crosstalk from unwanted variables. This is particularly important for removing the effect of "intrinsic" sensitivities (temperature, fiber strain and curvature) from the target sensing application. In the case of wavelength-based SRI measurements with a strain-free sensor for instance, parasitic temperature variations affect the values of the measured wavelengths, but they also change the refractive indices of the fiber and surrounding media through thermo-optic effects. In such case, the separate measurement tells the user at which temperature the refractive index was measured. This is routinely done with TFBGs where the core mode resonance is inherently insensitive to changes occurring solely outside the core mode field cross section, as long as the group index contribution is taken into account in the measurements of the other resonances [14,207–210].

3. RECENT ADVANCES IN SENSING APPLICATIONS

3.1. Temperature

Although temperature sensing is already very well addressed by SMF sensor technologies, it is discussed here for two reasons: applications at higher temperatures than those of common FBG technologies and dealing with the cross-sensitivity to temperature of multimodal sensors for other applications. In the case of modal interferometers, the wavelength shift of a fringe maximum at λ_m due to a change in temperature ΔT is given by

$$\Delta \lambda_m = \left(\alpha + \frac{1}{\Delta N} \frac{\partial \Delta N}{\partial T} \right) \lambda_m \cdot \Delta T, \tag{21}$$

where α is the thermal expansion coefficient of the fiber and ΔN the difference in effective indices of the interfering modes.

In Fig. 26, we show the interference patterns observed at different temperatures in a packaged SMF–MCF structure fabricated with 2.54 cm of the MCF shown in Fig. 10(a). In this case, the cleaved end of the MCF was used as a reflector. It can be noted that at high temperatures the shift is nonlinear. The sensitivity in the 700–1000°C range was found to be approximately 33 pm/°C, which is around 300% more sensitive than an FBG, which cannot operate at high temperatures.

On the gratings side, FBGs and arrays of FBGs in SMFs have been used for temperature sensing for decades. From the point of view of multimodal sensing, what changes is that each mode resonance will shift slightly differently according to its temperature gauge factor derived from Eq. (16) as

$$K_T = \frac{1}{\lambda} \frac{d\lambda}{dT} = \frac{\frac{\partial}{\partial T}(N_1 + N_2) + (N_1 + N_2)\frac{1}{\Lambda}\frac{d\Lambda}{dT}}{(N_{g1} + N_{g2})}. \tag{22}$$

Therefore, more accurate temperature values can be obtained from simultaneous measurements of the slightly different wavelength shifts of multiple resonances. This property allows to produce dual temperature and strain sensors [206]. Recent advances in the development of grating-assisted temperature sensors include high-temperature measurements, beyond the value (most probably around 850°C according to the previous reports) at which silica turns into cristobalite, weakening the fiber.

Figure 26
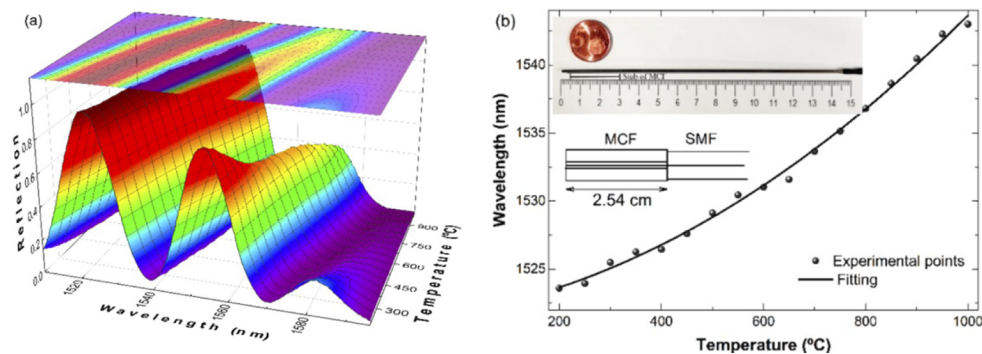
(a) Normalized reflection spectra observed at different temperatures in a packaged SMF-MCF structure. (b) Calibration curve; the peak centered at around 1522 nm was correlated with temperature. The inset photograph shows the packaged sensor after its exposure to 1000°C; the sketch of the sensor structure is also shown. The length of the seven-core MCF was 2.54 cm. Adapted from [132].

Sensing up to 1050°C or even slightly more has been achieved with femtosecond laser-induced FBGs [211,212]. Very recently, similar conclusions have been observed for TFBGs [213].

3.2. Strain and Shape

3.2a. Axial Strain

In the case of axial strain, multimodal point sensors can be used to increase the measurement accuracies or decrease cross-sensitivity in applications where more conventional fiber sensors do not suffice.

If a modal interferometer is subjected to an axial tension, its length increases and this gives rise to a phase shift difference between the interfering modes. For an axial tension σ (the applied force per unit area of the fiber), the change in length of an interferometer of length L, will be $\Delta L = \sigma L / Y$ (where Y is Young's modulus of the fiber). Furthermore, the refractive indices of the device will change due to the photo-elastic effect. For the simplest case of a SMF under tension, the following equation can be used for the change in the refractive index of each material making up the fiber [214]:

$$\frac{\partial n}{\partial \sigma} = -\frac{1}{2Y} n^3 [p_{12} - \nu(p_{11} + p_{12})], \tag{23}$$

where n is the refractive index of the core, ν is the Poisson ratio of the fiber, and p_{11} and p_{12} are the appropriate components of the strain-optic tensor.

The shift of the interference pattern can be estimated in a similar manner as previously. By differentiating Eq. (20) with respect to L and by assuming a constant temperature, we obtain

$$\Delta \lambda_m = \left(1 + \frac{L}{\Delta N}\frac{\partial \Delta N}{\partial L}\right)\lambda_m \cdot \varepsilon. \tag{24}$$

In this expression, the strain $\varepsilon = \Delta L / L$. Equation (24) suggests that the shift of the interference pattern is linear with the applied strain to the device (assuming that the photo-elastic contribution implicit in the $\partial \Delta N / \partial L$ term is small enough to be in its linear range). The main issue of modal interferometers when they are used for strain sensing is their cross-sensitivity to temperature. Thus, it is important to compensate for the effect of temperature to measure strain, pressure, or force with high accuracy, which is often done with an additional modal interferometer isolated from strain, pressure, or force used as a reference.

Supermode interferometers have been employed for sensing strain in real-world environments. It was demonstrated that such devices can provide information as accurate as a commercial Bragg grating strain sensor [215]. The advantage of modal interferometers is their capacity to operate at high temperatures, up to 1000°C, because they can be made of all silica fibers.

In the case of grating resonances, because $(1/\Lambda)(\partial \Lambda / \partial \varepsilon) = 1$ the gauge factor for axial strain is equal to

$$K_\varepsilon = \frac{1}{\lambda}\frac{d\lambda}{d\varepsilon} = \frac{\frac{\partial(N_1 + N_2)}{\partial\varepsilon} + (N_1 + N_2)}{(N_{g1} + N_{g2})} \tag{25}$$

and, as for temperature, each guided mode shifts by a slightly different amount under strain [216]. As the K_ε and K_T of the modes are different, a single measurement of the shifts of a group of cladding modes can, in principle, be used to differentiate strain and temperature with a single multimodal grating.

3.2b. Shape (3D Strain, Curvature)

Fiber-optic curvature sensors have several potential applications; probably the most attractive is shape sensing, which, in turn, has applications in the industry and biomedical sectors [45,50,211,217]. An ideal curvature sensor must provide the amplitude and the direction of curvature, and this is where multimodal sensors become ideal, as in [44,218].

Mechanically, an optical fiber can be treated as a homogeneous circular rod. If the fiber is subjected to curvature, its refractive-index profile will change due to the stress experienced by the fiber materials. The changes of the index profile alter the shape of the modes that are excited in the curved fiber. In the particular case of bending, a good approximate formula for the change in refractive index of the materials making up the fiber is given by

$$n'(x, y) = n(x, y) \left(1 + \frac{x}{R_{eff}} \right), \tag{26}$$

where $n'(x,y)$ and $n(x,y)$ are the refractive index profiles of the bent and straight fiber, respectively, x is the radial distance from the center of the fiber in the plane of bending, y the orthogonal direction to x in the fiber cross section (with z along the fiber axis). Here R_{eff} is a function of the photo-elastic tensor coefficients (p_{11} and p_{12}) and Poisson ratio ν of the fiber [219]:

$$R_{eff} = \frac{R}{1 - \frac{n(x,y)^2}{2}(p_{12} - \nu(p_{11} + p_{12}))}. \tag{27}$$

The above equation indicates that the index of the core and cladding will increase or decrease gradually and non-uniformly with respect to a straight fiber, depending on the direction of the curvature. As different modes occupy different spaces in the fiber cross section, they experience different values of index change as they propagate, which, in turn, shifts the interference pattern and also often induces a change in its amplitude.

A second consequence of bending is a shift and deformation of mode fields [220]. Figure 27 shows the profiles of two circular modes when the MMF is straight (left-hand graphs) and when it is curved (right-hand graphs). The direction of curvature is

Figure 27
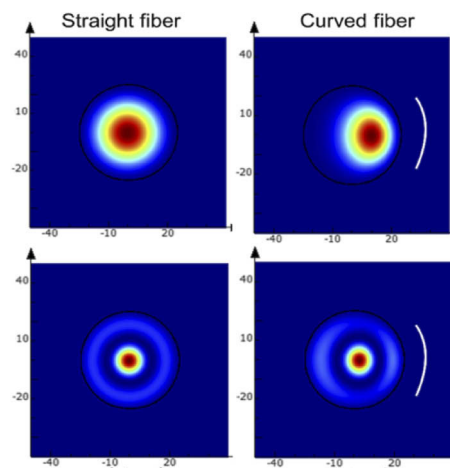
(a) Refractive index profile of a MMF when it is straight (solid line) and when the fiber is curved (dotted line). (b) Profiles of two circular modes in the MMF calculated at 1550 nm when it is straight and curved. The white lines indicate the direction of the applied curvature to the fiber. In all cases, the core of the fiber is 50 μm.

indicated with the white arcs. It can be observed that the mode shifts in the direction of curvature or to the region of the core where the refractive index is higher.

It is mostly this mode field disturbance which enables the measurement of curvature via gratings, for the following reasons. As seen from Eq. (26), for pure bending the index change at the center of the fiber is zero. This minimizes the effect of bending on mode effective indices and, therefore, on resonance wavelength shifts. On the other hand, the coupling coefficients between a core mode and cladding-guided modes depend on their overlap integral, and whereas the core mode (nearest to the fiber axis) shifts very little, cladding mode fields extend much further and shift significantly. These shifts produce amplitude changes of the grating resonances instead of wavelength shifts. In all cases, if the optical fiber is symmetric, these approaches measure the magnitude of bending only, not its direction [51]. To identify the direction of the curvature, an asymmetry in the segment that supports the interfering modes is necessary [26,133]. Likewise for gratings, the same curvature will lead to large differential resonance amplitude changes that are direction-specific only for gratings that break the symmetry (i.e., TFBGs, Ex-TFGs, and localized FBGs) [221–223].

As a particular case of curvature or strain sensing, the measurement of vibrations with high sensitivity and precision is important in a wide variety of sectors (structural health monitoring, ground motion monitoring, and condition monitoring). In the conventional way to detect vibrations with an optical fiber sensor, usually a seismic mass is coupled to the optical fiber. Vibrations move periodically the mass and the optical fiber experiences cyclic strain or displacements. The disadvantages of this approach include bulky sensors and risks of breaking the optical fiber when the sensor is in resonance. If a modal interferometer is used to detect vibrations, no mass is needed. The periodic bending, strain, or curvature of the multimode segment of the interferometer gives rise to cyclic phase shifts, which periodically shifts the interference pattern [48,134,224,225]. Some modal interferometers are so highly sensitive to curvature or bending that small-amplitude vibrations can be detected at frequencies approaching 100 MHz [224–227].

Finally, a recent example of the use of MCF gratings for 3D shape sensing is shown in Fig. 28 [50]. The fiber is interrogated by optical frequency domain reflectometry which provides the value of the local Bragg wavelength as a function of distance along each fiber, which then can be analyzed to provide the local curvature and strain over the full fiber length [114].

3.3. SRI Sensing and Related Sensing Modalities

The excitation and control of evanescent fields propagating outside the cross section of fibers opens up a myriad of sensing opportunities, from simple bulk refractometry to applications in chemistry, materials characterization, thin-film deposition monitoring, electro-chemistry, biochemistry, and medical devices. In the following, we describe how cladding mode measurements by resonant or interferometric processes can be used for each kind of sensing application and review some of the most recent advances.

3.3a. Bulk Refractometry

The simplest extrinsic sensing modality consists of exposing the evanescent fields of fiber modes to a change in refractive index in the surrounding medium, i.e., the depth over which the evanescent part of each mode extends, which, in turn, depends on the mode. In fiber-optic refractometers, the link between the refractive index to be measured and device output is the mode effective index, and how it depends on the SRI. Regardless of the sensing configuration used (resonant or interferometric), the $\partial N_i / \partial n_{SRI}$ factor of a given cladding guided mode depends on the power fraction

Figure 28
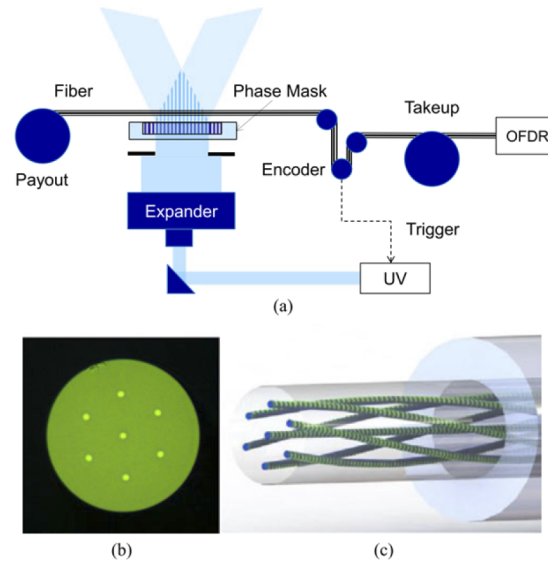
(a) System for the inscription of a continuous Bragg grating in all the cores of a seven-core fiber. (b) Photograph of the cross section of the fiber. (c) Diagram showing that the fiber is twisted along its axis. Reprinted with permission from [50]. Copyright 2017 Optical Society of America.

of the mode that is located in the surrounding medium: higher-order modes (less confined) will be modified more strongly than others and have their optical path lengths or resonant wavelengths (for interferometers and gratings, respectively) vary more than that of other modes (Fig. 23). This is, for instance, why the sensitivity of fiber refractometers is sometimes increased by reducing fiber diameters to bring modes closer to cut-off and to extend their evanescent fields further in the medium to be sensed.

Although both interferometric and resonant SRI sensors can measure refractive index variations with very high accuracy, only the latter can perform an "absolute" refractive index measurement, i.e., provide a refractive index value without a reference measurement. This was first demonstrated for TFBGs, based on a measurement of the wavelength of the last guided cladding mode resonance. Much like an Abbe refractometer, the effective index of this last guided mode (which is related to its resonance wavelength by Eq. (15)) is nearly equal to the SRI because it corresponds to the end of the total internal reflection of light by the cladding. It is in such cases beneficial to have the highest possible spectral density of modes (i.e., using TFBGs or localized FBGs instead of LPGs or Ex-TFGs, and a large diameter of the guiding structure relative to the wavelength) to reduce the uncertainty arising from the wavelength separation between resonances [56,178]. Figure 29 demonstrates this sensing modality for saline solutions.

Of course, it is only needed to measure refractive index shifts in many other applications instead of an absolute value, and generally over very limited ranges. In such cases, as in biosensing for instance, it is then more advantageous to track the wavelength shifts and/or amplitude changes of the modes near cut-off, as proposed in [186]. Although the cut-off modes reach their maximum sensitivity, of the order of 10–20 nm per refractive index unit (RIU) over a very limited range [78], their resonance wavelength can be measured with picometric accuracy, giving a limit of detection of the order of 10^{-4} for that sensing methodology. Of course, TFBGs and localized FBGs also provide

Figure 29
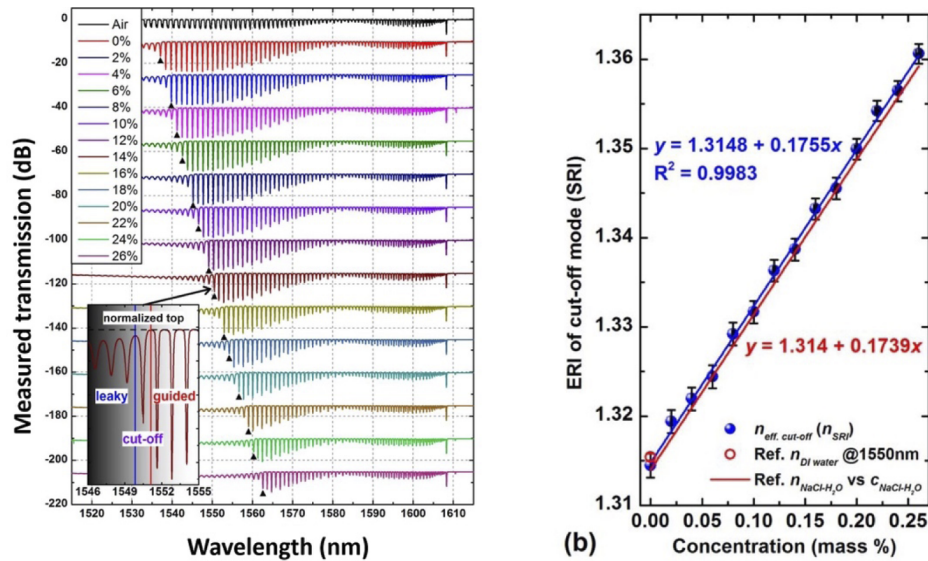
(a) Measured TFBG spectra following immersions in liquids with increasing SRI (as indicated by the salt concentrations of the water solutions in the legend). The inset shows the details of a spectrum near the cut-off point where the mode effective index is equal to the SRI. (b) SRI determined from the cut-off mode effective index as a function of salt concentration in water, with reference data for the index of saline solutions from the literature. Reprinted with permission from [179]. Copyright 2015 Optical Society of America.

the inherent advantages of a simultaneous measurement of the *in situ* temperature, from the Bragg wavelength measurement, and of uncertainty reduction techniques by combining multiple resonance shifts in the data processing algorithms.

Although these features are interesting, there are many applications where higher accuracies are required. These can be achieved using plasmonic amplification of the modal sensitivities: for both TFBGs and localized FBGs, it is possible to selectively excite TM polarized cladding modes at the fiber surface and to couple energy to surface plasmons in noble metal layers deposited on the fiber surface. As such, for a metal thickness ranging between ~30 and ~70 nm and upon the use of P-polarized light, a strong modulation of the cladding mode resonance spectrum for cladding mode resonances phase-matched to the surface plasmon. The hybridized plasmonic cladding modes have as much as 70% of their power density located in the surrounding medium at the peak of the surface plasmon phase matching resonance and as a result this resonance condition becomes highly sensitive to the SRI. In the case of gold-coated TFBGs in water with a Bragg wavelength near 1610 nm, the plasmonic resonances occur near 1543 nm (whereas the cut-off mode occurs at 1537 nm, for the same fiber without gold layer; see Fig. 30), and the location of the surface plasmon shifts by 550 nm/RIU (about 50 times more than the most-sensitive cladding mode resonance near cut-off). However, the SPR is relatively broad and poorly resolved (by the comb of cladding mode resonances in the spectrum). As shown in the application examples provided in later sections, it is often preferable and much more accurate to infer the SPR shift due to SRI changes from the individual wavelength shifts and amplitude changes of the mode resonances located just before and after the maximum of the SPR (where the resonances are almost completely attenuated).

Figure 30
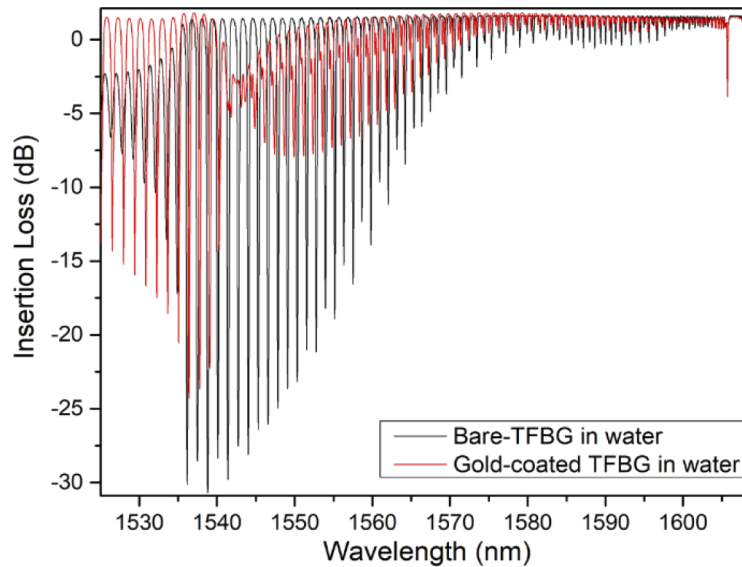
Comparison between the transmitted amplitude spectra of a bare and gold-coated 8° TFBGs in pure water. The cut-off wavelength occurs near 1536 nm in the bare spectrum, whereas the SPR resonance is observed near 1542 nm in the gold-coated spectrum. The cut-off is much less evident for the gold-coated TFBG due to partial shielding by the gold.

An interesting variant of bulk refractometry is the use of fiber gratings to detect liquid level changes. It has been known for a while that the response of a partially immersed, relatively long fiber grating refractometer shows a transmission spectrum that has features corresponding to the two media which surround the grating, in proportions corresponding to the fraction of the grating length in each medium [228]. This idea was recently extended to dynamic measurements of the motion of a fluid boundary along the grating to determine the flow velocity and direction [229,230]. The same principle was used in the measurement of the surface tension of liquids in the milli-Newton range but in this case for partial contact of a water bead around the circumference of the fiber grating [231]. In all cases, the required information is obtained from differential amplitude and wavelength shifts of selected resonances in the transmission spectrum of TFBGs and partially gold-coated TFBGs.

3.3b. Thin-Film Characterization and Modifications

A closely related problem to bulk SRI measurement, but in many ways more important, is the addition or modification of a thin layer of material on the fiber outer surface. This is the situation in most instances of chemical and biochemical sensing, where a "functional" layer is needed to provide selectivity of the sensor to a particular substance or reaction. As those layers are typically extremely thin (most often monolayers of the order of a few nanometers in thickness), the approximate perturbation methods described in Section 2.2 could, in principle, be used to calculate the effect of functional layers and their modifications on mode fields and, thus, to simulate and analyze sensing events. However, the optical properties of the nanoscale layers used in most cases are not known accurately (especially for organic molecules exposed to liquid buffers) and any error in the actual thickness of the layer changes the mode field overlap by the largest amount (the rate of exponential decay of mode fields is largest at the cladding surface). As the accuracy needed in chemical experiments is typically very high, these uncertainties make simulations of functional layer sensors extremely

Figure 31
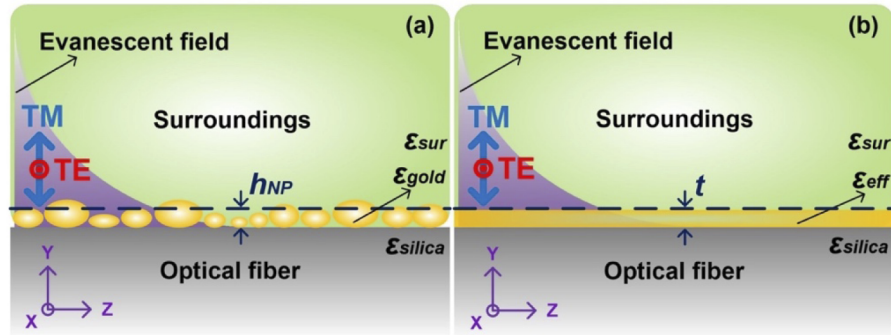
(a) Discontinuous coatings on a fiber and (b) their equivalent layer model. The possible polarizations of the probing light electrical field are also indicated. Reprinted with permission from [72]. Copyright 2014 Optical Society of America.

challenging, if not impossible. Therefore, these kinds of sensors are typically characterized experimentally on a case-by-case basis, which may explain their lack of broad acceptability outside of research settings.

These issues are complicated further when the functional layers are discontinuous. In these cases, even the definition of a layer thickness is problematic, and the average complex permittivity of the layer also depends on the properties of the surrounding medium (and what happens to it during experiments). The general problem for measuring with discontinuous nanoscale coatings is sketched in Fig. 31.

In conventional (free space and bulk material) optics, effective medium theories, such as the Maxwell–Garnett and Bruggeman formulas, have long been used to predict the optical properties of mixtures of different materials, including metals and dielectrics [73,232]. Although some attempts have been made to use these approaches in guided geometries, their use in the case of deeply subwavelength thicknesses over multi-wavelength interaction lengths has not been very convincing so far [71,72].

Another factor that is only occurring in discontinuous coatings is the possibility of mode loss which is not associated with absorption, but rather scattering [233,234]. Although both these sources of loss lead to mode attenuation and its effect on grating resonances (amplitude and width) or interferometer fringe visibility, their effect on the real part of the mode effective index dispersion differ: absorption changes are related to refractive index changes through Kramers–Kroenig relations, but scattering losses are not. As modal sensitivies are strongly affected by mode dispersion, it remains an unsolved challenge to deal with the scattering versus absorption issue in simulating fiber sensor properties of discontinuous nano- and micro-scale coatings and binding events on fibers. Figure 32 shows how the scattering out of a gold-nanoparticle-coated TFBG depends strongly on the polarization state of the cladding mode evanescent field, leading to an apparent differential loss in the transmission spectrum.

Nevertheless, polarization and selective excitation of cladding modes enable very precise measurements of the optical properties of thin films. This is especially critical for metallic and near-metallic films at near-infrared wavelengths. It has been found that ultrathin continuous and discontinuous metal coatings have a major effect on the amplitudes and wavelengths of polarized cladding mode resonances in TFBGs. By comparing measured changes with simulated models, the properties of several kinds of thin metal coatings have been determined in the last few years [181,235,236].
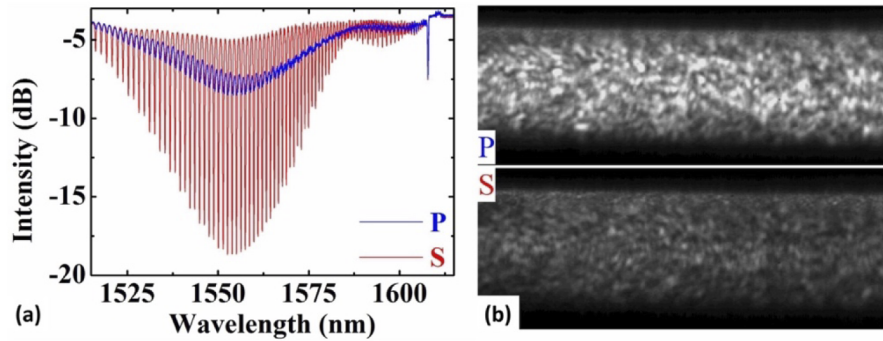
Polarization-resolved cladding mode scattering from gold-nanoparticle-coated fiber. Reprinted with permission from [72]. Copyright 2014 Optical Society of America. The larger scattering occurs for P-polarized input light, and the corresponding transmission spectrum shows much higher resonance loss.

This application of multimodal fiber sensors constitutes one of the most promising directions for developing a new class of *in situ*, real-time monitoring tools for coating systems, including widely used coating processes such as chemical vapor deposition (CVD), magnetron sputtering (MS), pulsed vapor deposition (PVD), thermal evaporation, atomic layer deposition (ALD), chemical binding, and crystallization.

Furthermore, it has been recently shown that optical fiber sensors can be used to measure the linear electrical properties of metals [70] as well as their electro-chemical [237] and nonlinear optical properties [182]. To this aim, optical fiber devices have been used in a wide variety of configurations to deliver extremely sensitive and accurate thin-film properties and growth data. Table 1 provides a sample of relevant references and their main features.

For a recent example, Ref. [251] shows how a very uniform nanoscale ITO coating increases the modal birefringence between S and P resonances of a TFBG in the mode transition regime (ITO thicknesses near 250 nm), where the sensitivity of the resonances to perturbations (twist in this case) is magnified (Fig. 33). Measuring the TFBG during deposition will allow the desired thickness to be achieved precisely regardless of variations in deposition rates or differences between the thickness on fiber with that obtained from external thickness monitors.

3.4. Electromagnetic Sensors Based on Surface Refractometry

Although most optical fiber materials do not have a second-order optical nonlinearity, it is possible to build fiber electric field sensors by surface refractometry with the help of electro-optic coatings. The most frequent examples of this have been liquid crystal coatings (or infiltrations into the holes of microstructured fibers), but those are limited to static or relatively low-frequency measurements [252–254]. Recent developments in the accuracy and sensitivity of fiber-based refractometers open up new possibilities using solid electro-optic coatings at frequencies limited only by the speed of the fiber interrogation systems (at least tens of gigahertz for single wavelength/photodetector detection systems) using laser light tuned on the edge of a transmission resonance, as in [186]. Similarly, fiber-optic refractometers can detect the presence or displacements of magnetic particles around the fiber surface or of changes in magneto-optic coatings (Table 2).

Although fiber-optic magnetic field sensors based on Faraday rotation of the mode polarization have been around for a long time, this is relatively weak effect and it

requires special fiber materials with a large Verdet constant as well as long interaction lengths. Much stronger response, including magnetic field orientation determination (as well as magnitude) was demonstrated using fiber gratings immersed in magnetic fluids (a stable colloid suspension of magnetic Fe_3O_4 nanoparticles). In the presence of a magnetic field, the nanoparticles accumulate asymmetrically around the fiber circumference according to the orientation and strength of the magnetic field. This accumulation changes the local refractive index (and loss) of the material around the fiber, a change that can be detected easily with evanescent field fiber sensors, especially when polarized light is used along with plasmonic enhancement thanks to a thin gold film on the TFBG, as depicted in Fig. 34.

3.5. Electrochemical Plasmonics in Renewable Energy

In the context of the global transition towards renewable energies, the need for new monitoring tools to ensure safety and optimum operation of storage and power sources has emerged [272]. Due to the outstanding importance of this recent application and the fact that fiber optics is often the only way to make certain kinds of measurements, it is treated here separately and includes pioneering work using SMF optic sensor designs. Progress in this direction was first demonstrated in 2013 [273], with further developments using the wavelength dependence of FBG sensors on the local temperature (T), pressure (P), and strain (ε) [274–277]. In particular, FBG sensors embedded within a battery were used to image the temperature distribution [278,279] and to provide state of charge (SoC) and state of health (SoH) estimations [280–282]. Similar

Table 1. Selected Examples of Fiber-Based Configuration of *in situ* Monitoring Deposition Process

Optical Fiber Configuration	Reactant	Substrate	Coating Material	Deposition Method	Interrogation Wavelength (nm)	Ref.
TFBG	Au nanoparticles and HAuCl4	SiO_2 (fiber)	Au	Electroless plating	1520–1570	[238]
TFBG	$[Au(NMe_2(N^iPr)_2]_2$ /$[Au(Me2^tBu-^ip)]_2$	SiO_2 (fiber)	Au	CVD	1520–1610	[236,239, 240]
TFBG	Au source	SiO_2 (fiber)	Au	Electron beam	1566–1568	[79]
TFBG	$[Cu(NMe_2(N^iPr)_2]_2$	SiO_2 (fiber)	Cu	p-CVD	1520–1600	[241]
TFBG	Ag Source	SiO_2 (fiber)	Ag	Thermal evaporation/etching	1530–1620	[70]
TFBG	AgNO3, Ethylene glycol and poly (vinyl pyrrolidone)	Ag-SiO_2 (fiber)	Ag nanowire	Covalent binding	1520–1600	[235,242]
TFBG	O_2-plasma, Zn source	SiO_2 (fiber)	ZnO	Sputtered	1540–1580	[243]
TFBG	Cysteamine, AuNP colloid	SiO_2 (fiber)	Biotin-Avidin	Protein binding	1525–1625	[244]
TFBG	Trimethyl aluminum, H_2O	SiO_2 (fiber)	Al_2O_3	ALD	1529–1575	[245]
Au-coated TFBG	Au source, 1-Dodecanethiol (DDT)	SiO_2 (fiber)	Au and DDT	Thermal evaporation and Covalent binding	1552–1576	[187]
Au-coated TFBG	Au source, Pb^{2+} ions	SiO_2 (fiber)	Au and Pb compound	Electrochemical	1547–1548	[246]
LPG	$Al(CH_3)_3$, H_2O	SiO_2 (fiber)	Al_2O_3	MS and ALD	1200–1600	[247]
Ag and Fe–C-coated LPG	NaCl	Ag, Fe-C and SiO_2 (fiber)	Ag and Fe-C	Electroplated	1550–1620	[248 249–250]
ITO-coated TFBG	ITO film, air	SiO_2 (fiber)	ITO	Sputtering	1550–1620	[251]

Figure 33
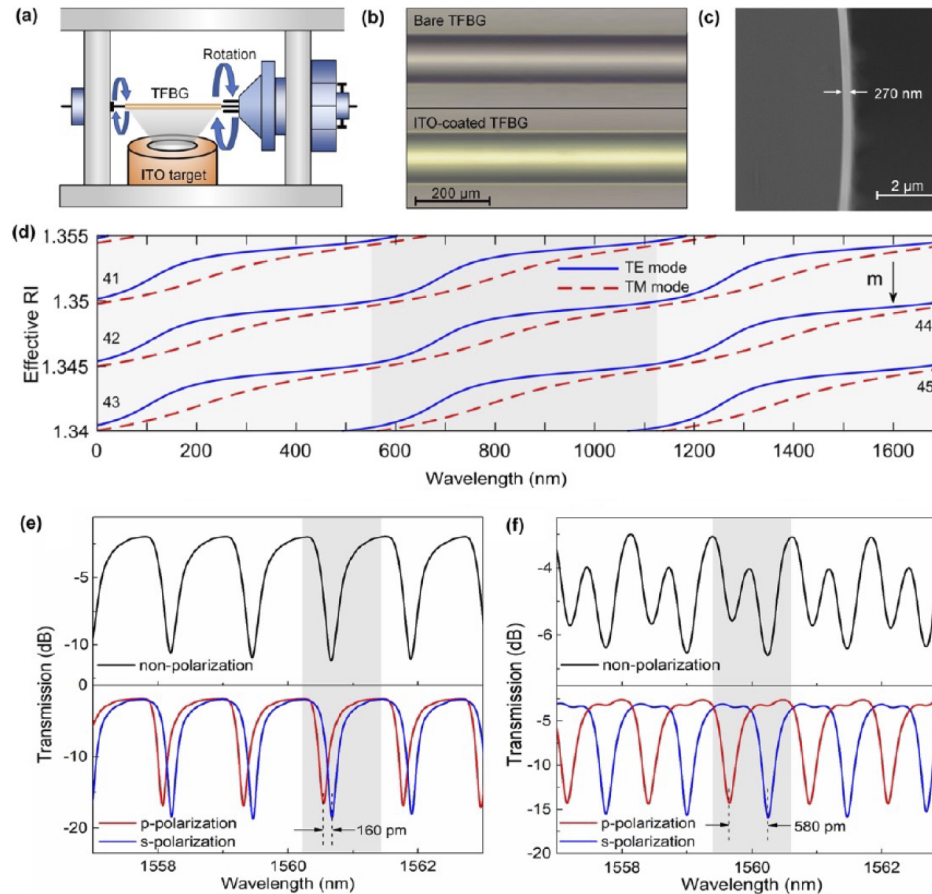
(a) Rotated magnetron sputtering technique. (b) Microscopic images of the bare TFBG and ITO-coated TFBG. (c) SEM image of the fiber cross-section with ITO coating. (d) Calculated effective mode indices for HE/TE and EH/TM modes as a function of ITO thickness, showing mode transitions (accelerated mode dispersions) occurring at different thicknesses. (e) Experimental spectra measured with unpolarized input (black), P-polarized input (red) and S-polarized input (blue) for (e) bare TFBG and (f) ITO-coated TFBG. Reproduced with permission from [251]. Copyright 2021 Optical Society of America.

sensors were developed to decouple the effect of thermal and strain on Li-ion batteries [283,284]. First attempts at *in situ* chemical parameter identification of electrolytes for the optimization of Li-ion batteries were carried out by Raman spectroscopy with a multifiber probe for measurements of ion concentrations close to the electrode surface [285]. More recently, similar studies were performed in commercial Na(Li)-ion cells with specially configured FBGs in microstructured fibers [286]. Figure 35 shows some of the features of this system and the correlations between the fiber sensor data and the electrical measurements.

Finally, plasmon-assisted fiber sensors such as TFBG-SPR devices are ideally suited to detect electrical processes and charging states within batteries and supercapacitors used in energy storage because their properties depend strongly on the distributions of charges along the metal-coated surfaces. Placing a metal-coated fiber sensor in proximity to an electrode should respond to the state of the electrode and to the local concentration of electrolytes. The first demonstrations of such sensing performance were published in 2018 and showed simultaneous optical and electrochemical

Table 2.   Selected Examples of Fiber-Based Electromagnetic Field Sensors

Configuration (Vector (Y/N))	Coating	Sensing Field	Range	Sensitivity	Wavelength (nm)	Ref.
LPG + D-shaped fiber	Magnetic fluid	Magnetic	1.4–191.2 mT	176.4 pm/mT	1520–1570	[255]
Microstructured LPG	Magnetic fluid	Magnetic	0–300 Oe	1.946 nm/Oe	~967.56	[256]
TFBG-SPR (Yes)	Au film and Magnetic fluid	Magnetic	0–18 mT	2 nm/° 1.8 nm/mT	1520–1560	[257]
TFBG (Yes)	Magnetic fluid	Magnetic	0–28 mT	0.038 dB/rad 0.39 dB/mT	1522–1524	[258 259–260]
TFBG	Liquid Crystal	Electric field	1.0–4.8 kV/cm	0.287 dB/ kV/cm	1520–1550	[261]
MZ-interferometer (Yes)	Magnetic fluid	Magnetic	0–238.2 Oe	−170 pm/Oe −0.21268 dB/Oe	1440–1640	[262 263 264–265]
Sagnac Interferometer	Magnetic fluid	Magnetic	0–1000 Oe	1.17 nm/Oe	~1160	[265]
Multimode interference	Magnetic fluid	Magnetic	0–500 Oe	- 0.01939dB/Oe	1150–1350	[266]
Taper Interferometer (Yes)	Magnetic fluid	Magnetic	38–250 Oe	56 pm/Oe 0.13056 dB/Oe	1520–1610	[267,268]
Fabry–Pérot Interferometer	Magnetic fluid	Magnetic	0–400 Gs	0.0431 nm/Gs	1530–1565	[269]
Few-Mode-Fiber-Based Plasmonic (Yes)	Au film and Magnetic fluid	Magnetic	0–400 Oe	0.692 nm/Oe- 11.917 nm/°	550–850	[270]
Side-Polished MMF (Yes)	Magnetic fluid	Magnetic	0–300 Oe	−0.053 nm/ Oe−5.68 nm/°	1450–1610	[271]

measurements of a supercapacitor under charge–discharge cycles, as shown in Fig. 36 [287].

3.6. Chemical/Biochemical/Medical Advances

Biochemical sensors have known cutting-edge improvements in the recent years, both in terms of technology, miniaturization, versatility, response time, and sensitivity. Optical fiber biosensors are part of the game and have undergone multidisciplinary progress in both biochemical sciences and photonics engineering. As grating-assisted optical fibers are highly resolute refractometers, they possess intrinsic properties that make them suited to detect molecular events happening on their surface. [157,288]

In that philosophy, bare modal sensors such as TFBGs or LPFGs and their etched versions, FBGs and etched-FBGs, ex-TFGs, made in silica or polymer fibers can be functionalized with biochemical receptors through different ways (Fig. 37). Indeed, the immobilization of receptors on glass and polymeric materials has been the subject of an abundant literature, especially for the functionalization of chips and site-directed anchoring. [289,290] Reliable biochemical immobilization processes therefore exist through covalent or non-covalent bindings. While covalent bindings present higher stability, passive adsorption on surfaces remains highly exploited in biochemical assays such as for enzyme-linked immunosorbent assay (ELISA) microtiter plates and leads to sufficient binding forces to operate in successive solutions and samples. [291] Surface treatment such as plasma [292,293], chemical modifications [294], or UV–O_3 exposure coupled with deep surface drying are often needed to ensure sufficient molecular adhesion for physical adsorption [295]. More than passive layers, optical fiber biosensors are able to directly self-monitor

Figure 34
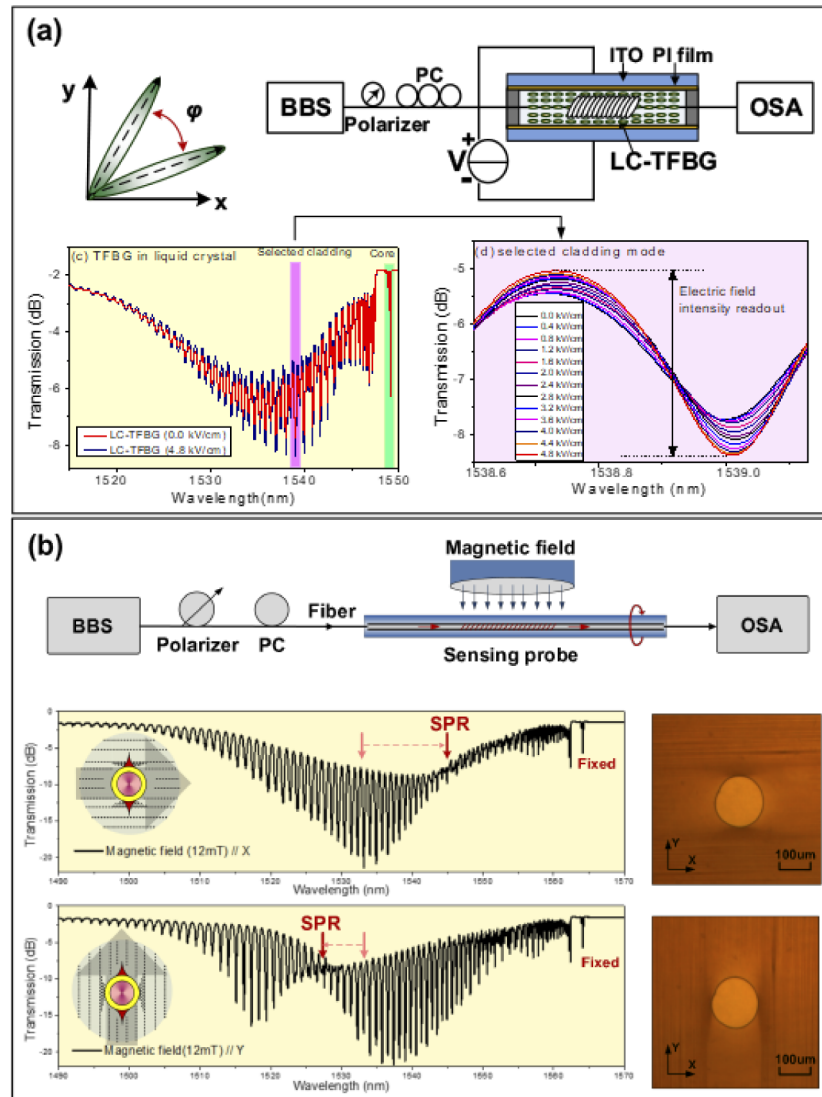
(a) Liquid-crystal-assisted TFBG electric measurement. Reprinted with permission from [261]. Copyright 2017 Optical Society of America. (b) Magnetic-fluid-assisted TFBG-SPR magnetic fields measurement. Reprinted from [257]) under a Creative Commons 4.0 license .

the binding of receptors in real time, where other devices have to rely on the efficiency of a chemical process and further perform quality tests, after receptors immobilization.

The molecular building blocks to manufacture grating-assisted optical fiber biochemical sensors differ, depending on the target application. Receptors such as antibodies, DNA or RNA, aptamers, affimers, proteins, enzymes, molecularly imprinted polymers (MIPs) are only few examples within the numerous categories of bioreceptors and biomimicking receptors developed nowadays. Antibodies remain a safe bet with a large commercial availability when DNA probes show higher stability and versatility. Both antibodies and DNA-based molecules therefore remain gold standards in biosensors [296,297].

Figure 35
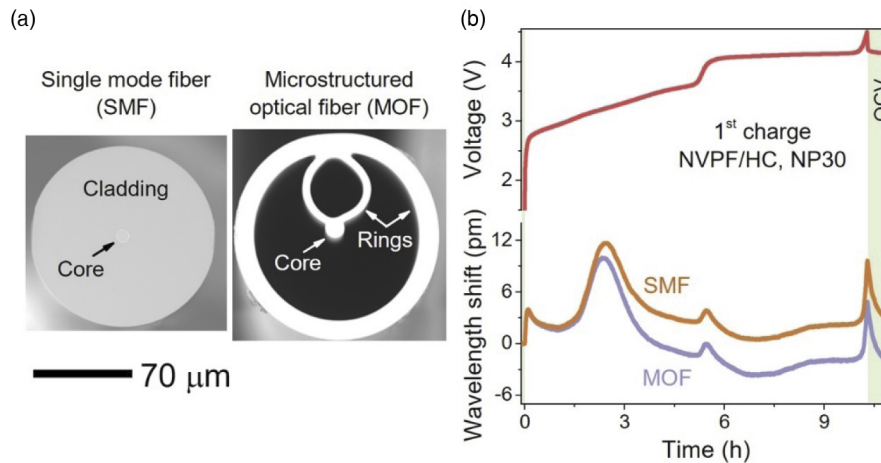
Fiber-based measurements of electrical parameters in Na(Li)-ion battery. (a) Two types of fiber used; (b) simultaneous voltage and FBG wavelength shifts in the two types of fiber. Reprinted by permission from Macmillan Publishers Ltd: Huang *et al.*, Nature Energy **5**, 674–683 (2020) [286]. Copyright 2020.

The use of antibodies on bare gratings has been investigated through covalent binding and non-covalent binding via direct adsorption. Other strategies such as the use of intermediate proteins as the so-called "protein A," which binds to the constant region of IgG antibodies, have also been investigated to better orient antibodies on their surface. It appears that covalent binding of antibodies on glass can be performed through silanization using (3-aminopropyl)trimethoxysilanes (APTMS). Silanization is often performed to ensure a strong anchoring layer that can further bind to many types of chemical groups, as many substitutes exist [298,299]. Silanized optical fibers can, for instance, be coupled with antibodies using glutaraldehyde to create covalent bonds. On the other hand, electrostatic adsorption can be applied on silanized surfaces by adding receptors directly after that surface pre-modification. Last, but not least, protein A intermediates can be added to the process through these two procedures as well [300]. They, however, need additional steps and increase the distance between receptors and the optical fiber surface, whereas closer events are detected with higher impacts. These three aforementioned immobilization techniques have all demonstrated fine detection features on bare gratings [301] and can still be adapted and optimized according to the nature of the optical fibers and the experimental conditions.

DNA receptors can also be attached on glass thanks to crosslinkers or silanization processes. The main advantage of such synthetic molecules is their ability self-bind according to the orientation of their binding site, so the efficiency of the receptors layer is better assured. Spacers can easily be added chemically to reduce steric hindrance and boost the binding performance of the anchored bioreceptors. [302] On the other hand, MIPs are not considered as biomolecules but as bio-mimicking components. These receptors have also been investigated through covalent binding on bare fiber surfaces and are increasingly being studied. They are mostly produced through the synthesis of reticulated polymers in the presence of templates made of targets (ions, macromolecules, cells, etc.). A vinylization of silica is often needed to ensure a strong binding of the MIPs while non-imprinted polymers (NIPs) are used as references. MIPs demonstrate an increasing interest for gas sensing, as they are able to catch molecules flowing onto the sensor's surface [303].

Figure 36
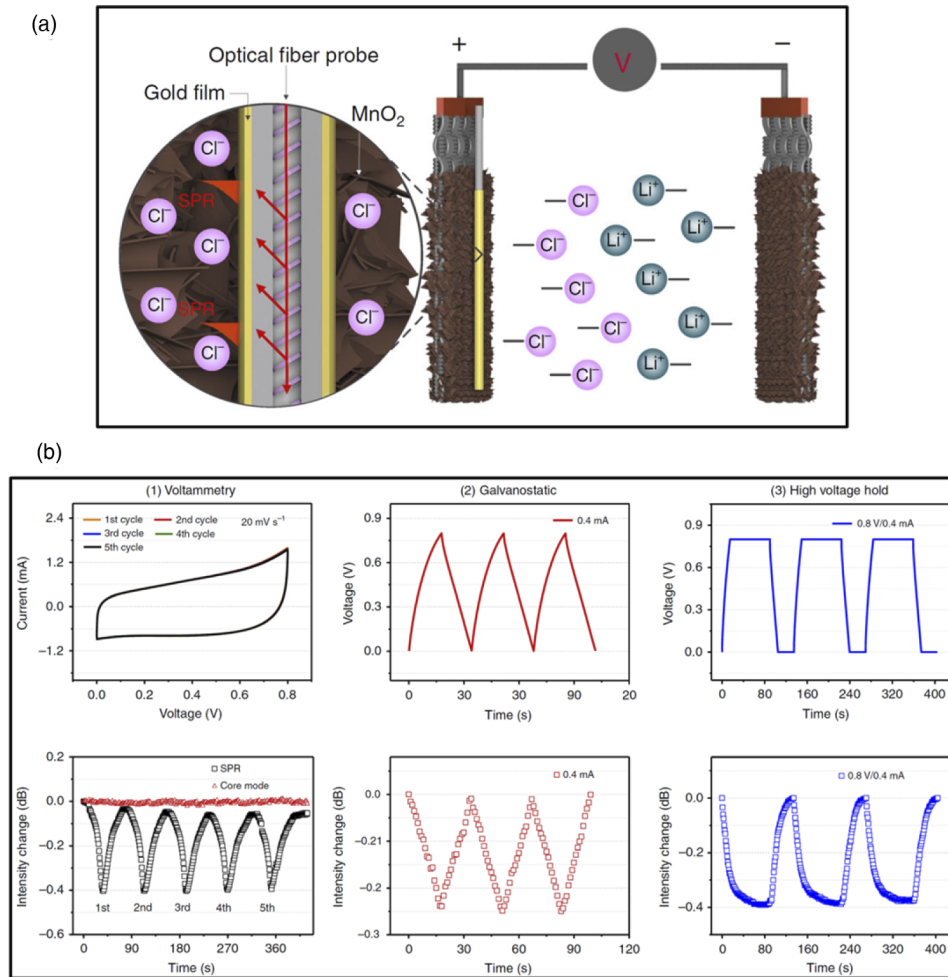
(a) TFBG-SPR measurement of the state of charge of a supercapacitor. (b) Representative electrical measurements (top) and corresponding response of the most sensitive TFBG resonance (bottom). Reprinted from [285] under a Creative Commons 4.0 license.

It is also important to mention that bare optical fiber configurations do not only rely on a direct use of the grating structure in its original integrity, but sometimes need a surface etching to expose the grating to the outer medium and enhance its sensitivity

Figure 37
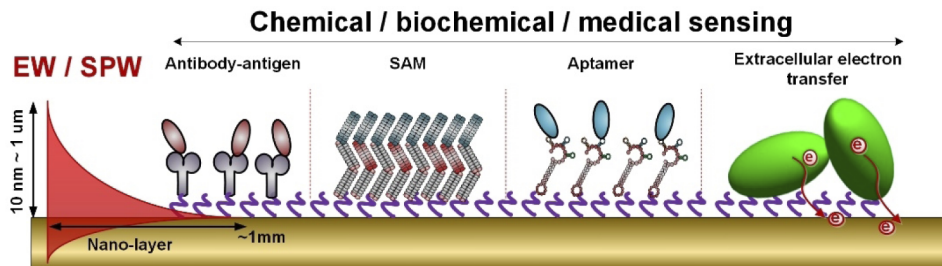
Several possibilities for surface functionalization. Reprinted from [287] under a Creative Commons 4.0 license .

Table 3.   Representative Non-Plasmonic Optical Fiber Grating Sensors: Non-Exhaustive List Since 2014

Optical Fiber Configuration and Detection method	Receptor / Target	Bulk Refractive Index Sensitivity (nm/RIU)	Limit of Detection (LOD)	Ref.
TFBG	Molecularly imprinted polymer (MIP) / Maltol	NA	~ 1-10 ng/mL	[303]
TFBG	Antibody / Cytokeratin 17	~20 nm/RIU	14 pM	[298]
Etched-TFBG	Aptamer / thrombin	23.4 nm/RIU	75-110 pM	[305]
Etched-FBG	Aptamer / Thrombin	17.4 nm/RIU	10 nM	[306]
LPFG	Aptamer / cocain	6000 nm/RIU	20 μM	[307]
Etched-LPFG	Antibody / T7 phage (virus)	4300 nm/RIU	5×10^3 PFU/mL	[304]
Etched-LPFG	Graphene oxide - antibody / C-reactive protein	670–1035 nm/RIU	0.15 ng/mL	[145]
LPFG	Lipase enzyme / triacylglycerides	N.A.	177.1 mg/L	[308]
LPFG	Polycarbonate - Graphene oxide - Streptavidin / Biotinylated BSA	~2000nm/RIU	< 0.2 aM	[309]
LPFG	Polycarbonate – Cryptophane A / methane	~3560 nm/RIU	0.2% (v/v)	[310]
LPFG	DNA/DNA wine variety	N.A.	62 nM	[311]
Ex-TFG	Glucose Oxidase / Glucose	1168 nm/RIU	0.013-0.02 mg/mL	[312]

[304]. Using this strategy, structures such as LPFGs or TFBGs can improve bulk refractive index sensitivities and reach very high values, making them intriguing for biochemical detections, as reported in Table 3. Non-plasmonic fibers can therefore only rely on their intrinsic sensitivities which explains why intermediate steps such as etching procedures are sometimes mandatory. Surface amplifications may therefore also be necessary to enable the detection of very low target concentrations. This is often achieved by adding nanoparticles or nanostructures that play the role of hotspots on the surface and locally enhance local refractive index changes in relation with the target detection.

Although these bare-grating approaches have led to significant advances, most optical fiber biosensors are relying on sensitivity amplification by SPR or localized surface plasmon resonance (LSPR) effects. [313] These sensors are exploiting the similarity of the TFBG-SPR approach to the Kretschmann prism principle used in many commercial biochemical affinity sensors but with the addition of the grating to generate high-Q-factor resonances to help quantify small wavelength shifts and to provide a local temperature reference. This is in contrast with the abundant literature on claddless MMF SPR sensors [314,315] which do not use individual modes of the fiber to measure fine changes, and which are not discussed here.

Different metal layers or particles can be selected to improve plasmonic properties and many bioconjugation strategies can therefore be applied, depending on the selected configuration. Gold (Au) is the most suitable noble material to reach high stability and sensitivity, but the use of other materials such as silver [316], platinum [317], palladium [318], copper [319], or tungsten also exist [320]. Hybrid phenomena using both continuous metal layers and nanoparticles or nanoparticle clusters have been studied in recent years. [321] The quality and uniformity of the metal layer deposited on the cylindrical surface of optical fibers is of paramount importance, and clearly plays a role in the reproducibility and sensitivity to biodetections. The generation of nano-islands and thermal influences on nanometric metal films have been recently

explored to identify their effects on the film adhesion and its related surface sensitivity [322,323].

Continuous metal films are only one part among the many possible uses for plasmonics. Indeed, localized effects can be generated and amplified using dedicated nanostructures. Among these effects, the use of nanodots, nanorods and nanowires, nanospheres, nanocages, or other specific particles shapes are commonly used in the development of molecular sensors [237]. The local effects provoked by these edifices on the optical signal cause modifications which affect both the surface refractive index and the molecular construction. For example, gold nanoparticles can be coated with bioreceptors and then bind to targets already immobilized on the optical fiber surface. This results in a local refractive index change but also in the formation of strong molecular bonds, which consequently generate a permanent and cumulative effect on the surface as long as stable conditions are maintained [324]. Other configurations rely on biochemical detections to bring nanoparticles closer to the surface or to move them further to play on localized hotspots [325]. This diversity is an infinite resource for combining technologies and precisely adjusting the capacities of each configuration, according to specific needs linked to experimental conditions (temperature, pH, nature of targets and receptors, surface roughness, etc.).

Bioreceptors are varied and can all be biochemically combined with metallized surfaces. DNA receptors and antibodies are often covalently bound to metal surfaces thanks to the formation of self-assembled monolayers (SAMs) and chemical crosslinkers can be selected to tune the anchoring of the receptors. For instance, DNA strands or aptamers sequences can be modified to possess thiol ends and directly bind on gold or silver after a reduction process. Furthermore, classical functionalization with antibodies often relies on carbodiimide crosslinking, through NHS/EDC (N-hydroxysuccinimide and carbodiimide). Carboxyl-reactive chemical groups bind to primary amines and provoke the anchoring of bioreceptors on the surface. Both chemistries have been studied on metal-coated gratings for the detection of proteins and cells and have shown limits of detection comparable with those obtained with laboratory techniques such as the ELISA. The monitoring of small refractive index shifts on the sensor's surfaces allow a label-free detection, which means that no enzymatic or fluorescent labeling is necessary. Blocking agents such as bovine serum albumin (BSA), casein, fish gelatin, and others, need to be handled and well balanced to ensure high surface selectivity, while maintaining sufficient target binding. This ratio between available bioreceptors and sufficient blocking drives the whole performance of the system, while establishing the rate of false-positive or false-negative detections.

The number of biosensors based on metal-coated gratings is increasing and there is a real interest in many applications (environmental sensing, *in vivo* measurements, rapid diagnostic tests, etc.). In recent years, high performance has been reported for metal-coated gratings (Table 4) and many strategies have been highlighted as alternatives to more traditional biosensors.

This table points out a very large range of limits of detection, from femtomolar to micromolar levels. It is important to mention that most works dealing with optical fiber biosensors and more generally with optical devices are calibrated through bulk refractive index measurements (sucrose or glucose, lithium chloride solutions, oils, etc.). These calibrations are useful to roughly determine bulk sensitivities, but it turns out that it does not necessarily reflect the same level of performance for surface sensing, especially when the range of the evaluated solutions are not in the same range of buffers used for biosensing. Devices with approximately same reported refractive index sensitivities finally end up with very disparate sensitivities to target surfaces. This can be explained by the various affinities between receptors and targets, efficiency of surface

**Table 4.   Representative Coated Optical Fiber Grating Sensors Since 2014**

Optical Fiber Configuration and Detection Method	Receptor / Target	Bulk Refractive Index Sensitivity (nm/RIU)	Limit of Detection (LOD)	Ref.
Gold-coated Dual-Resonance LPFG (DR-LPFG)	Aptamer / cyanobacterial toxin	3891.5 nm/RIU	~ 5 ng/mL	[326]
LPFG with titania-silica sol-gel	Antibodies IgG / Anti-IgG	> 2000 nm/RIU	~ 10 pM	[327]
LPFG with silica core gold shell nanoparticles	biotin / Streptavidin anti-IgM /Immunoglobulin M	N.A.	0.86 pg/mm^2 and 22 pg/mm^2	[328]
Micro-tapered LPFG with graphene oxide	GO / hemoglobin	N.A.	0.02 mg/mL	[329]
LPFG coated with atactic polystyrene (aPS)	Antibody / Thyroglobuline	~ 1700 nm/RIU	0.12 pM	[330]
TFBG with Au/Graphene layers	Aptamer / Dopamine	N.A.	160 fM	[331]
Ex-TFG with graphene oxide	Glucose Oxidase / Glucose	110-127 nm/RIU	mM range	[332]
Ex-TFG with gold nanospheres	Antibody / Newcastle disease virus (NDV)	180 nm/RIU	~25 pg/mL	[333]
Gold-coated TFBG	Concanavalin A / Glucose	688 nm/RIU	0.1 pM	[334]
Gold-coated TFBG	Boronic acid derivative / Glycoprotein	576.04 nm/RIU	15.56 nM	[335]
Gold-coated TFBG	Antibody / Cytokeratin 17	N.A.	14 pM	[336]
Gold-coated TFBG	Antibody / Cytokeratin 7 peptides	N.A.	0.4 nM	[337]
Gold-coated TFBG	Biotin / Streptavidin	~500 nm/RIU	2 pM	[338]
Gold-coated TFBG	Aptamer / Thrombin	N.A.	1 nM	[339]
Gold-coated TFBG	DNA / dopamine	N.A.	0.1 pM	[331]
Gold-coated TFBG	Aptamer / HER2	102.03 nm/RIU 124.89 nm/RIU	~8.6 fM	[340]
Gold-coated TFBG	Aptamer / cells	N.A.	10–49 cells/mL	[341]
Gold-coated TFBG	Aptamer / Thrombin	N.A.	22.6 nM	[342]
Gold-coated TFBG	DNAzyme / Pb^{2+}	N.A.	8.56 pM	[325]
Gold-coated TFBG	Estrogen receptors / environmental estrogens	N.A.	~5.5 pM	[343]

bindings, experimental conditions (temperature, pH, distance between the surface and the immobilized targets, orientation of bioreceptors, etc.). All this affects reproducibility and fair comparisons between similar biosensing strategies. It is therefore needed to highlight and draw more uniform assessments for biosensing analysis in the near future to enable a better evaluation of the intrinsic performance for each approach.

3.7. Specific Gas Detection: the case of Hydrogen

The general advances in bulk and surface refractive index sensors described in previous sections of this paper are also applicable to detection in gaseous media, but as in other cases of chemical sensing, fiber devices must be conditioned to be selective to the target gas species chosen. Here the important case of hydrogen is chosen to demonstrate the use of multimodal techniques because it is one of the most studied gases for its potential use as a source of clean energy [344,345], but also because it poses serious security risks in storage and utilization [346,347]. To alleviate these concerns, reliable and inexpensive sensors are required to monitor hydrogen concentrations in and around storage tanks and fuel cells [348,349], including fiber-optic implementations that are desirable from a safety point of view as they avoid the use of electricity and are immune to chemical degradation [350–353]. Selectivity in this case is provided by chemically reactive thin film coatings used to translate hydrogen levels into measurable changes in optical signals. A favorite coating for this purpose has been palladium (Pd) metal

Figure 38
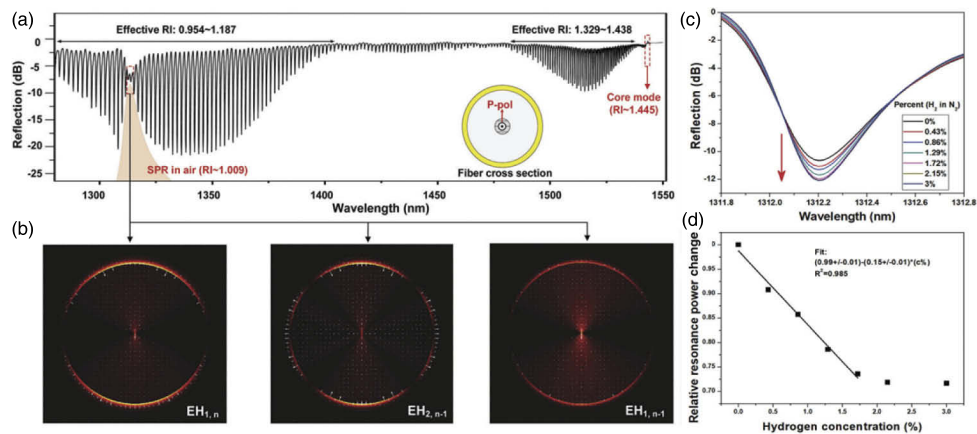
Palladium–gold alloy-coated TFBG fiber-optic sensor for _in situ_ hydrogen monitoring: (a) P-polarized transmission spectrum of the device in air; (b) mode intensity patterns in the vicinity of the SPR maximum; (c) measured changes of the most sensitive resonance with H_2 concentration in air; (d) calibration of the power level change versus H_2 concentration. Reprinted with permission from Zhang _et al._, J. Mater. Chem. C **6**, 5161−5170 (2018) [185].

as it absorbs hydrogen in proportion to its relative concentration by a combination of dissolution of H_2 molecules within the metal framework and reaction with the metal to form palladium hydride (PdH_x where x is the atomic ratio of H:Pd). Both dissolution and reaction change the average complex permittivity of the metal film by significant amounts and also its volume (i.e., thickness) in a reversible manner, detectable by the evanescent fields of suitably excited fiber modes [354–356]. As in other cases of chemical sensing, plasmonic amplification can also be used to increase the sensitivity and accuracy of fiber-based hydrogen sensors by combining hydrogen selective coatings with thin films able to support SPRs [357–359].

More recently, multiresonant approaches were developed based on extending the TFBG-SPR approach to measurements in gaseous media (i.e., media with refractive indices in the vicinity of 1.0) by using larger tilt angles near 37°. This allows the efficient excitation cladding modes with effective indices between 0.92 and 1.18 that can be phase-matched to surface plasmons at a metal–air interface [180]. This unique feature can then be used to perform accurate refractometric measurements in dilute gases and in thin films surrounded by air or other gaseous substances, in particular for hydrogen detection using palladium or palladium–gold coatings (Fig. 38) [185,360,361]. These devices have been shown to achieve faster response times (less than 20 seconds of stabilization time during association phase, and less than 30 seconds for that of dissociation phases) and improved deactivation resistance (higher than 99% per test cycle).

4. MEDICAL APPLICATIONS OF FIBER SENSORS

4.1. Cancer Biomarkers and Monitoring Living Cells

Although most biosensors are restricted to _in vitro_ usage with sampled biomaterials, such as the first demonstration of the evolution of living cells under various stimuli by gold coated TFBG-SPR sensors [362], optical fiber-based technologies can be embedded into catheters and to perform _in situ_ measurements. One of their major assets is to be able to sense on-site biomarkers and cellular environments which is a sought-after advantage to diagnose pathologies and cancers. Nowadays, most cancers can now be diagnosed by means of scans and blood tests, but some cancer or cancer subtypes

remain undetermined after these examinations and still require molecular analyses of a biopsy. One relevant example is lung cancer because it calls for invasive surgery in most cases, which require general anesthesia of the patient. Localized detection could therefore reduce the invasiveness and speed up the diagnosis. This challenge was carried out as a world premiere using gold-coated TFBGs for the detection of lung cancer biomarkers inside freshly resected human lung tissues [363]. TFBGs covered with antibodies and blocked with BSA were embedded inside a biocompatible polymer packaging allowing its insertion inside an endoscope. The flexibility of this setup was calculated to be sufficient to reach the upper lobe region, where the catheters experience an important bend. Tests were carried out on anesthetized pigs to determine whether it was possible to generate a plasmonic effect inside a living organism, while controlling the navigation of the instrument within the lungs thanks to an experienced thoracic surgeon. These first conclusive tests then led to repeated assays on a panel of patient samples, using both healthy and tumoral tissues which were further analyzed through immunohistochemistry, to validate the higher expression of cytokeratin-17 proteins (CK17) inside tumorous samples (Fig. 39). Optical fiber biosensors were then used inside dense cellular matrices and have demonstrated the feasibility of this technology. Recent works have also shown: the possibility to detect Neuropsin (Opn5) in the brain tissue of a murine model using LPFGs [364]; the use of ultrasound for tissue imaging [365]; fluorescent imaging in brain tissue [366]; the use of Raman spectroscopy using *in vivo* optical fiber applications [367]; and so on. These studies on tissues and living organisms are not a final outcome, but a first stone which paves the way towards new challenges such as multiplexing, live imaging, and tumoral cells/bacteria detection.

4.2. Theranostic Devices Combining Light Activation and Sensing

In addition to the wide deployment of photonic-based technologies in the medical and pharmaceutical disciplines, the interaction of light with living systems has been the subject of intense research for applications in diagnostic and treatment of diseases [368–370]. Multimodal fiber-optic sensors can also play a role, as they can be used to deliver light very efficiently into living organisms or in their vicinity, while simultaneously performing measurements that can be processed remotely.

For instance, the multiresonant features of a TFBG sensor with a light-absorbing coating was recently used to heat a limited region of a tissue phantom to a precise and stable temperature in the range desired for hyperthermal treatment of tumors but also to measure the local temperature in real time to avoid overheating and damaging neighboring healthy tissue. The heating was provided by an amplified near-infrared pump light signal from a tunable laser at a wavelength coupled to cladding modes whereas the temperature was measured from the wavelength shift of the Bragg wavelength using low-intensity broadband light launched simultaneously in the same fiber [371].

Another configuration of light delivery and control using a multimodal fiber sensor has been used towards the development of a point-of-care device for polymerase chain reaction (PCR) detection of viruses and DNA mutations. The same idea of generating heat from cladding-coupled near-infrared pump light and temperature measurement was used to alternatively split and recombine polymer-embedded DNA molecules spot-deposited on the fiber cladding by rapidly cycling the temperature between 40 and 80°C with a cycle time under 1 minute. This kind of device is the starting point for the development of a rapid, multiplexed PCR devices small and inexpensive enough for broad point-of-care deployment [372].

Figure 39

(a) Experimental setup with a gold-coated TFBG embedded inside an endoscope. (b), (c) Spectra inside healthy and tumoral lung tissues over 5 min. (d) Detection of CK17 molecules inside healthy and tumoral tissues of a same patient sample. Reprinted from Biosens. Bioelectron. **131**, Loyez *et al*., "*In situ* cancer diagnosis through online plasmonics," 104–112, copyright 2019, with permission from Elsevier [363].

5. REMAINING CHALLENGES AND OPPORTUNITIES

After 40 years of development and thousands of publications and patents, the only widely used applications of fiber sensors are still in temperature and strain sensing, with some advances in pressure sensing. One can argue that developments for other important applications such as (bio)chemical sensing are more recent and less mature, but what are the reasons for their limited penetration in actual field use and industrial applications? We believe that there are a number of current limitations that can be viewed as opportunities for the near future.

First, "canonical" problems in the chemical realm for which fiber-optic solutions would be ideal have not yet been clearly identified and accepted by the sensor and potential user communities. Having such targets would lead to better standardization of systems, methods, and qualification procedures to reach technology readiness levels approaching the commercialization stage. It would also spur the development of customized portable packaging and user-friendly interfaces compatible with smartphone applications and other forms of data transmission and storage. Better integrated microfluidics systems to facilitate the contact between samples and fiber surfaces are also needed and would help to standardize the way sensors are tested against different molecular targets. This would further allow the acquisition of much more experimental data and statistical validations to compare between different systems. Part of the difficulty in much of the current fiber sensors literature is the lack of sufficient methodological detail on experimental conditions and statistical measures (measurement noise quantification, limit of detection calculations, validity ranges, etc.) to ensure sufficient reproducibility and validation by the research community.

What needs to be understood and appreciated is that competing technologies (electrical sensors, in particular) are mass-produced at extremely low cost and that they use standardized, familiar interrogation units (usually for voltage or current measurements, that are also typically much less expensive than optical counterparts). Lowering the cost of optical instrumentation while maintaining the high resolution of mainframe optical tools is the key for a subsequent deployment of the technology. This will be enabled by advances in photonic lightwave circuits and optical processing, notably through the creation of the equivalent of ASICs (application-specific integrated circuits) in photonics and opto-electronics.

The vast majority of optical sensor systems developed currently rely on optical instrumentation designed for other purposes (optical telecommunications and spectroscopy, for instance) and, therefore, feature capabilities or performance levels that may not be absolutely necessary for sensors. Similarly, and specifically for chemical sensing, better control of the quality and reproducibility of functional coatings is also required. This will be achieved by optimizing the fiber-coating processes for mass production. An interesting idea here is to use some of the fibers being coated as *in situ* monitors for the batch deposition. These advances will allow the development of chemical fiber sensor stubs packaged with a connector ferrule compatible with fiber-based instruments and that would be so economical that they can be replaced after a single use (which is often a feature of chemical sensing through functional layers) and yet sturdy and reliable enough to be shipped and stored securely for extended periods of time prior to use.

In addition to these essential steps, it will also be useful to consider lowering the complexity of fiber device configurations, for instance by avoiding the use of sophisticated precision splicers when dealing with multifiber combinations or micro-machined parts of the fiber. Configurations compatible with mass production such as unclad fiber combinations or fiber gratings should be privileged. In the case of gratings, it is also essential to lower the dependence of sensor performance on exact grating parameters, which will allow mass production at low cost. Improving the numerical modeling of such configurations will help in this regard.

Finally, a great opportunity lies in the development of machine learning and artificial intelligence in optical fiber sensing. Both interferometers and grating-based sensors can be designed to generate highly complex optical spectra that contain enormous amounts of information (there are 10,000 optical power level points in a 100 nm wide spectrum at 10 pm measurement resolution), and yet very low-level peak-level fitting routines of single resonances are still most commonly used. Much of the spectral

content is therefore thrown away while meaningful parameters could certainly be obtained to make the data extraction process from the optical measurements more robust and more accurate. Progress in this direction is beginning to occur but much more needs to be done to take full advantage of optical techniques, especially in multimodal systems based on gratings [373,374] and interferometers [375].

Given the wealth of applications that can be addressed with multimodal optical fiber sensors, compared with FBG arrays and distributed acoustic sensing that have found significant commercial success in niche applications, researchers are still looking for research problems that have no competition from other sensing technology and, therefore, that would justify the necessary investments to realize the advances that were described in this paper. An example of this was the relatively rapid transition of multicore shape sensors from research labs to burgeoning commercial success in robotics, biomedical devices, and structural sensing.

6. CONCLUSION

In this paper, we have extensively discussed the physics, fabrication, and applications of multimodal optical fiber sensors. From basic interferometer to more advanced fiber grating configurations, we have highlighted their common mathematical formalism and reviewed the recent advances that they have enabled in diverse physical and (bio)chemical sensing applications. At a time where single-mode optical fiber sensors are a mature commercial technology, mode-division and spatial-division configurations considerably widen the sensing modalities while offering multiparameter sensing opportunities with a high resolution. Considering the recent rise in technology readiness level of such configurations, we look forward to a spread of practical and industrial applications, as fabrication techniques and metrological performance further improve.

DISCLOSURES

The authors declare that there are no conflicts of interest related to this article.

DATA AVAILABILITY

Data underlying the results presented in this paper are not publicly available at this time but may be obtained from the authors upon reasonable request.

SUPPLEMENTAL DOCUMENT

See Supplement 1 for supporting content.

REFERENCES

1. D. A. Krohn, T. W. MacDougal, and A. Mendez, *Fiber Optic Sensors: Fundamentals and Applications*, 4th ed. (SPIE Digital Library, 2015).
2. I. Del Villar and I. R. Matias, *Optical Fibre sensors: Fundamentals for Development of Optimized Devices* (Wiley-IEEE Press, 2020).
3. Z. He and Q. Liu, "Optical fiber distributed acoustic sensors: a review," J. Lightwave Technol. **39**, 3671–3686 (2021).
4. P. Lu, N. Lalam, M. Badar, B. Liu, B. T. Chorpening, M. P. Buric, and P. R. Ohodnicki, "Distributed optical fiber sensing: review and perspective," Appl. Phys. Rev. **6**, 041302 (2019).
5. I. Ashry, Y. Mao, A. Trichili, B. Wang, T. K. Ng, M.-S. Alouini, and B. S. Ooi, "A review of using few-mode fibers for optical sensing," IEEE Access **8**, 179592–179605 (2020).
6. S. Pevec and D. Donlagić, "Multiparameter fiber-optic sensors: a review," Opt. Eng. **58**, 072009 (2019).
7. A. Urrutia, I. Del Villar, P. Zubiate, and C. R. Zamarreño, "A comprehensive review of optical fiber refractometers: toward a standard comparative criterion," Laser Photonics Rev. **13**, 1900094 (2019).
8. C. Caucheteur, T. Guo, and J. Albert, "Review of plasmonic fiber optic bio-chemical sensors: improving the limit of detection," Anal. Bioanal. Chem. **407**, 3883–3897 (2015).
9. X. D. Wang and O. S. Wolfbeis, "Fiber-optic chemical sensors and biosensors (2015-2019)," Anal. Chem. **92**, 397–430 (2020).
10. L. Wang and S. LaRochelle, "Design of eight-mode polarization-maintaining few-mode fiber for multiple-input multiple-output-free spatial division multiplexing," Opt. Lett. **40**, 5846–5849 (2015).
11. E. S. Manuylovich, V. V. Dvoyrin, and S. K. Turitsyn, "Fast mode decomposition in few-mode fibers," Nat. Commun. **11**, 5507 (2020).
12. M. K. Annuar Zaini, Y.-S. Lee, K.-S. Lim, N. A. Mohd Nazal, M. H. Zohari, and H. Ahmad, "Axial stress profiling for few-mode fiber Bragg grating based on resonant wavelength shifts during etching process," J. Opt. Soc. Am. B **34**, 1894–1898 (2017).
13. F. Y. Chan, G. Mudhana, and P. Shum, "Comparison of bandwidth and sensitivity of long-period gratings in single-mode and few-mode fibers," Appl. Opt. **54**, 6558–6565 (2015).
14. X. Gao, T. Ning, C. Zhang, J. Xu, J. Zheng, H. Lin, J. Li, L. Pei, and H. You, "A dual-parameter fiber sensor based on few-mode fiber and fiber Bragg grating for strain and temperature sensing," Opt. Commun. **454**, 124441 (2020).
15. L. Grüner-Nielsen, N. M. Mathew, and K. Rottwitt, "Characterization of few mode fibers and devices," Opt. Fiber Technol. **52**, 101972 (2019).
16. S. A. Jacobs, "Failure of the weakly guiding approximation for few-mode fiber index profiles," J. Lightwave Technol. **37**, 5076–5082 (2019).
17. W. Jin, Y. Xu, Y. Jiang, Y. Wu, S. Yao, S. Xiao, Y. Qi, W. Ren, and S. Jian, "Strain and temperature characteristics of the LP11 mode based on a few-mode fiber Bragg grating and core-offset splicing," Laser Phys. **28**, 025103 (2018).
18. X. Liang, Y. Li, Z. Geng, and Z. Liu, "Selective transverse mode operation of a fiber laser based on few-mode FBG for rotation sensing," Opt. Express **27**, 37964–37974 (2019).

19. Z. Luo, H. Yu, Y. Zheng, Z. Zheng, Y. Li, and X. Jiang, "Selective mode excitation in a few-mode photonic crystal fiber for strain sensing with restrained temperature response," J. Lightwave Technol. **38**, 4560–4571 (2020).

20. C. Wang, C. Pan, J. Xu, Z. Yang, J. Zhao, and Z. Huang, "Analysis of misalignment, twist, and bend in few-mode fibers using spatially and spectrally resolved imaging," Opt. Fiber Technol. **56**, 102205 (2020).

21. Y. Xu, G. Ren, Y. Jiang, Y. Gao, H. Li, W. Jin, Y. Wu, Y. Shen, and S. Jian, "Bending effect characterization of individual higher-order modes in few-mode fibers," Opt. Lett. **42**, 3343–3346 (2017).

22. M. Yang, J. Yang, C. Guan, M. Wang, P. Geng, Y. Shen, J. Zhang, J. Shi, J. Yang, and L. Yuan, "Refractive index sensor based on etched eccentric core few-mode fiber dual-mode interferometer," Opt. Express **27**, 28104–28113 (2019).

23. J. Zhao, J. Xu, C. Wang, Y. Liu, and Z. Yang, "Experimental demonstration of multi-parameter sensing based on polarized interference of polarization-maintaining few-mode fibers," Opt. Express **28**, 20372–20378 (2020).

24. Y. Zhao, C. Wang, G. Yin, B. Jiang, K. Zhou, C. Mou, Y. Liu, L. Zhang, and T. Wang, "Simultaneous directional curvature and temperature sensor based on a tilted few-mode fiber Bragg grating," Appl. Opt. **57**, 1671–1678 (2018).

25. M. C. Alonso-Murias, D. Monzon-Hernandez, O. Rodriguez-Quiroz, J. E. Antonio-Lopez, A. Schulzgen, R. Amezcua-Correa, and J. Villatoro, "Long-range multicore optical fiber displacement sensor," Opt. Lett. **46**, 2224–2227 (2021).

26. J. Amorebieta, A. Ortega-Gomez, G. Durana, R. Fernandez, E. Antonio-Lopez, A. Schulzgen, J. Zubia, R. Amezcua-Correa, and J. Villatoro, "Compact omni-directional multicore fiber-based vector bending sensor," Sci. Rep. **11**, 5989 (2021).

27. B. J. Ávila, J. N. Hernández, S. M. Toxqui Rodríguez, and B. M. Rodríguez-Lara, "Symmetric supermodes in cyclic multicore fibers," OSA Continuum **2** , 515–522 (2019).

28. D. Barrera, J. Madrigal, and S. Sales, "Tilted fiber Bragg gratings in multicore optical fibers for optical sensing," Opt. Lett. **42**, 1460–1463 (2017).

29. D. Barrera, J. Madrigal, and S. Sales, "Long period gratings in multicore optical fibers for directional curvature sensor implementation," J. Lightwave Technol. **36**, 1063–1068 (2018).

30. M. Becker, A. Lorenz, T. Elsmann, I. Latka, A. Schwuchow, S. Dochow, R. Spittel, J. Kobelke, J. Bierlich, K. Schuster, M. Rothhardt, and H. Bartelt, "Single-mode multicore fibers with integrated Bragg filters," J. Lightwave Technol. **34**, 4572–4578 (2016).

31. D. Budnicki, D. Budnicki, I. Parola, Ł Szostkiewicz, K. Markiewicz, Z. Hołdyński, G. Wojcik, M. Makara, K. Poturaj, M. Kuklińska, P. Mergo, M. Napierała, and T. Nasiłowski, "All-fiber vector bending sensor based on a multicore fiber with asymmetric air-hole structure," J. Lightwave Technol. **38**, 6685–6690 (2020).

32. G. Capilla-Gonzalez, D. A. May-Arrioja, D. Lopez-Cortes, and J. R. Guzman-Sepulveda, "Stress homogenization effect in multicore fiber optic bending sensors," Appl. Opt. **56**, 2273–2279 (2017).

33. J. Cui, H. Luo, J. Lu, X. Cheng, and H. Y. Tam, "Random forest assisted vector displacement sensor based on a multicore fiber," Opt. Express **29**, 15852–15864 (2021).

34. A. Fender, W. N. MacPherson, R. R. J. Maier, J. S. Barton, D. S. George, R. I. Howden, G. W. Smith, B. J. S. Jones, S. McCulloch, X. Chen, R. Suo, L. Zhang, and I. Bennion, "Two-axis temperature-insensitive accelerometer based on multicore fiber Bragg gratings," IEEE Sens. J **8**, 1292–1298 (2008).

35. L. Gan, R. Wang, D. Liu, L. Duan, S. Liu, S. Fu, B. Li, Z. Feng, H. Wei, W. Tong, P. Shum, and M. Tang, "Spatial-division multiplexed Mach–Zehnder interferometers in heterogeneous multicore fiber for multiparameter measurement," IEEE Photonics J. **8**, 1–8 (2016).

36. T. A. Goebel, J. Nold, C. Hupel, S. Kuhn, N. Haarlammert, T. Schreiber, C. Matzdorf, T. O. Imogore, R. G. Krämer, D. Richter, A. Tünnermann, and S. Nolte, "Ultrashort pulse written fiber Bragg gratings as narrowband filters in multicore fibers," Appl. Opt. **60** , 43–51 (2021).

37. S. Guvenc Kilic, Y. Zhu, Q. Sheng, M. Naci Inci, and M. Han, "Refractometer with etched chirped fiber Bragg grating Fabry–Perot interferometer in multicore fiber," IEEE Photonics Technol. Lett. **31**, 575–578 (2019).

38. W. Hu, C. Li, S. Cheng, F. Mumtaz, C. Du, and M. Yang, "Etched multicore fiber Bragg gratings for refractive index sensing with temperature in-line compensation," OSA Continuum **3** , 1058–1067 (2020).

39. P. Li, P. Tian, C. Guan, Z. Zhu, Y. Li, J. Yang, J. Shi, and L. Yuan, "Heterogeneous double period array multicore fiber and its application in Bragg grating sensor," IEEE Sens. J. **19**, 6193–6196 (2019).

40. Y. Liu, A. Zhou, and L. Yuan, "Gelatin-coated Michelson interferometric humidity sensor based on a multicore fiber with helical structure," J. Lightwave Technol. **37**, 2452–2457 (2019).

41. J. Madrigal, D. Barrera, and S. Sales, "Refractive index and temperature sensing using inter-core crosstalk in multicore fibers," J. Lightwave Technol. **37**, 4703–4709 (2019).

42. D. A. May-Arrioja and J. R. Guzman-Sepulveda, "Highly sensitive fiber optic refractive index sensor using multicore coupled structures," J. Lightwave Technol. **35**, 2695–2701 (2017).

43. F. Mumtaz, P. Cheng, C. Li, S. Cheng, C. Du, M. Yang, Y. Dai, and W. Hu, "A design of taper-like etched multicore fiber refractive index-insensitive a temperature highly sensitive Mach-Zehnder interferometer," IEEE Sens. J. **20**, 7074–7081 (2020).

44. A. V. Newkirk, J. E. Antonio-Lopez, A. Velazquez-Benitez, J. Albert, R. Amezcua-Correa, and A. Schulzgen, "Bending sensor combining multicore fiber with a mode-selective photonic lantern," Opt. Lett. **40**, 5188–5191 (2015).

45. D. Paloschi, K. A. Bronnikov, S. Korganbayev, A. A. Wolf, A. Dostovalov, and P. Saccomandi, "3D shape sensing with multicore optical fibers: transformation matrices versus Frenet-Serret equations for real-time application," IEEE Sens. J. **21**, 4599–4609 (2021).

46. T. Sakamoto, T. Mori, M. Wada, T. Yamamoto, F. Yamamoto, and K. Nakajima, "Fiber twisting- and bending-induced adiabatic/nonadiabatic super-mode transition in coupled multicore fiber," J. Lightwave Technol. **34**, 1228–1237 (2016).

47. A. Van Newkirk, J. E. Antonio-Lopez, G. Salceda-Delgado, M. U. Piracha, R. Amezcua-Correa, and A. Schulzgen, "Multicore fiber sensors for simultaneous measurement of force and temperature," IEEE Photonics Technol. Lett. **27**, 1523–1526 (2015).

48. J. Villatoro, E. Antonio-Lopez, A. Schulzgen, and R. Amezcua-Correa, "Miniature multicore optical fiber vibration sensor," Opt. Lett. **42**, 2022–2025 (2017).

49. R. Wang, M. Tang, S. Fu, Z. Feng, W. Tong, and D. Liu, "Spatially arrayed long period gratings in multicore fiber by programmable electrical arc discharge," IEEE Photonics J. **9**, 4500310 (2017).

50. P. S. Westbrook, T. Kremp, K. S. Feder, W. Ko, E. M. Monberg, H. Wu, D. A. Simoff, T. F. Taunay, and R. M. Ortiz, "Continuous multicore optical fiber

grating arrays for distributed sensing applications," J. Lightwave Technol. **35**, 1248–1252 (2017).

51. S. Xiang, H. Xiongwei, Y. Luyun, D. Nengli, W. Jianjun, Z. Fangfang, P. Jingang, L. Haiqing, and L. Jinyan, "Helical long-period grating manufactured with a CO2 laser on multicore fiber," Opt. Express **25**, 10405–10412 (2017).

52. M. S. Yoon, S. B. Lee, and Y. G. Han, "In-line interferometer based on intermodal coupling of a multicore fiber," Opt. Express **23**, 18316–18322 (2015).

53. Z. Zhao, Z. Liu, M. Tang, S. Fu, L. Wang, N. Guo, C. Jin, H. Y. Tam, and C. Lu, "Robust in-fiber spatial interferometer using multicore fiber for vibration detection," Opt. Express **26**, 29629–29637 (2018).

54. D. Zheng, J. Madrigal, D. Barrera, S. Sales, and J. Capmany, "Microwave photonic filtering for interrogating FBG-based multicore fiber curvature sensor," IEEE Photonics Technol. Lett. **29**, 1707–1710 (2017).

55. R. Zhou, F. Chen, S. Li, R. Wang, and X. Qiao, "Three-dimensional vector accelerometer using a multicore fiber inscribed with three FBGs," J. Lightwave Technol. **39**, 3244–3250 (2021).

56. C. Tsao, *Optical Fibre Waveguide Analysis* (Oxford , 1992).

57. C.L. Chen, *Foundations for Guided-Wave Optics* (Wiley, 2007).

58. K. Okamoto, *Fundamentals of Optical Waveguides*, 2nd ed., (Academic Press , 2006).

59. A. W. Snyder and J. Love, *Optical waveguide theory* (Springer Science & Business Media , 2012).

60. W. Zhou, Y. Zhou, and J. Albert, "A true fiber optic refractometer," Laser Photonics Rev. **11**, 1600157 (2017).

61. C. Chen, P. Berini, D. Feng, S. Tanev, and V. Tzolov, "Efficient and accurate numerical analysis of multilayer planar optical waveguides in lossy anisotropic media," Opt. Express **7**, 260–272 (2000).

62. E. Anemogiannis and E. N. Glytsis, "Multilayer waveguides: efficient numerical analysis of general structures," J. Lightwave Technol. **10**, 1344–1351 (1992).

63. A. V. Lavrinenko, J. Laegsgaard, N. Gregersen, F. Schmidt, and T. Søndergaard, *Numerical Methods in Photonics* (CRC Press, 2017).

64. F. L. Teixeira and W. C. Chew, "PML-FDTD in cylindrical and spherical grids," IEEE Microw. and Guided Waves Lett. **7** , 285–287 (1997).

65. Y.-C. Lu, L. Yang, W.-P. Huang, and S.-S. Jian, "Improved full-vector finite-difference complex mode solver for optical waveguides of circular symmetry," J. Lightwave Technol. **26**(13), 1868–1876 (2008).

66. Z. Zhu and T. G. Brown, "Full-vectorial finite-difference analysis of microstructured optical fibers," Opt. Express **10**, 853–864 (2002).

67. J. D. Joannopoulos, S. G. Johnson, J. N. Winn, and R. D. Meade, *Photonic Crystals: Molding the Flow of Light*, 2nd ed., Chap. 9 (Princeton U. Press, 2008) ISBN:9780691124568

68. I. Del Villar, F. J. Arregui, C. R. Zamarreño, J. M. Corres, C. Bariain, J. Goicoechea, C. Elosua, M. Hernaez, P. J. Rivero, A. B. Socorro, A. Urrutia, P. Sanchez, P. Zubiate, D. Lopez, N. De Acha, J. Ascorbe, and I. R. Matias, "Optical sensors based on lossy-mode resonances," Sens. Actuators, B **240**, 174–185 (2017).

69. Z. Li and H. Zhu, "Fiber-optic surface waveguide modes excited by inter/intra mode transition for refractometric sensitivity enhancement," IEEE J. Sel. Top. Quantum Electron. **27**, 5600308 (2021).

70. F. Liu, X. Zhang, T. Guo, and J. Albert, "Optical detection of the percolation threshold of nanoscale silver coatings with optical fiber gratings," APL Photonics **5**, 076101 (2020).

71. W. Zhou, D. J. Mandia, M. B. E. Griffiths, S. T. Barry, and J. Albert, "Effective permittivity of ultrathin chemical vapor deposited gold films on optical fibers at infrared wavelengths," J. Phys. Chem. C **118**, 670–678 (2014).

72. W. Zhou, D. J. Mandia, S. T. Barry, and J. Albert, "Anisotropic effective permittivity of an ultrathin gold coating on optical fiber in air, water and saline solutions," Opt. Express **22**, 31665–31676 (2014).

73. U. Kreibig and M. Vollmer, *Optical Properties of Metal clusters*, Vol. 25 of Springer Series in Materials Science (Springer, 1995)

74. J. U. Thomas, N. Jovanovic, R. G. Becker, G. D. Marshall, M. J. Withford, A. Tünnermann, S. Nolte, and M. J. Steel, "Cladding mode coupling in highly localized fiber Bragg gratings: modal properties and transmission spectra," Opt. Express **19** , 325–341 (2011).

75. J. U. Thomas, N. Jovanovic, R. G. Krämer, G. D. Marshall, S. Nolte, and M. J. Steel, "Cladding mode coupling in highly localized fiber Bragg gratings II: complete vectorial analysis," Opt. Express **20** , 21434–21449 (2012).

76. F. Shen and T. Zhang, "Numerical analyses of the polarization dependent cladding mode coupling in localized fiber Bragg gratings," IEEE Access **9**, 6689–6695 (2021).

77. Z. Yan, H. Wang, C. Wang, Z. Sun, G. Yin, K. Zhou, Y. Wang, W. Zhao, and L. Zhang, "Theoretical and experimental analysis of excessively tilted fiber gratings," Opt. Express **24**, 12107–12115 (2016).

78. J. Albert, L.-Y. Shao, and C. Caucheteur, "Tilted fiber Bragg grating sensors," Laser Photonics Rev. **7**, 83–108 (2013).

79. M. Z. Alam and J. Albert, "Selective excitation of radially and azimuthally polarized optical fiber cladding modes," J. Lightwave Technol. **31**, 3167–3175 (2013).

80. J. Bucaro and E. Carome, "Single fiber interferometric acoustic sensor," Appl. Opt. **17**, 330–331 (1978).

81. B. Y. Kim, J. N. Blake, S.-Y. Huang, and H. J. Shaw, "Use of highly elliptical core fibers for two-mode fiber devices," Opt. Lett. **12**, 729–731 (1987).

82. G. Salceda-Delgado, D. Monzon-Hernandez, A. Martinez-Rios, G. A. Cardenas-Sevilla, and J. Villatoro, "Optical microfiber mode interferometer for temperature-independent refractometric sensing," Opt. Lett. **37**, 1974–1976 (2012).

83. H. Luo, Q. Sun, X. Li, Z. Yan, Y. Li, D. Liu, and L. Zhang, "Refractive index sensitivity characteristics near the dispersion turning point of the multi-mode microfiber-based Mach-Zehnder interferometer," Opt. Lett. **40**, 5042–5045 (2015).

84. I. Hernández-Romano, D. Monzón-Hernández, C. Moreno-Hernández, D. Moreno-Hernandez, and J. Villatoro, "Highly sensitive temperature sensor based on a polymer-coated microfiber interferometer," IEEE Photonics Techn. Lett. **27**, 2591–2594 (2015).

85. M. Arjmand, H. Saghafifar, M. Alijanianzadeh, and M. Soltanolkotabi, "A sensitive tapered-fiber optic biosensor for the label-free detection of organophosphate pesticides," Sens. Actuators B **249**, 523–532 (2017).

86. A. D. D. Le, J. Hwang, M. Yusuf, K. H. Park, S. Park, and J. Kim, "Simultaneous measurement of humidity and temperature with CYTOP-reduced graphene oxide-overlaid two-mode optical fiber sensor," Sens. Actuators B **298**, 126841 (2019).

87. Y. Li, H. Ma, L. Gan, Q. Liu, Z. Yan, D. Liu, and Q. Sun, "Immobilized optical fiber microprobe for selective and high sensitive glucose detection," Sens. Actuators B **255**, 3004–3010 (2018).

88. D. Sun, S. Xu, Y. Fu, and J. Ma, "Fast response microfiber-optic pH sensor based on a polyaniline sensing layer," Appl. Opt. **59**, 11261–11265 (2020).

89. P. Wang, H. Zhao, X. Wang, G. Farrell, and G. Brambilla, "A review of multimode interference in tapered optical fibers and related applications," Sensors **18**, 858 (2018).

90. S. Korposh, S. W. James, S.-W. Lee, and R. P. Tatam, "Tapered optical fibre sensors: current trends and future perspectives," Sensors **19**, 2294 (2019).

91. P. R. Horche, M. López-Amo, M. A. Muriel, and J. A. Martin-Pereda, "Spectral behavior of a low-cost all-fiber component based on untapered multifiber unions," IEEE Photonics Technol. Lett. **1**, 184–187 (1989).

92. A. Kumar, R. K. Varshney, and P. Sharma, "Transmission characteristics of SMS fiber optic sensor structures," Opt. Commun. **219**, 215–219 (2003).

93. Y. Jung, S. Kim, D. Lee, and K. Oh, "Compact three segmented multimode fibre modal interferometer for high sensitivity refractive-index measurement," Meas. Sci. Technol. **17**, 1129 (2006).

94. Q. Wang, G. Farrell, and W. Yan, "Investigation on single-mode–multimode–single-mode fiber structure," J. Lightwave Technol. **26**, 512–519 (2008).

95. P. Wang, G. Brambilla, M. Ding, Y. Semenova, Q. Wu, and G. Farrell, "Investigation of single-mode–multimode–single-mode and single-mode–tapered-multimode–single-mode fiber structures and their application for refractive index sensing," J. Opt. Soc. Am. B **28**, 1180–1186 (2011).

96. J. Antonio-Lopez, D. May-Arrioja, and P. LiKamWa, "Optofluidic tuning of multimode interference fiber filters," in *Enabling Photonics Technologies for Defense, Security, and Aerospace Applications V* (SPIE , 2009), p. 73390D .

97. Y. Zhao, J. Zhao, and Q. Zhao, "Review of no-core optical fiber sensor and applications," Sens. Actuators, A **313**, 112160 (2020).

98. K. Wang, X. Dong, M. H. Köhler, P. Kienle, Q. Bian, M. Jakobi, and A. W. Koch, "Advances in optical fiber sensors based on multimode interference (MMI): a review," IEEE Sens. J. **21**, 132–142 (2020).

99. Q. Wu, Y. Qu, J. Liu, J. Yuan, S.-P. Wan, T. Wu, X.-D. He, B. Liub, D. Liuc, and Y. Ma, "Singlemode-multimode-singlemode fiber structures for sensing applications – a review," IEEE Sens. J. **21** , 12734–12751 (2021).

100. J. R. Guzmán-Sepúlveda, R. Guzmán-Cabrera, and A. A. Castillo-Guzmán, "Optical sensing using fiber-optic multimode interference devices: a review of nonconventional sensing schemes," Sensors **21**, 1862 (2021).

101. R. X. Gao, Q. Wang, F. Zhao, B. Meng, and S. L. Qu, "Optimal design and fabrication of SMS fiber temperature sensor for liquid," Opt. Commun. **283**, 3149–3152 (2010).

102. A. M. Hatta, Y. Semenova, G. Rajan, P. Wang, J. Zheng, and G. Farrell, "Analysis of temperature dependence for a ratiometric wavelength measurement system using SMS fiber structure based edge filters," Opt. Commun. **283**, 1291–1295 (2010).

103. Q. Wu, Y. Semenova, A. M. Hatta, P. Wang, and G. Farrell, "Bent SMS fibre structure for temperature measurement," Electron. Lett. **46**, 1129–1130 (2010).

104. A. M. Hatta, K. Indriawati, T. Bestariyan, T. Humada, and Sekartedjo, "SMS fiber structure for temperature measurement using an OTDR," Photonic Sens. **3**, 262–266 (2013).

105. Y. Zhang, X. Tian, L. Xue, Q. Zhang, L. Yang, and B. Zhu, "Super-high sensitivity of fiber temperature sensor based on leaky-mode bent SMS structure," IEEE Photonics Technol. Lett. **25**, 560–563 (2013).

106. M. Kumar, A. Kumar, and S. M. Tripathi, "A comparison of temperature sensing characteristics of SMS structures using step and graded index multimode fibers," Opt. Commun. **312**, 222–226 (2014).

107. X. Q. Lei, Y. T. Yu, W. J. Feng, B. J. Peng, and X. D. Li, "A novel fiber temperature sensor with liquid-crystal filled SM-NC-SM structure," J. Optoelectron. Laser **26**, 2278–2282 (2015).

108. Q. Wu, M. Yang, J. Yuan, H. P. Chan, Y. Ma, Y. Semenova, P. Wang, C. Yu, and G. Farrell, "The use of a bend singlemode-multimode-singlemode (SMS) fibre structure for vibration sensing," Opt. Laser Technol. **63**, 29–33 (2014).

109. J. W. Costa, M. A. R. Franco, V. A. Serrão, C. M. B. Cordeiro, and M. T. R. Giraldi, "Macrobending SMS fiber-optic anemometer and flow sensor," Opt. Fiber Technol. **52**, 101981 (2019).

110. Z. Shuo, D. Sifan, W. Zemin, S. Cuiting, C. Xudong, M. Yiwei, Z. Lei, L. Chunlian, G. Tao, Y. Wenlei, and Y. Libo, "A miniature SMS-LPG bending sensor with high sensitivity based on multimode fiber embedded-LPG," Sens. Actuators, A **295**, 31–36 (2019).

111. A. M. Hatta, H. E. Permana, H. Setijono, A. Kusumawardhani, and Sekartedjo, "Strain measurement based on SMS fiber structure sensor and OTDR," Microw. Opt. Technol. Lett. **55**, 2576–2578 (2013).

112. Y. Sun, D. Liu, P. Lu, Q. Sun, W. Yang, S. Wang, L. Liu, and W. Ni, "High sensitivity optical fiber strain sensor using twisted multimode fiber based on SMS structure," Opt. Commun. **405**, 416–420 (2017).

113. K. Saitoh and S. Matsuo, "Multicore fiber technology," J. Lightwave Technol. **34**, 55–66 (2016).

114. J. P. Moore and M. D. Rogge, "Shape sensing using multi-core fiber optic cable and parametric curve solutions," Opt. Express **20**, 2967–2973 (2012).

115. I. Floris, J. M. Adam, P. A. Calderón, and S. Sales, "Fiber optic shape sensors: a comprehensive review," Opt. Lasers Eng. **139**, 106508 (2021).

116. A. Azmi, A. Abdullah, M. M. Noor, M. Ibrahim, R. R. Ibrahim, T. Tan, and J. Zhang, "Dynamic bending and rotation sensing based on high coherence interferometry in multicore fiber," Opt. Laser Technol. **135**, 106716 (2021).

117. Z. Zhao, L. Shen, Y. Dang, C. Lu, and M. Tang, "Enabling long range distributed vibration sensing using multicore fiber interferometers," Opt. Lett. **46**, 3685–3688 (2021).

118. D. Yan, Z. Tian, N.-K. Chen, L. Zhang, Y. Yao, Y. Xie, P. P. Shum, K. T. Grattan, and D. Wang, "Observation of split evanescent field distributions in tapered multicore fibers for multiline nanoparticle trapping and microsensing," Opt. Express **29**, 9532–9543 (2021).

119. W. Chen, Y. Zhang, H. Yang, Y. Qiu, H. Li, Z. Chen, and C. Yu, "Non-invasive measurement of vital signs based on seven-core fiber interferometer," IEEE Sens. J. **21**, 10703–10710 (2021).

120. Z. Li, Y.-X. Zhang, W.-G. Zhang, L.-X. Kong, Y. Yue, and T.-Y. Yan, "Parallelized fiber Michelson interferometers with advanced curvature sensitivity plus abated temperature crosstalk," Opt. Lett. **45**, 4996–4999 (2020).

121. D. Guo, L. Wu, H. Yu, A. Zhou, Q. Li, F. Mumtaz, C. Du, and W. Hu, "Tapered multicore fiber interferometer for refractive index sensing with graphene enhancement," Appl. Opt. **59**, 3927–3932 (2020).

122. Y. Chunxia, D. Hui, D. Wei, and X. Chaowei, "Weakly-coupled multicore optical fiber taper-based high-temperature sensor," Sens. Actuators A **280**, 139–144 (2018).

123. C. Zhang, T. Ning, J. Li, L. Pei, C. Li, and H. Lin, "Refractive index sensor based on tapered multicore fiber," Opt. Fiber Technol. **33**, 71–76 (2017).

124. R. Zhou, X. Qiao, R. Wang, F. Chen, and W. Ma, "An optical fiber sensor based on lateral-offset spliced seven-core fiber for bending and stretching strain measurement," IEEE Sens. J. **20**, 5915–5920 (2020).

125. C. Zhang, T. Ning, J. Zheng, X. Gao, H. Lin, J. Li, L. Pei, and X. Wen, "Miniature optical fiber temperature sensor based on FMF-SCF structure," Opt. Fiber Technol. **41**, 217–221 (2018).

126. T. A. Birks, I. Gris-Sanchez, S. Yerolatsitis, S. G. Leon-Saval, and R. R. Thomsons, "The photonic lantern," Adv. Opt. Photon. **7**, 107–167 (2015).

127. S. Lacroix, F. Gonthier, and J. Bures, "Modeling of symmetric 2×2 fused-fiber couplers," Appl. Opt. **33**, 8361–8369 (1994).

128. A. Radosavljević, A. Daničić, J. Petrovic, A. Maluckov, and L. Hadžievski, "Coherent light propagation through multicore optical fibers with linearly coupled cores," J. Opt. Soc. Am. B **32** , 2520–2527 (2015).

129. W. Ren, Z. Tan, and G. Ren, "Analytical formulation of supermodes in multicore fibers with hexagonally distributed cores," IEEE Photon. J. **7**, 7100311 (2015).

130. J. E. Antonio-Lopez, Z. S. Eznaveh, P. LiKamWa, A. Schülzgen, and R. Amezcua-Correa, "Multicore fiber sensor for high-temperature applications up to 1000 °C," Opt. Lett. **39**, 4309–4312 (2014).

131. J. A. Flores-Bravo, R. Fernández, E. A. Lopez, A. Schülzgen, A. Amezcua-Correa, and J. Villatoro, "Simultaneous sensing of refractive index and temperature with supermode interference," J. Lightwave Technol. **39**, 7351–7357 (2021)

132. J. Amorebieta, G. Durana, A. Ortega-Gomez, R. Fernández, J. Velasco, I. S. de Ocáriz, J. Zubia, J. E. Antonio-López, A. Schülzgen, and R. Amezcua-Correa, "Packaged multi-core fiber interferometer for high-temperature sensing," J. Lightwave Technol. **37**, 2328–2334 (2019).

133. J. Villatoro, A. Van Newkirk, E. Antonio-Lopez, J. Zubia, A. Schülzgen, and R. Amezcua-Correa, "Ultrasensitive vector bending sensor based on multicore optical fiber," Opt. Lett. **41**, 832–835 (2016).

134. J. Amorebieta, A. Ortega-Gomez, G. Durana, R. Fernández, E. Antonio-Lopez, A. Schülzgen, J. Zubia, R. Amezcua-Correa, and J. Villatoro, "Highly sensitive multicore fiber accelerometer for low frequency vibration sensing," Sci. Rep. **10**, 1–11 (2020).

135. N. Cuando-Espitia, M. A. Fuentes-Fuentes, D. A. May-Arrioja, I. Hernández-Romano, R. Martínez-Manuel, and M. Torres-Cisneros, "Dual-point refractive index measurements using coupled seven-core fibers," J. Lightwave Technol. **39**, 310–319 (2021).

136. Y. Geng, X. Li, X. Tan, Y. Deng, and Y. Yu, "In-line flat-top comb filter based on a cascaded all-solid photonic bandgap fiber intermodal interferometer," Opt. Express **21**, 17352–17358 (2013).

137. S. Dong, B. Dong, C. Yu, and Y. Guo, "High sensitivity optical fiber curvature sensor based on cascaded fiber interferometer," J. Lightwave Technol. **36**, 1125–1130 (2017).

138. T. Claes, W. Bogaerts, and P. Bienstman, "Experimental characterization of a silicon photonic biosensor consisting of two cascaded ring resonators based on the Vernier-effect and introduction of a curve fitting method for an improved detection limit," Opt. Express **18** , 22747–22761 (2010).

139. F. Wei, D. Liu, Z. Wang, Z. Wang, G. Farrell, Q. Wu, G.-D. Peng, and Y. Semenova, "Enhancing the visibility of Vernier effect in a tri-microfiber coupler fiber loop interferometer for ultrasensitive refractive index and temperature sensing," J. LightwaveTechnol. **39**, 1523–1529 (2021).

140. J. Villatoro, "Phase-shifted modal interferometers for high-accuracy optical fiber sensing," Opt. Lett. **45**, 21–24 (2020).

141. J. Villatoro, J. Amorebieta, A. Ortega-Gomez, E. Antonio-Lopez, J. Zubia, A. Schülzgen, and R. Amezcua-Correa, "Composed multicore fiber structure for direction-sensitive curvature monitoring," APL Photonics **5**, 070801 (2020).

142. I. Del Villar, C. R. Zamarreno, M. Hernaez, F. J. Arregui, and I. R. Matias, "Lossy mode resonance generation with indium-tin-oxide-coated optical fibers for sensing applications," J. Lightwave Technol. **28**, 111–117 (2010).

143. E. I. Golant, A. B. Pashkovskii, and K. M. Golant, "Lossy mode resonance in an etched-out optical fiber taper covered by a thin ITO layer," Appl. Opt. **59**, 9254–9258 (2020).

144. F. Chiavaioli and D. Janner, "Fiber optic sensing with lossy mode resonances: applications and perspectives," J. Lightwave Technol. **39** , 3855–3870 (2021).

145. F. Esposito, L. Sansone, A. Srivastava, F. Baldini, S. Campopiano, F. Chiavaioli, M. Giordano, A. Giannetti, and A. Iadicicco, "Long period grating in double cladding fiber coated with graphene oxide as high-performance optical platform for biosensing," Biosens. Bioelectron. **172**, 112747 (2021).

146. D. Villar, C. R. Zamarreño, P. Sanchez, M. Hernaez, C. F. Valdivielso, F. J. Arregui, and I. R. Matias, "Generation of lossy mode resonances by deposition of high-refractive-index coatings on uncladded multimode optical fibers," J. Opt. **12**, 095503 (2010).

147. A. Yariv and P. Yeh, *Photonics: Optical Electronics in Modern Communications*, 6th ed., (Oxford U. Press, 2006).

148. K. O. Hill, B. Malo, K. A. Vineberg, F. Bilodeau, D. C. Johnson, and I. Skinner, "Efficient mode conversion in telecommunication fibre using externally written gratings," Electron. Lett. **26**, 1270–1272 (1990).

149. A. M. Vengsarkar, P. J. Lemaire, J. B. Judkins, V. Bahtia, T. Erdogan, and J. E. Sipe, "Long-period fiber gratings as band-rejection filters," J. Lightwave Technol. **14**, 58–65 (1996).

150. K. O. Hill, Y. Fujii, D. C. Johnson, and B. S. Kawasaki, "Photosensitivity in optical fiber waveguides: application to reflection filter fabrication," Appl. Phys. Lett. **32**, 647–649 (1978).

151. G. Meltz, W. W. Morey, and W. H. Glenn, "Formation of Bragg gratings in optical fibers by a transverse holographic method," Opt. Lett. **15**, 823–825 (1989).

152. K. O. Hill and G. Meltz, "Fiber Bragg grating technology fundamentals and overview," J. Lightwave Technol. **15**, 1263–1276 (1997).

153. Z. Xiong, G. D. Peng, B. Wu, and P. L. Chu, "Highly tunable Bragg gratings in single-mode polymer optical fibers," IEEE Photon. Technol. Lett. **11**, 352–354 (1999).

154. A. Theodosiou, A. Lacraz, A. Stassis, C. Koutsides, M. Komodromos, and K. Kalli, "Plane-by-plane femtosecond laser inscription method for single-peak Bragg gratings in multimode CYTOP polymer optical fiber," J. Lightwave Technol. **35**, 5404–5410 (2017).

155. I. P. Johnson, W. Yuan, A. Stefani, K. Nielsen, H. K. Rasmussen, L. Khan, D. J. Webb, K. Kalli, and O. Bang, "Optical fibre Bragg grating recorded in TOPAS cyclic olefin copolymer," Electron. Lett. **47**, 271–272 (2011).

156. G. Woyessa, A. Fasano, C. Markos, A. Stefani, H. K. Rasmussen, and O. Bang, "Zeonex microstructured polymer optical fiber: fabrication friendly fibers for high temperature and humidity insensitive Bragg grating sensing," Opt. Mater. Express **7**, 286–295 (2017).

157. T. Guo, Á González-vila, M. Loyez, and C. Caucheteur, "Plasmonic optical fiber grating immunosensing: a review," Sensors **17**, 1–19 (2017).

158. P. J. Lemaire, R. M. Atkins, V. Mizrahi, and W. A. Reed, "High pressure H_2 loading as a technique for achieving ultrahigh UV photosensitivity and thermal sensitivity in GeO_2 doped optical fibres," Electron. Lett. **29**, 1191–1193 (1993).

159. C. L. Liou, L. A. Wang, M. C. Shih, and T. J. Chuang, "Characteristics of hydrogenated fiber Bragg gratings," Appl. Phys. A **64**, 191–197 (1997).

160. K. Hill, B. Malo, F. Bilodeau, D. C. Johnson, and J. Albert, "Bragg gratings fabricated in monomode photosensitive optical fiber by UV exposure through a phase mask," Appl. Phys. Lett. **62**, 1035–1037 (1993).

161. C. G. Askins, M. A. Putnam, G. M. Williams, and E. J. Friebele, "Stepped-wavelength optical-fiber Bragg grating arrays fabricated in line on a draw tower," Opt. Lett. **19**, 147–149 (1994).

162. K. Oi, F. Barnier, and M. Obara, "Fabrication of fiber Bragg grating by femtosecond laser interferometry, " in 14th Annual Meeting of the IEEE Lasers and Electro-Optics Society (IEEE/OSA, 2001), pp. 776–777 .

163. A. Dragomir, D. N. Nikogosyan, K. A. Zagorulko, P. G. Kryukov, and E. M. Dianov, "Inscription of fiber Bragg gratings by ultraviolet femtosecond radiation," Opt. Lett. **28**, 2171–2173 (2003).

164. S. J. Mihailov, C. W. Smelser, P. Lu, R. B. Walker, D. G. H. Ding, G. Henderson, and J. Unruh, "Fiber Bragg gratings made with a phase mask and 800-nm femtosecond radiation," Opt. Lett. **28**, 995–997 (2003).

165. A. Martinez, M. Dubov, I. Khrushchev, and I. Bennion, "Direct writing of fibre Bragg gratings by femtosecond laser," Electron. Lett. **40** , 1170–1172 (2004).

166. A. D. Kersey, M. A. Davis, H. J. Patrick, M. Leblanc, K. P. Koo, C. G. Askins, M. A. Putnam, and E. J. Friebele, "Fiber grating sensors," J. Lightwave Technol. **15** , 1442–1463 (1997).

167. J. Canning, "Fibre gratings and devices for sensors and lasers," Laser Photon. Rev. **2**, 275–289 (2008).

168. J. L. Archambault, L. Reekie, and P. S. J. Russell, "100% reflectivity Bragg reflectors produced in optical fibres by single excimer laser pulses," Electron. Lett. **29**(5), 453–455 (1993).

169. B. Sutapun, M. Tabib-Azar, and A. Kazemi, "Pd-coated elastooptic fiber optic Bragg grating sensors for multiplexed hydrogen sensing," Sens. Actuators B **60**, 27–34 (1999).

170. C. Caucheteur, M. Debliquy, D. Lahem, and P. Mégret, "Hybrid fiber gratings coated with a catalytic sensitive layer for hydrogen sensing in air," Opt. Express **16**, 16854–16859 (2008).

171. V. Bhatia and A. M. Vengsarkar, "Optical fiber long-period grating sensors," Opt. Lett. **21**, 692–694 (1996).

172. V. Bhatia, "Applications of long-period gratings to single and multi-parameter sensing," Opt. Express **4**, 457–466 (1999).

173. T. Erdogan and V. Mizrahi, "Characterization of UV-induced birefringence in photosensitive Ge-doped silica optical fibers," J. Opt. Soc. Am. B **11**, 2100–2105 (1994).

174. C. Caucheteur, S. Bette, R. Garcia-Olcina, M. Wuilpart, S. Sales, J. Capmany, and P. Mégret, "Transverse strain measurements using the birefringence effect in fiber Bragg gratings," Photon. Technol. Lett. **19** , 966–968 (2007).

175. X. Shu, L. Zhang, and I. Bennion, "Sensitivity characteristics of long-period fiber gratings," J. Lightwave Technol. **20**, 255–266 (2002).

176. K. Zhou, L. Zhang, X. Chen, and I. Bennion, "Low thermal sensitivity grating devices based on ex-45° tilting structure capable of forward-propagating cladding modes coupling," J. Lightwave Technol. **24**, 5087–5094 (2006).

177. Z. Yan, Q. Sun, C. Wang, Z. Sun, C. Mou, K. Zhou, D. Liu, and L. Zhang, "Refractive index and temperature sensitivity characterization of excessively tilted fiber grating," Opt. Express **25**, 3336–3346 (2017).

178. E. Anemogiannis, E. N. Glytsis, and T. K. Gaylord, "Transmission characteristics of long-period fiber gratings having arbitrary azimuthal/radial refractive index variations," J. Light.Technol. **21** , 218–227 (2003).

179. W. Zhou, D. J. Mandia, S. T. Barry, and J. Albert, "Absolute near-infrared refractometry with a calibrated tilted fiber Bragg grating," Opt. Lett. **40**, 1713 (2015).

180. C. Caucheteur, T. Guo, F. Liu, B.-O. Guan, and J. Albert, "Ultrasensitive plasmonic sensing in air using optical fibre spectral combs," Nat. Commun. **7**, 13371 (2016).

181. D. Feng, J. Albert, Y. Jiang, C. Liu, B. Jiang, H. Wang, and J. Zhao, "Symmetry selective cladding modes coupling in ultrafast-written fiber Bragg gratings in two-mode fiber," Opt. Express **27**, 18410–18420 (2019).

182. A. Ioannou, A. Theodosiou, C. Caucheteur, and K. Kalli, "Femtosecond laser inscribed tilted gratings for leaky mode excitation in optical fibers," J. Lightwave Technol. **38** , 1921–1928 (2020).

183. J. W. Fleming, "Dispersion in GeO_2 -SiO_2 glasses," Appl. Opt. **23**(24), 4486–4493 (1984).

184. J. Albert, "Permanent photoinduced refractive-index changes for Bragg gratings in silicate glass waveguides and fiber," MRS Bull. **23** , 36–41 (1998).

185. X. Zhang, S. Cai, F. Liu, H. Chen, P. Yan, Y. Yuan, T. Guo, and J. Albert, "*In situ* determination of the complex permittivity of ultrathin H_2-infused palladium coatings for plasmonic fiber optic sensors in the near infrared," J. Mater. Chem. C **6**, 5161–5170 (2018).

186. F. Liu and J. Albert, "40 GHz-rate all-optical cross-modulation of core-guided near infrared light in single mode fiber by surface plasmons on gold-coated tilted fiber Bragg gratings," APL Photonics **4**, 126104 (2019).

187. F. Liu, X. Zhang, K. Li, T. Guo, A. Ianoul, and J. Albert, "Discrimination of bulk and surface refractive index change in plasmonic sensors with narrow bandwidth resonance combs," ACS Sens. **6**, 3013–3023 (2021).

188. A. Ivanov, "Multi-parameter fiber optic sensors for structural health monitoring," M.A.Sc. thesis (Carleton University, 2008).

189. Commercial literature from Ibsen Photonics , https://ibsen.com/products/interrogation-monitors/i-mon-usb/i-mon-256-512-usb/.

190. S. D. Dyer, P. A. Williams, R. J. Espejo, J. D. Kofler, and S. M. Etzel, "Fundamental limits in fiber Bragg grating peak wavelength measurements (invited paper)," Proc. SPIE **5855**, 88–93 (2005).

191. F. Liu, X. Tong, C. Zhang, C. Deng, Q. Xiong, Z. Zheng, and P. Wang, "Multipeak detection algorithm based on the Hilbert transform for optical FBG sensing," Opt. Fiber Technol. **45**, 47–52 (2018).

192. Y. Yang, J. Wu, M. Wang, Q. Wang, Q. Yu, and K. P. Chen, "Fast demodulation of fiber Bragg grating wavelength from low-resolution spectral measurements using Buneman frequency estimation," J. Lightwave Technol. **38**, 5142–5148 (2020).

193. D. Ganziy, B. Rose, and O. Bang, "Compact multichannel high-resolution microelectro-mechanical systems-based interrogator for Fiber Bragg grating sensing," Appl. Opt. **56**, 3622–3627 (2017).

194. M. P. Fernandez, L. A. Bulus Rossini, J. L. Cruz, M. V. Andres, and P. A. Costanzo Caso, "High-speed and high-resolution interrogation of FBG sensors using wavelength-to-time mapping and gaussian filters," Opt. Express **27**, 36815–36823 (2019).

195. J. Wang, T. Huang, F. Duan, Q. Cheng, F. Zhang, and X. Qu, "Fast peak-tracking method for FBG reflection spectrum and nonlinear error compensation," Opt. Lett. **45**, 451–454 (2020).

196. M. Shaimerdenova, A. Bekmurzayeva, M. Sypabekova, and D. Tosi, "Interrogation of coarsely sampled tilted fiber Bragg grating (TFBG) sensors with KLT," Opt. Express **25**, 33487–33496 (2017).

197. F. Ouellette, J. Li, Z. Ou, and J. Albert, "High-resolution interrogation of tilted fiber Bragg gratings using an extended range dual wavelength differential detection," Opt. Express **28**, 14662–14676 (2020).

198. K. A. Tomyshev, D. K. Tazhetdinova, E. S. Manuilovich, and O. V. Butov, "High-resolution fiber optic surface plasmon resonance sensor for biomedical applications," J. Appl. Phys. **124**, 113106 (2018).

199. K. A. Tomyshev, E. S. Manuilovich, D. K. Tazhetdinova, E. I. Dolzhenko, and O. V. Butov, "High-precision data analysis for TFBG-assisted refractometer," Sens. Act. A **308**, 112016 (2020).

200. T. Gang, F. Liu, M. Hu, and J. Albert, "Integrated differential area method for variable sensitivity interrogation of tilted fiber Bragg grating sensors," J. Lightwave Technol. **37**, 4531–4536 (2019).

201. L. Fazzi and R. M. Groves, "Demodulation of a tilted fibre Bragg grating transmission signal using α-shape modified Delaunay triangulation," Measurement **166**, 108197 (2020).

202. M. Lobry, M. Loyez, K. Chah, E. M. Hassan, E. Goormaghtigh, M. C. DeRosa, R. Wattiez, and C. Caucheteur, "HER2 biosensing through SPR-envelope tracking in plasmonic optical fiber gratings," Biomed. Opt. Express **11**, 4862–4871 (2020).

203. W. Yuan, Q. Zhao, L. Li, Y. Wang, and C. Yu, "Simultaneous measurement of temperature and curvature using ring-core fiber-based Mach-Zehnder interferometer," Opt. Express **29**, 17915–17925 (2021).

204. Q. Chen, D. N. Wang, and F. Gao, "Simultaneous refractive index and temperature sensing based on a fiber surface waveguide and fiber Bragg gratings," Opt. Lett. **46**, 1209–1212 (2021).

205. T. Osuch, T. Jurek, K. Markowski, and K. Jedrzejewski, "Simultaneous measurement of liquid level and temperature using tilted fiber Bragg grating," IEEE Sens. J. **16**, 1205–1209 (2016).

206. P. Kisala, D. Harasim, and J. Mroczka, "Temperature-insensitive simultaneous rotation and displacement (bending) sensor based on tilted fiber Bragg grating," Opt. Express **24**, 29922–29929 (2016).

207. S. Upendar, M. A. Schmidt, and T. Weiss, "What optical fiber modes reveal: group velocity and effective index for external perturbations," J. Opt. Soc. Am. B **38**, 1097–1103 (2021).

208. J. Jin, Y. Zhang, Y. Zhu, D. Zhang, and H. Zhang, "Analysis and correction method of axial strain error in multi-core fiber shape sensing," IEEE Sensors J. **20**, 12716–12722 (2020).

209. S. Bandyopadhyay, L. shao, M. Smietana, C. Wang, J. Hu, G. Wang, W. He, G. Gu, and Y. Yang, "Employing higher order cladding modes of fiber Bragg grating for analysis of refractive index change in volume and at the surface," IEEE Photonics J. **12**, 7100313 (2020).

210. H. J. W. M. Hoekstra and M. Hammer, "General relation for group delay and the relevance of group delay for refractometric sensing," J. Opt. Soc. Am. B **31**, 1561–1567 (2014).

211. M. Cavillon, M. Lancry, B. Poumellec, Y. Wang, J. Canning, K. Cook, T. Hawkins, P. Dragic, and J. Ballato, "Overview of high temperature fibre Bragg gratings and potential improvement using highly doped aluminosilicate glass optical fibres," J. Phys.: Photonics **1**, 042001 (2019).

212. C. Zhu, D. Alla, and J. Huang, "High-temperature stable FBGs fabricated by a point-by-point femtosecond laser inscription for multi-parameter sensing," OSA Continuum **4**, 355–363 (2021).

213. N. Safari-Yazd, K. Chah, C. Caucheteur, and P. Mégret, "Thermal regeneration of tilted Bragg gratings UV photo-inscribed in hydrogen-loaded standard optical fibers," J. Lightwave Technol. **39**, 3582–3590 (2021).

214. X. Rosello-Mecho, M. Delgado-Pinar, A. Diez, and M. V. Andres, "Measurement of Pockels' coefficients and demonstration of the anisotropy of the elasto-optic effect in optical fibers under axial strain," Opt. Lett. **41**, 2934–2937 (2016).

215. J. Villatoro, O. Arrizabalaga, G. Durana, I. Sáez de Ocáriz, E. Antonio-Lopez, J. Zubia, A. Schülzgen, and R. Amezcua-Correa, "Accurate strain sensing based on super-mode interference in strongly coupled multi-core optical fibres," Sci. Rep. **7**, 4451 (2017).

216. V. Voisin, C. Caucheteur, P. Mégret, and J. Albert, "Anomalous effective strain-optic constants of nonparaxial optical fiber mode," Opt. Lett. **39**, 578 (2014).

217. F. Khan, A. Denasi, D. Barrera, J. Madrigal, S. Sales, and S. Misra, "Multi-core optical fibers with Bragg gratings as shape sensor for flexible medical instruments," IEEE Sens. J. **19**, 5878–5884 (2019).

218. T. Kissinger, E. Chehura, S. E. Staines, S. W. James, and R. P. Tatam, "Dynamic fiber-optic shape sensing using fiber segment interferometry," J. Lightwave Technol. **36**, 917–925 (2018).

219. R. T. Schermer and J. H. Cole, "Improved bend loss formula verified for optical fiber by simulation and experiment," IEEE J. Quantum Electron. **43**, 899–909 (2007).

220. L. Shao, L. Xiong, C. Chen, A. Laronche, and J. Albert, "Directional bend sensor based on re-grown tilted fiber Bragg grating," J. Lightwave Technol. **28** , 2681–2687 (2010).

221. D. Feng, J. Albert, Y. Hou, B. Jiang, Y. Jiang, Y. Ma, and J. Zhao, "Co-located angularly offset fiber Bragg grating pair for temperature-compensated unambiguous 3D shape sensing," Appl. Opt. **60** , 4185–4189 (2021).

222. D. Feng, X. Qiao, and J. Albert, "Off-axis ultraviolet-written fiber Bragg gratings for directional bending measurements," Opt. Lett. **41**, 1201–1204 (2016).

223. D. Feng, W. Zhou, X. Qiao, and J. Albert, "Compact optical fiber 3D shape sensor based on a pair of orthogonal tilted fiber Bragg gratings," Sci. Rep. **5**, 17415 (2015).

224. H. Fan, L. Chen, and X. Bao, "Fiber-optic ultrasound transmitter based on multi-mode interference in curved adhesive waveguide," IEEE Photon. Technol. Lett. **32**, 325–328 (2020).

225. H. Fan, L. Zhang, S. Gao, L. Chen, and X. Bao, "Ultrasound sensing based on an in-fiber dual-cavity Fabry-Pérot interferometer," Opt. Lett. **44**, 3606–3609 (2020).

226. H. Fan, L. Chen, and X. Bao, "Chalcogenide microfiber-assisted silica microfiber for ultrasound detection," Opt. Lett. **45**, 1128–1131 (2020).

227. H. Fan, W. Ma, L. Chen, and X. Bao, "Ultracompact twisted silica taper for 20 kHz to 94 MHz ultrasound sensing," Opt. Lett. **45**, 3889–3892 (2020).

228. B. Gu, W. Qi, Y. Zhou, Z. Wu, P. P. Shum, and F. Luan, "Reflective liquid level sensor based on modes conversion in thin-core fiber incorporating tilted fiber Bragg grating," Opt. Express **22**, 11834–11839 (2014).

229. C. Shen, X. Lian, V. Kavungal, C. Zhong, D. Liu, Y. Semenova, G. Farrell, J. Albert, and J. F. Donegan, "Optical spectral sweep comb liquid flow rate sensor," Opt. Lett. **43**, 751–754 (2018).

230. C. Shen, D. Liu, X. Lian, T. Lang, C. Zhao, Y. Semenova, and J. Albert, "Microfluidic flow direction and rate vector sensor based on a partially gold-coated TFBG," Opt. Lett. **45**, 2776–2779 (2020).

231. C. Shen, C. Zhong, D. Liu, X. Xian, J. Zheng, J. Wang, Y. Semenova, G. Farrell, J. Albert, and J. F. Donegan, "Measurements of milli-Newton surface tension forces with tilted fiber Bragg gratings," Opt. Lett. **43**, 2–5 (2018).

232. A. Sihvola, *Electromagnetic Mixing Formulas and Applications* (IEEE Press, , 1999).

233. C. Shen, W. Zhou, and J. Albert, "Polarization-resolved evanescent wave scattering from gold-coated tilted fiber gratings," Opt. Express **22**, 5277 (2014).

234. C. Shen, L. Xiong, A. Bialiayeu, Y. Zhang, and J. Albert, "Polarization-resolved near- and far-field radiation from near-infrared tilted fiber Bragg gratings," J. Lightwave Technol. **32**, 2157–2162 (2014).

235. J.-M. Renoirt, M. Debliquy, J. Albert, A. Ianoul, and C. Caucheteur, "Surface plasmon resonances in oriented silver nanowire coatings on optical fibers," J. Phys. Chem. C **118**, 11035–11042 (2014).

236. D. J. Mandia, W. Zhou, J. Albert, and S. T. Barry, "CVD on optical fibers: tilted fiber Bragg gratings as real-time sensing platforms," Chem. Vap. Depos. **21**, 4–20 (2015).

237. Y. Yuan, T. Guo, X. Qiu, J. Tang, Y. Huang, L. Zhuang, S. Zhou, Z. Li, B. Guan, X. Zhang, and J. Albert, "Electrochemical surface plasmon resonance fiber-optic sensor: *in-situ* detection of electroactive biofilms," Anal. Chem. **88**, 7609–7616 (2016).

238. A. Bialiayeu, C. Caucheteur, N. Ahamad, A. Ianoul, and J. Albert, "Self-optimized metal coating for fiber plasmonics by electroless deposition," Opt. Express **19**, 18742–18753 (2011).

239. W. Zhou, D. J. Mandia, M. B. E. Griffiths, A. Bialiayeu, Y. Zhang, P. G. Gordon, S. T. Barry, and J. Albert, "Polarization-dependent properties of the cladding modes of single mode fiber covered with gold nanoparticles," Opt. Express **21**, 245–255 (2013).

240. D. J. Mandia, M. B. E. Griffiths, W. Zhou, P. G. Gordon, J. Albert, and S. T. Barry, "*In situ* deposition monitoring by a tilted fiber Bragg grating optical probe: probing nucleation in chemical vapour deposition of gold," Phys. Procedia **46**, 12–20 (2013).

241. L. Y. Shao, J. P. Coyle, S. T. Barry, and J. Albert, "Anomalous permittivity and plasmon resonances of copper nanoparticle conformal coatings on optical fibers," Opt. Mater. Express **1**, 128–137 (2011).

242. A. Bialiayeu, A. Bottomley, D. Prezgot, A. Ianoul, and J. Albert, "Plasmon-enhanced refractometry using silver nanowire coating on tilted fiber Bragg gratings," Nanotechnology **23**, 444012 (2012).

243. J. M. Renoirt, C. Zhang, M. Debliquy, M. G. Olivier, P. Megret, and C. Caucheteur, "High-refractive-index transparent coatings enhance the optical fiber cladding modes refractometric sensitivity," Opt. Express **21**, 29073–29082 (2013).

244. S. Lepinay, A. Staff, A. Ianoul, and J. Albert, "Improved detection limits of protein optical fiber biosensors coated with gold nanoparticles," Biosens. Bioelectron. **52**, 337–344 (2014).

245. D. J. Mandia, W. Zhou, M. J. Ward, H. Joress, J. J. Sims, J. B. Giorgi, J. Albert, and S. T. Barry, "The effect of ALD-grown Al_2O_3 on the refractive index sensitivity of CVD gold-coated optical fiber sensors," Nanotechnology **26**, 434002 (2015).

246. Y. Si, J. Lao, X. Zhang, Y. Liu, S. Cai, A. G. Vila, K. Li, Y. Huang, Y. Yuan, C. Caucheteur, and T. Guo, "Electrochemical plasmonic fiber-optic sensors for ultra-sensitive heavy metal detection," J. Lightwave Technol. **37**, 3495–3502 (2019).

247. M. Śmietana, T. Drażewski, P. Firek, P. Mikulic, and W. J. Bock, "Comparison of Al2O3 nano-overlays deposited with magnetron sputtering and atomic layer deposition on optical fibers for sensing purpose," in *Micro/Nano Materials, Devices, and Systems* (SPIE, 2013), p. 89231G .

248. Y. Chen, F. Tang, Y. Bao, Y. Tang, and G. Chen, "A Fe-C coated long-period fiber grating sensor for corrosion-induced mass loss measurement," Opt. Lett. **41**, 2306–2309 (2016).

249. Y. Chen, F. Tang, Y. Tang, M. J. O'Keefe, and G. Chen, "Mechanism and sensitivity of Fe-C coated long period fiber grating sensors for steel corrosion monitoring of RC structures," Corros. Sci. **127**, 70–81 (2017).

250. F. Tang, Z. Li, Y. Chen, H. N. Li, J. Huang, and M. J. O'Keefe, "Monitoring passive film growth on steel using Fe-C coated long period grating fiber sensor," IEEE Sens. J. **19**, 6748–6755 (2019).

251. R. Wang, Z. Li, X. Chen, N. Hu, Y. Xiao, K. Li, and T. Guo, "Mode Splitting in ITO-nanocoated tilted fiber Bragg gratings for vector twist measurement," J. Lightwave Technol **39** , 4151–4157 (2021).

252. A. Czapla, W. J. Bock, T. R. Wolinski, P. Mikulic, E. Nowinowski-Kruszelnicki, and R. Dabrowski, "Improving the electric field sensing capabilities of the long-period fiber grating coated with a liquid crystal layer," Opt. Express **24**, 5662–5673 (2016).

253. S. Mathews, G. Farrell, and Y. Semenova, "Liquid crystal infiltrated photonic crystal fibers for electric field intensity measurements," Appl. Opt. **50**, 2628–2635 (2011).

254. M. M. Tefelska, T. R. Wolinski, S. Ertman, K. Milenko, R. Laczkowski, A. Siarkowska, and A. W. Domanski, "Electric field sensing with photonic liquid crystal fibers based on micro-electrodes systems," J. Lightwave Technol. **33**, 2405–2411 (2015).

255. L. Gao, T. Zhu, M. Deng, K. S. Chiang, X. Sun, X. Dong, and Y. Hou, "Long-period fiber grating within D-shaped fiber using magnetic fluid for magnetic-field detection," IEEE Photonics J. **4** , 2095–2104 (2012).

256. Y. Miao, K. Zhang, B. Liu, W. Lin, H. Zhang, Y. Lu, and J. Yao, "Ferrofluid-infiltrated microstructured optical fiber long-period grating," IEEE Photonics Technol. Lett. **25** , 306–309 (2012).

257. Z. Zhang, T. Guo, X. Zhang, J. Xu, W. Xie, M. Nie, Q. Wu, B. O. Guan, and J. Albert, "Plasmonic fiber-optic vector magnetometer," Appl. Phys. Lett. **108** , 101105 (2016).

258. W. Lin, Y. Miao, H. Zhang, B. Liu, Y. Liu, B. Song, and J. Wu, "Two-dimensional magnetic field vector sensor based on tilted fiber Bragg grating and magnetic fluid," J. Lightwave Technol. **31** , 2599–2605 (2013).

259. D. Yang, L. Du, Z. Xu, Y. Jiang, J. Xu, M. Wang, Y. Bai, and H. Wang, "Magnetic field sensing based on tilted fiber Bragg grating coated with nanoparticle magnetic fluid," Appl. Phys. Lett. **104** , 061903 (2014).

260. Z. Zhang, F. Liu, Q. Ma, L. Li, and T. Guo, "Vector magnetometer based on localized scattering between optical fiber spectral combs and magnetic nanoparticles," J. Lightwave Technol. **39** , 6599–6605 (2021).

261. X. Chen, F. Du, T. Guo, J. Lao, X. Zhang, Z. Zhang, F. Liu, J. Li, C. Chen, and B.-O. Guan, "Liquid crystal-embedded tilted fiber grating electric field intensity sensor," J. Lightwave Technol. **35** , 3347–3353 (2017).

262. F. Shi, X. Bai, F. Wang, F. Pang, S. Pu, and X. Zeng, "All-fiber magnetic field sensor based on hollow optical fiber and magnetic fluid," IEEE Sens. J. **17** , 619–622 (2016).

263. J. Yin, S. Ruan, T. Liu, J. Jiang, S. Wang, H. Wei, and P. Yan, "All-fiber-optic vector magnetometer based on nano-magnetic fluids filled double-clad photonic crystal fiber," Sens. Actuators B **238**, 518–524 (2017).

264. J. Yin, P. Yan, H. Chen, L. Yu, J. Jiang, M. Zhang, and S. Ruan, "All-fiber-optic vector magnetometer based on anisotropic magnetism-manipulation of ferromagnetism nanoparticles," Appl. Phys. Lett. **110** , 231104 (2017).

265. M. Ma, H. Chen, S. Li, X. Jing, W. Zhang, and M. Wang, "Analysis of a magnetic field sensor based on a Sagnac interferometer using a magnetic fluid-filled birefringent photonic crystal fiber," IEEE Photonics J. **11** , 1–10 (2019).

266. W. Lin, Y. Miao, H. Zhang, B. Liu, Y. Liu, and B. Song, "Fiber-optic in-line magnetic field sensor based on the magnetic fluid and multimode interference effects," Appl. Phys. Lett. **103**(15), 151101 (2013).

267. S. Dong, S. Pu, and H. Wang, "Magnetic field sensing based on magnetic-fluid-clad fiber-optic structure with taper-like and lateral-offset fusion splicing," Opt. Express **22** , 19108–19116 (2014).

268. A. Layeghi and H. Latifi, "Magnetic field vector sensor by a nonadiabatic tapered Hi-Bi fiber and ferrofluid nanoparticles," Opt. Laser Technol. **102**, 184–190 (2018).

269. R. Q. Lv, Y. Zhao, D. Wang, and Q. Wang, "Magnetic fluid-filled optical fiber Fabry-Pérot sensor for magnetic field measurement," IEEE Photonics Technol. Lett. **26** , 217–219 (2013).

270. Y. Chen, W. Sun, Y. Zhang, G. Liu, Y. Luo, J. Dong, Y. Zhong, W. Zhu, J. Yu, and Z. Chen, "Magnetic nanoparticles functionalized few-mode-fiber-based plasmonic vector magnetometer," Nanomaterials **9** , 785 (2019).

271. Y. Chen, Y. Hu, H. Cheng, F. Yan, Q. Lin, Y. Chen, P. Wu, L. Chen, G. Liu, G. Peng, Y. Luo, and Z. Chen, "Side-polished single-mode-multimode-single-mode fiber structure for the vector magnetic field sensing," J. Lightwave Technol. **38** , 5837–5843 (2020).

272. C. P. Grey and J. M. Tarascon, "Sustainability and *in situ* monitoring in battery development," Nat. Mater. **16**, 45–56 (2017).

273. G. Yang, C. Leitão, Y. Li, J. Pinto, and X. Jiang, "Real-time temperature measurement with fiber Bragg sensors in lithium batteries for safety usage," Measurement **46** , 3166–3172 (2013).

274. L. H. J. Raijmakers, D. L. Danilov, R. A. Eichel, and P. H. L. Notten, "A review on various temperature-indication methods for Li-ion batteries," Appl. Energy **240**, 918–945 (2019).

275. X. Cheng and M. Pecht, "*In situ* stress measurement techniques on Li-ion battery electrodes: a review," Energies **10**, 591 (2017).

276. J. Peng, X. Zhou, S. Jia, Y. Jin, S. Xu, and J. Chen, "High precision strain monitoring for lithium ion batteries based on fiber Bragg grating sensors," J. Power Sources **443**, 226692 (2019).

277. A. Fortier, M. Tsao, N. D. Williard, Y. Xing, and M. G. Pecht, "Preliminary study on integration of fiber optic Bragg grating sensors in li-ion batteries and *in situ* strain and temperature monitoring of battery cells," Energies **10** , 838 (2017).

278. M. Nascimento, T. Paixão, M. S. Ferreira, and J. Pinto, "Thermal mapping of a lithium polymer batteries pack with FBGs network," Batteries **4** , 67 (2018).

279. S. Novais, M. Nascimento, L. Grande, M. F. Domingues, P. Antunes, N. Alberto, C. Leitao, R. Oliveira, S. Koch, G. T. Kim, S. Passerini, and J. Pinto, "Internal and external temperature monitoring of a Li-ion battery with fiber Bragg grating sensors," Sensors **16** , 1394 (2016).

280. A. Raghavan, P. Kiesel, L. W. Sommer, J. Schwartz, A. Lochbaum, A. Hegyi, A. Schuh, K. Arakaki, B. Saha, A. Ganguli, K. H. Kim, C. Kim, H. J. Hah, S. kim, G.-O. Hwang, G.-C. Chung, B. Choi, and M. Alamgir, "Embedded fiber-optic sensing for accurate internal monitoring of cell state in advanced battery management systems part 1: cell embedding method and performance," J. Power Sources **341**, 466–473 (2017).

281. A. Ganguli, B. Saha, A. Raghavan, P. Kiesel, K. Arakaki, A. Schuh, J. Schwartz, A. Hegyi, L. W. Sommer, A. Lochbaum, S. Sahu, and M. Alamgir, "Embedded fiber-optic sensing for accurate internal monitoring of cell state in advanced battery management systems part 2: internal cell signals and utility for state estimation," J. Power Sources **341**, 474–482 (2017).

282. A. R. Ghannoum, P. Nieva, A. Yu, and A. Khajepour, "Development of embedded fiber-optic evanescent wave sensors for optical characterization of graphite anodes in lithium-ion batteries," ACS Appl. Mater. Interfaces **9** , 41284–41290 (2017).

283. M. Nascimento, M. S. Ferreira, and J. L. Pinto, "Simultaneous sensing of temperature and bi-directional strain in a prismatic Li-ion battery," Batteries **4** , 23 (2018).

284. M. Nascimento, S. Movais, M. Ding, M. S. Ferreira, S. Koch, S. Passerini, and J. Pinto, "Internal strain and temperature discrimination with optical fiber hybrid sensors in Li-ion batteries," J. Power Sources **410**, 1–9 (2019).

285. T. Yamanaka, H. Nakagawa, S. Tsubouchi, Y. Domi, T. Doi, T. Abe, and Z. Ogumi, "*In situ* Raman spectroscopic studies on concentration of electrolyte salt in lithium ion batteries by using ultrafine multifiber probes," ChemSusChem **10** , 855–861 (2017).

286. J. Huang, L. A. Blanquer, J. Bonefacino, E. R. Logan, D. A. D. Corte, C. Delacourt, B. M. Gallant, S. T. Boles, J. R. Dhan, H.-Y. Tam, and J.-M. Tarascon, "Operando decoding of chemical and thermal events in commercial Na (Li)-ion cells via optical sensors," Nat. Energy **5** , 674–683 (2020).

287. J. Lao, P. Sun, F. Liu, X. Zhang, C. Zhao, W. Mai, T. Guo, G. Xiao, and J. Albert, "*In situ* plasmonic optical fiber detection of the state of charge of supercapacitors for renewable energy storage," Light: Sci. Appl. **7**, 1–12 (2018).

288. F. Chiavaioli, C. A. J. Gouveia, P. A. S. Jorge, and F. Baldini, "Towards a uniform metrological assessment of grating-based optical fiber sensors: from refractometers to biosensors," Biosensors **7**, 23 (2017).

289. Y. Liu and J. Yu, "Oriented immobilization of proteins on solid supports for use in biosensors and biochips: a review," Microchim. Acta **183**, 1–19 (2016).

290. G. Ramsay, "DNA chips: State-of-the art," Nat. Biotechnol. **16**, 40–44 (1998).

291. J. R. Crowther, *The ELISA Guidebook*, 2nd ed., (Springer International Publishing, 2009).

292. M. M. Bilek and D. R. McKenzie, "Plasma modified surfaces for covalent immobilization of functional biomolecules in the absence of chemical linkers: towards better biosensors and a new generation of medical implants," Biophys. Rev. **2**, 55–65 (2010).

293. E. Makhneva, L. Barillas, Z. Farka, M. Pastucha, P. Skládal, K.-D. Weltmann, and K. Fricke, "Functional plasma polymerized surfaces for biosensing," ACS Appl. Mater. Interfaces **12**, 17100–17112 (2020).

294. M. Oliverio, S. Perotto, G. C. Messina, L. Lovato, and F. De Angelis, "Chemical functionalization of plasmonic surface biosensors: A tutorial review on issues, strategies, and costs," ACS Appl. Mater. Interfaces **9**, 29394–29411 (2017).

295. M. L. Sham, J. Li, P. C. Ma, and J. K. Kim, "Cleaning and functionalization of polymer surfaces and nanoscale carbon fillers by UV/ozone treatment: a review," J. Compos. Mater. **43**, 1537–1564 (2009).

296. M. Asal, Ö Özen, M. Şahinler, and İ Polatoğlu, "Recent developments in enzyme, DNA and immuno-based biosensors," Sensors **18** , 1924 (2018).

297. A. Zamora-Gálvez, E. Morales-Narváez, C. C. Mayorga-Martinez, and A. Merkoçi, "Nanomaterials connected to antibodies and molecularly imprinted polymers as bio/receptors for bio/sensor applications," Appl. Mater. Today **9**, 387–401 (2017).

298. M. Loyez, J. Albert, C. Caucheteur, and R. Wattiez, "Cytokeratins biosensing using tilted fiber gratings," Biosensors **8**, 1–8 (2018).

299. A. Shakeri, N. A. Jarad, A. Leung, L. Soleymani, and T. F. Didar, "Biofunctionalization of glass- and paper-based microfluidic devices: a review," Adv. Mater. Interfaces **6**, 1–16 (2019).

300. A. K. Trilling, J. Beekwilder, and H. Zuilhof, "Antibody orientation on biosensor surfaces: a minireview," Analyst **138**, 1619–1627 (2013).

301. M. Loyez, M. Lobry, R. Wattiez, and C. Caucheteur, "Optical fiber gratings immunoassays," Sensors **19**, 2595 (2019).

302. D. Santano, A. Urrutia, C. R. Zamarreno, and I. Del Villar, "Advances in fiber optic DNA-based sensors: A Review," IEEE Sens. J. **21**, 12679–12691 (2021).

303. S. Lépinay, A. Ianoul, and J. Albert, "Molecular imprinted polymer-coated optical fiber sensor for the identification of low molecular weight molecules," Talanta **128**, 401–407 (2014).

304. M. Janczuk-Richter, M. Dominik, E. Roźniecka, M. Koba, P. Mikulic, W. J. Bock, M. Łoś, M. Śmietana, and J. Niedziółka-Jönsson, "Long-period fiber grating sensor for detection of viruses," Sens. Act. B **250**, 32–38 (2017).

305. M. Sypabekova, S. Korganbayev, Á González-Vila, C. Caucheteur, M. Shaimerdenova, T. Ayupova, A. Bekmurzayeva, L. Vangelista, and D. Tosi, "Functionalized etched tilted fiber Bragg grating aptasensor for label-free protein detection," Biosens. Bioelectron. **146**, 111765 (2019).

306. A. Bekmurzayeva, K. Dukenbayev, M. Shaimerdenova, I. Bekniyazov, T. Ayupova, M. Sypabekova, C. Molardi, and D. Tosi, "Etched fiber Bragg grating biosensor functionalized with aptamers for detection of thrombin," Sensors **18** , 4298 (2018).

307. A. Celebanska, Y. Chiniforooshan, M. Janik, P. Mikulic, B. Sellamuthu, R. Walsh, J. Perreault, and W. J. Bock, "Label-free cocaine aptasensor based on a long-period fiber grating," Opt. Lett. **44**, 2482 (2019).

308. A. Baliyan, S. Sital, U. Tiwari, R. Gupta, and E. K. Sharma, "Long period fiber grating based sensor for the detection of triacylglycerides," Biosens. Bioelectron. **79**, 693–700 (2016).

309. F. Esposito, L. Sansone, C. Taddei, S. Campopiano, M. Giordano, and A. Iadicicco, "Ultrasensitive biosensor based on long period grating coated with polycarbonate-graphene oxide multilayer," Sens. Act. B **274**, 517–526 (2018).

310. J. Yang, L. Zhou, J. Huang, C. Tao, X. Li, and W. Chen, "Sensitivity enhancing of transition mode long-period fiber grating as methane sensor using high refractive index polycarbonate/cryptophane A overlay deposition," Sens. Act B **207**, 477–480 (2015).

311. S. Barrias, J. R. Fernandes, J. E. Eiras-Dias, J. Brazão, and P. Martins-Lopes, "Label free DNA-based optical biosensor as a potential system for wine authenticity," Food Chem. **270**, 299–304 (2019).

312. B. Luo, Z. Yan, Z. Sun, Y. Liu, M. Zhao, and L. Zhang, "Biosensor based on excessively tilted fiber grating in thin-cladding optical fiber for sensitive and selective detection of low glucose concentration," Opt. Express **23**, 32429 (2015).

313. Y. Zhao, R.-J. Tong, F. Xia, and Y. Peng, "Current status of optical fiber biosensor based on surface plasmon resonance," Biosens. Bioelectron. **142**, 111505 (2019).

314. B.D. Gupta, A.M. Shrivastav, and S.P. Usha, *Optical Sensors for Biomedical Diagnostics and Environmental Monitoring*, 1st ed. (CRC Press , , 2017).

315. B. Peeters, S. Safdar, D. Daems, P. Goos, D. Spasic, and J. Lammertyn, "Solid-phase PCR-amplified DNAzyme activity for real-time FO-SPR detection of the MCR-2 gene," Anal. Chem. **92** , 10783–10791 (2020).

316. N. A. M. Zainuddin, M. M. Ariannejad, P. T. Arasu, S. W. Harun, and R. Zakaria, "Investigation of cladding thicknesses on silver SPR based side-polished optical fiber refractive-index sensor," Results Phys. **13**, 102255 (2019).

317. K. Shah, N. K. Sharma, and V. Sajal, "SPR based fiber optic sensor with bi layers of indium tin oxide and platinum: a theoretical evaluation," Optik **135**, 50–56 (2017).

318. J. Homola, S. S. Yee, and G. Gauglitz, "Surface plasmon resonance sensors: review," Sens. Act. B **54**, 3–15 (1999).

319. Y. V. Stebunov, D. I. Yakubovsky, D. Y. Fedyanin, A. V. Arsenin, and V. S. Volkov, "Superior sensitivity of copper-based plasmonic biosensors," Langmuir **34**, 4681–4687 (2018).

320. K. J. Huang, Y. J. Liu, H. B. Wang, T. Gan, Y. M. Liu, and L. L. Wang, "Signal amplification for electrochemical DNA biosensor based on two-dimensional graphene analogue tungsten sulfide-graphene composites and gold nanoparticles," Sens. Act. B **191**, 828–836 (2014).

321. M. Loyez, C. Ribaut, C. Caucheteur, and R. Wattiez, "Functionalized gold electroless-plated optical fiber gratings for reliable surface biosensing," Sens. Act B **280**, 54–61 (2019).

322. J. M. M. M. de Almeida, H. Vasconcelos, P. A. S. Jorge, and L. Coelho, "Plasmonic optical fiber sensor based on double step growth of gold nano-islands," Sensors **18** , 1–13 (2018).

323. I. Antohe, K. Schouteden, P. Goos, F. Delport, D. Spasic, and J. Lammertyn, "Thermal annealing of gold coated fiber optic surfaces for improved plasmonic biosensing," Sens. Actu. B **229**, 678–685 (2016).

324. D. Daems, B. Peeters, F. Delport, T. Remans, J. Lammertyn, and D. Spasic, "Identification and quantification of celery allergens using fiber optic surface plasmon resonance PCR," Sensors **17** , 1754 (2017).

325. F. Wang, Y. Zhang, M. Lu, Y. Du, M. Chen, S. Meng, W. Ji, C. Sun, and W. Peng, "Near-infrared band gold nanoparticles-Au film "hot spot" model based label-free ultratrace lead (II) ions detection via fiber SPR DNAzyme biosensor," Sens. Act. B **337**, 129816 (2021).

326. S. M. Tripathi, K. Dandapat, W. J. Bock, P. Mikulic, J. Perreault, and B. Sellamuthu, "Gold coated dual-resonance long-period fiber gratings (DR-LPFG) based aptasensor for cyanobacterial toxin detection," Sens. Bio-Sensing Res. **25**, 100289 (2019).

327. F. Chiavaioli, P. Biswas, C. Trono, S. Jana, S. Bandyopadhyay, N. Basumallick, A. Giannetti, S. Tombelli, S. Bera, A. Mallick, and F. Baldini, "Sol-gel-based titania-silica thin film overlay for long period fiber grating-based biosensors," Anal. Chem. **87**, 12024–12031 (2015).

328. L. L. Liu, L. Marques, R. Correia, S. P. Morgan, S. W. Lee, P. Tighe, L. Fairclough, and S. Korposh, "Highly sensitive label-free antibody detection using a long period fibre grating sensor," Sens. Act. B **271**, 24–32 (2018).

329. R. Wang, Z. Ren, D. Kong, B. Hu, and Z. He, "Highly sensitive label-free biosensor based on graphene-oxide functionalized micro-tapered long period fiber grating," Opt. Mater. (Amst) **109**, 110253 (2020).

330. G. Quero, M. Consales, R. Severino, P. Vaiano, A. Boniello, A. Sandomenico, M. Ruvo, A. Borriello, L. Diodato, S. Zuppolini, M. Giordano, I. C. Nettore, C. Mazzarella, A. Colao, P. E. Macchia, F. Santorelli, A. Cutolo, and A. Cusano, "Long period fiber grating nano-optrode for cancer biomarker detection," Biosens. Bioelectron. **80**, 590–600 (2016).

331. W. Hu, Y. Huang, C. Chen, Y. Liu, T. Guo, and B. O. Guan, "Highly sensitive detection of dopamine using a graphene functionalized plasmonic fiber-optic sensor with aptamer conformational amplification," Sens. Act. B **264**, 440–447 (2018).

332. B. Jiang, K. Zhou, C. Wang, Q. Sun, G. Yin, Z. Tai, K. Wilson, J. Zhao, and L. Zhang, "Label-free glucose biosensor based on enzymatic graphene oxide-functionalized tilted fiber grating," Sens. Act. B. **254**, 1033–1039 (2018).

333. B. Luo, Y. Xu, S. Wu, M. Zhao, P. Jiang, S. Shi, Z. Zhang, Y. Wang, L. Wang, and Y. Liu, "A novel immunosensor based on excessively tilted fiber grating coated

with gold nanospheres improves the detection limit of Newcastle disease virus," Biosens. Bioelectron. **100**, 169–175 (2018).

334. M. Lobry, D. Lahem, M. Loyez, M. Debliquy, K. Chah, M. David, and C. Caucheteur, "Non-enzymatic D-glucose plasmonic optical fiber grating biosensor," Biosens. Bioelectron. **142**, 111506 (2019).

335. Y. Zhang, F. Wang, S. Qian, Z. Liu, Q. Wang, Y. Gu, Z. Wu, Z. Jing, C. Sun, and W. Peng, "A novel fiber optic surface plasmon resonance biosensors with special boronic acid derivative to detect glycoprotein," Sensors **17**, 2259 (2017).

336. C. Ribaut, M. Loyez, J. Larrieu, S. Chevineau, P. Lambert, M. Remmelink, R. Wattiez, and C. Caucheteur, "Cancer biomarker sensing using packaged plasmonic optical fiber gratings: towards in vivo diagnosis," Biosens. Bioelectron. **92**, 449–456 (2017).

337. C. Ribaut, V. Voisin, V. Malachovská, V. Dubois, P. Mégret, R. Wattiez, and C. Caucheteur, "Small biomolecule immunosensing with plasmonic optical fiber grating sensor," Biosens. Bioelectron. **77**, 315–322 (2016).

338. V. Voisin, J. Pilate, P. Damman, P. Mégret, and C. Caucheteur, "Highly sensitive detection of molecular interactions with plasmonic optical fiber grating sensors," Biosens. Bioelectron. **51**, 249–254 (2014).

339. J. Lao, L. Han, Z. Wu, X. Zhang, Y. Huang, Y. Tang, and T. Guo, "Gold nanoparticle-functionalized surface plasmon resonance optical fiber biosensor: *in situ* detection of thrombin with 1 nM detection limit," J. Lightwave Technol. **37**, 2748–2755 (2019).

340. M. Lobry, M. Loyez, E. M. Hassan, K. Chah, M. C. DeRosa, E. Goormaghtigh, R. Wattiez, and C. Caucheteur, "Multimodal plasmonic optical fiber grating aptasensor," Opt. Express **28**, 7539 (2020).

341. M. Loyez, E. M. Hassan, M. Lobry, F. Liu, C. Caucheteur, R. Wattiez, M. C. DeRosa, W. G. Willmore, and J. Albert, "Rapid detection of circulating breast cancer cells using a multiresonant optical fiber aptasensor with plasmonic amplification," ACS Sens. **5**, 454–463 (2020).

342. Y. Shevchenko, T. J. Francis, D. A. D. Blair, R. Walsh, M. C. DeRosa, and J. Albert, "*In situ* biosensing with a surface plasmon resonance fiber grating aptasensor," Anal. Chem. **83**, 7027–7034 (2011).

343. L. Liu, X. Zhang, Q. Zhu, K. Li, Y. Lu, X. Zhou, and T. Guo, "Ultrasensitive detection of endocrine disruptors via superfine plasmonic spectral combs," Light Sci. Appl. **10**, 181 (2021).

344. S. E. Hosseini and M. A. Wahid, "Hydrogen production from renewable and sustainable energy resources: promising green energy carrier for clean development," Renew. Sustain. Energy Rev. **57**, 850–866 (2016).

345. P. Dimitriou and T. Tsujimura, "A review of hydrogen as a compression ignition engine fuel," Int. J. Hydrogen Energy **42** , 24470–24486 (2017).

346. A. M. Abdalla, S. Hossain, O. B. Nisfindy, A. T. Azad, M. Dawood, and A. K. Azad, "Hydrogen production, storage, transportation and key challenges with applications: a review," Energy Convers. Manage. **165**, 602–627 (2018).

347. J. Nakayama, N. Y. Kasai, T. Shibutani, and A. Miyake, "Security risk analysis of a hydrogen fueling station with an on-site hydrogen production system involving methylcyclohexane," Int. J. Hydrogen Energy **44** , 9110–9119 (2018).

348. T. Hübert, L. Boon-Brett, G. Black, and U. Banach, "Hydrogen sensors - a review," Sens. Act. B **157** , 329–352 (2011).

349. W. J. Buttner, M. B. Post, R. Burgess, and C. Rivkin, "An overview of hydrogen safety sensors and requirements," Int. J. Hydrogen Energy **36** , 2462–2470 (2011).

350. Y. N. Zhang, H. Peng, X. Qian, Y. Zhang, G. An, and Y. Zhao, "Recent advancements in optical fiber hydrogen sensors," Sens. Actuators, B **244**, 393–416 (2017).

351. H. E. Joe, H. Yun, S.-H. Jo, M. B. G. Jun, and B. K. Min, "A review on optical fiber sensors for environmental monitoring," Int. J. Precis. Eng. Manuf. Technol. **5** , 173–191 (2018).

352. J. X. Dai, L. Zhu, G. P. Wang, F. Xiang, Y. H. Qin, M. Wang, and M. H. Yang, "Optical fiber grating hydrogen sensors: a review," Sensors **17** , 577 (2017).

353. Z. P. Yu, L. Jin, L. H. Chen, J. Li, Y. Ran, and B. O. Guan, "Microfiber Bragg grating hydrogen sensors," IEEE Photonics Technol. Lett. **27** , 2575–2578 (2015).

354. S. Silva, L. Coelho, J. M. Almeida, O. Frazao, J. L. Santos, F. X. Malcata, M. Becker, M. Rothhardt, and H. Bartelt, "H_2 sensing based on a Pd-coated tapered-FBG fabricated by DUV femtosecond laser technique," IEEE Photon. Technol. Lett. **25** , 401–403 (2013).

355. L. Coelho, J. M. M. M. de Almeida, J. L. Santos, and D. Viegas, "Fiber optic hydrogen sensor based on an etched Bragg grating coated with palladium," Appl. Opt. **54** , 10342–10348 (2015).

356. Y. H. Yang, F. L. Yang, H. Wang, W. Yang, and W. Jin, "Temperature-insensitive hydrogen sensor with polarization-maintaining photonic crystal fiber-based Sagnac interferometer," J. Light. Technol **33** , 2566–2571 (2015).

357. C. Perrotton, R. J. Westerwaal, N. Javahiraly, M. Slaman, H. Schreuders, B. Dam, and P. Meyrueis, "A reliable, sensitive and fast optical fiber hydrogen sensor based on surface plasmon resonance," Opt. Express **21** , 382–390 (2013).

358. A. Hosoki, M. Nishiyama, H. Igawa, A. Seki, and K. Watanabe, "A hydrogen curing effect on surface plasmon resonance fiber optic hydrogen sensors using an annealed Au/Ta2O5/Pd multi-layers film," Opt. Express **22** , 18556–18563 (2014).

359. R. Tabassum and B. D. Gupta, "Fiber optic hydrogen gas sensor utilizing surface plasmon resonance and native defects of zinc oxide by palladium," J. Opt. **18** , 015004 (2016).

360. S. S. Cai, Á González-Vila, X. J. Zhang, T. Guo, and C. Caucheteur, "Palladium-coated plasmonic optical fiber gratings for hydrogen detection," Opt. Lett. **44** , 4483–4486 (2019).

361. S. S. Cai, F. Liu, R. L. Wang, Y. G. Xiao, K. W. Li, C. Caucheteur, and T. Guo, "Narrow bandwidth fiber-optic spectral combs for renewable hydrogen detection," Sci. China Inf. Sci. **63** , 222401 (2020).

362. Y. Shevchenko, G. Camci-Unal, D. F. Cuttica, M. R. Dokmeci, J. Albert, and A. Khademhosseini, "Surface plasmon resonance fiber sensor for real-time and label-free monitoring of cellular behavior," Biosens. Bioelectron. **56**, 359–367 (2014).

363. M. Loyez, J. Larrieu, S. Chevineau, M. Remmelink, D. Leduc, B. Bondue, P. Lambert, J. Devière, R. Wattiez, and C. Caucheteur, "*In situ* cancer diagnosis through online plasmonics," Biosens. Bioelectron. **131**, 104–112 (2019).

364. R. Delgado-Macuil, K. González-León, and G. Beltrán-Pérez, "Neuropsin (Opn5) detection in the brain tissue of a murine model using long period fiber grating (LPFG)," Opt. Laser Technol. **139**, 1–9 (2021).

365. R. J. Colchester, E. Z. Zhang, C. A. Mosse, P. C. Beard, I. Papakonstantinou, and A. E. Desjardins, "Broadband miniature optical ultrasound probe for high resolution vascular tissue imaging," Biomed. Opt. Express **6**, 1502 (2015).

366. S. Ohayon, A. Caravaca-Aguirre, R. Piestun, and J. J. DiCarlo, "Minimally invasive multimode optical fiber microendoscope for deep brain fluorescence imaging," Biomed. Opt. Express **9**, 1492 (2018).

367. J. Desroches, M. Jermyn, M. Pinto, F. Picot, M.-A. Tremblay, S. Obaid, E. Marple, K. Urmey, D. Trudel, G. Soulez, M.-C. Guiot, B. C. Wilson, K. Petrecca, and F. Leblond, "A new method using Raman spectroscopy for *in vivo* targeted brain cancer tissue biopsy," Sci. Rep. **8**, 1792 (2018).

368. A. Vernet-Crua, D. Medina-Cruz, E. Mostafavi, A. Benko, J. L. Cholula-Diaz, M. Suravana, H. Vahidi, H. Barabadi, and T. J. Webster, "Nanobiosensors for theranostic applications," in *Handbook on Nanobiomaterials for Therapeutics and Diagnostic Applications* (Elsevier, 2021), Chap. 23, pp. 511–543 .

369. M. Schürmann, G. Cojoc, S. Girardo, E. Ulbricht, J. Guck, and P. Müller, "Three-dimensional correlative single-cell imaging utilizing fluorescence and refractive index tomography," J. Biophotonics **11** , 1–11 (2018).

370. T.-L. Liu, S. Upadhyayula, D. E. Milkie, V. Singh, K. Wang, I. A. Swinburne, K. R. Mosaliganti, Z. M. Collins, T. W. Hiscock, J. Shea, A. Q. Kohrman, T. N. Medwig, D. Dambournet, R. Forster, B. Cunniff, Y. Ruan, H. Yashiro, S. Scholpp, E. M. Meyerowitz, D. Hockemeyer, D. G. Drubin, B. L. Martin, D. Q. Matus, M. Koyama, S. G. Megason, T. Kirchhausen, and E. Betzig, "Observing the cell in its native state: imaging subcellular dynamics in multicellular organisms," Science **360** , 284 (2018).

371. S. A. Alqarni, W. G. Willmore, J. Albert, and C. W. Smelser, "Self-monitored and optically powered fiber-optic device for localized hyperthermia and controlled cell death *in vitro*," Appl. Opt. **60**, 2400–2411 (2021).

372. J. Koppert, H. Jean-Ruel, D. O'Neill, C. Harder, W. Willmore, A. Ianoul, and J. Albert, "Self-heating tilted fiber Bragg grating device for melt curve analysis of solid-phase DNA hybridization and thermal cycling," Anal. Bioanal. Chem. **411**, 6813–6823 (2019).

373. K. Yang, B. Liu, C. Liao, Y. Wang, Z. Cai, J. Tang, Y. Yang, and Y. Wang, "Highly localized point-by-point fiber Bragg grating for multi-parameter measurement," J. Lightwave Technol. **39** , 6686–6690 (2021).

374. K. Yao, Q. Lin, Z. Jiang, N. Zhao, B. Tian, and G. D. Peng, "Joint-peaks demodulation method based on multireflection peaks of a few-mode fiber Bragg grating for reducing sensing error," Opt. Express **29**, 4422–4430 (2021).

375. Y. Yu, X. Zhang, K. Wang, Z. Wang, H. Sun, Y. Yang, C. Deng, Y. Huang, and T. Wang, "Coexistence of transmission mechanisms for independent multiparameter sensing in a silica capillary-based cascaded structure," Opt. Express **29**, 27938–27950 (2021)..

Christophe Caucheteur received his master's degree in electrical engineering and his Ph.D. degree in applied sciences from the Faculté Polytechnique de Mons, Belgium, in 2003 and 2007, respectively. He is currently a Senior Research Associate of the F.R.S.-FNRS with the University of Mons, and he is the Head of the Advanced Photonic Sensors ERC unit. He is the coauthor of about 250 papers in international journals and conference proceedings. He is also coauthor of six international patent applications regarding the development of innovative FBG sensors. He was the recipient of the European Research Council Starting Grant for a research project focused on the development of innovative plasmonic biochemical optical fiber sensors. He is co-founder of the spin-off company B-SENS (www.b-sens.be) that specializes in the design and development of advanced sensing solutions based on FBGs. He is associated editor of the Optica journal *Optics Express*, the *Elsevier Journal of Optics & Laser Technology*, and *MDPI Sensors* and has served as TPC member of numerous international conferences including OFS and BGPP.

Joel Villatoro received his M.Sc. and Ph.D. degrees in optics from the INAOE-Instituto Nacional de Astrofísica, Óptica y Electrónica, Puebla, Mexico, in 1995 and 1999, respectively. He is currently Ikerbasque Research Professor at the University of the Basque Country UPV/EHU. Prior to his current position, he held research posts at Aston Institute of Photonic Technologies, Birmingham, U.K.; the Institute of Photonic Sciences (ICFO), Barcelona, Spain; the Centro de Investigaciones en Óptica A. C., Leon, Mexico; the University of Valencia, Spain; and the Case Western Reserve University, Cleveland, Ohio, USA. In 2020, he was awarded the distinction of Optica Fellow for his contributions to interferometric optical fiber sensors. In 2021, he was included in the prestigious list of the World's top 2% of scientists. His research interests include interferometric sensors based on standard, multicore and photonic-crystal fibers, applications of sensors in real-world environments, and development of micro- and nano-sensors for biomedical applications.
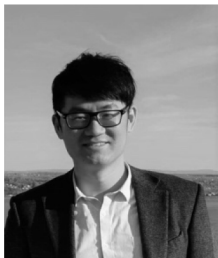
Fu Liu received his B.S. degree in application physics from Northwest University, Xi'an, China, in 2011, his M.S. degree from the Institute of Photonics Technology from Jinan University, Guangzhou, China, in 2015, and his Ph.D. degree from Carleton University, Ottawa, Ontario, Canada, in 2020. His main research focuses on ultrafast switching using tailored permittivity materials on optical fiber gratings.

Médéric Loyez studied biology at the University of Mons, Belgium, where he received his master's degree in 2016. He was the recipient of the award for the best master's thesis in biology that year. He started his doctoral thesis in October 2016, after obtaining a FRIA grant (F.R.S.-FNRS). He went to Carleton University, Ottawa, Ontario, Canada, for a research stay during his Ph.D. to learn about new biosensing strategies. In 2020, Médéric was granted as Postdoctoral Researcher (Chargé de Recherches, F.R.S.-FNRS). He is currently working on the development of optical fiber biosensors.

Tuan Guo received his Ph.D. degree in optics from Nankai University, China, in 2007. From 2007 to 2010, he was a Postdoctoral Fellow with the Department of Electronics, Carleton University, Canada and the Photonics Research Centre, The Hong Kong Polytechnic University, respectively. Since 2010, he has been working with Jinan University, first as an Associate Professor and then as a Full Professor. He founded and is currently heading the research activities of the Photonic Sensing for Energy & Biology Laboratory at the Institute of Photonics Technology. His current research interests include optical fiber sensors, plasmonics, biophotonics, and photonics for renewable energy. He co-authored about 250 papers in peer-refereed journals and international conferences and two book chapters and has been awarded 20 patents from China and USA. He received the 2018 Technical Award of the IEEE Instrumentation and Measurement Society. He is currently the IEEE-IMS technical committee chair of "Photonic Technology in Instrumentation and Measurement", a senior member of IEEE, and a senior member of Optica. He is an Associate Editor for the *IEEE/OSA Journal of Lightwave Technology*, an Associate Editor for the *Science China Information Sciences*. He has

served as Associate TPC Chair for IEEE International Instrumentation and Measurement Technology Conference from 2019 to 2021, Session Chair of IEEE International Flexible Electronics Technology Conference 2018, and TPC section Co-Chair of the CLEO Pacific Rim 2018.
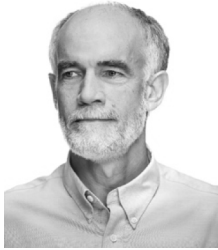
Jacques Albert has degrees in physics from the Université de Montréal and Université Laval, followed by a Ph.D. in electrical engineering from McGill University in 1988. He worked as a research scientist at the Government of Canada Communications Research Centre in Ottawa for 11 years and then at Alcatel Optronics Canada as Senior scientist in research and development of new products. In 2004, he was awarded a Tier 1 Canada Research Chair in Advanced Photonic Components at Carleton University (renewed in 2011 and 2018). Since then, he has led a research group with worldwide collaborative activities in various fields of photonics, mostly dealing with optical fiber sensors for physical and biochemical sensing applications. In addition to frequent participations on the Program committees of major conferences and Topical meetings (including CLEO, OSA Sensors, IEEE Photonics Conference, BGPP), he has chaired several international meetings in photonics, including OFS-21 (Optical Fiber Sensors), the BGPP Topical meeting of the OSA, and Photonics North. He was an Associate Editor for *Optics Express* from 2007 to 2013 and he is currently Deputy Editor of the *IEEE Journal of Lightwave Technology*. In 2013, he was named a Fellow of the OSA for "Outstanding and sustained contributions to the science and technology of fiber Bragg gratings and their applications."